

THESIS

CHARACTERIZATION OF A PHOTOLUMINESCENCE-BASED  
FIBER OPTIC SENSOR SYSTEM

Submitted by

Zhangjing Yi

Department of Electrical and Computer Engineering

In partial fulfillment of the requirements

For the Degree of Master of Science

Colorado State University

Fort Collins, Colorado

Fall 2011

Master's Committee:

Advisor: Kevin L. Lear

Ali Pezeshki

Jennifer L. Mueller

Copyright by Zhangjing Yi 2011

All Rights Reserved

## ABSTRACT

### CHARACTERIZATION OF A PHOTOLUMINESCENCE-BASED FIBER OPTIC SENSOR SYSTEM

Measuring multiple analyte concentrations is essential for a wide range of environmental applications, which are important for the pursuit of public safety and health. Target analytes are often toxic chemical compounds found in groundwater or soil. However, in-situ measurement of such analytes still faces various challenges. Some of these challenges are rapid response for near-real time monitoring, simultaneous measurements of multiple analytes in a complex target environment, and high sensitivity for low analyte concentration without sample pretreatment. This thesis presents a low-cost, robust, multichannel fiber optic photoluminescence (PL)-based sensor system using a time-division multiplexing architecture for multiplex biosensor arrays for *in-situ* measurements in environmental applications. The system was designed based upon an indirect sensing scheme with a pH or oxygen sensitive dye molecules working as the transducer that is easily adaptable with various enzymes for detecting different analytes.

A characterization of the multi-channel fiber optic PL-based sensor system was carried out in this thesis. Experiments were designed with interests in investigating this

system's performance with only the transducer thus providing reference figures of merit, such as sensitivity and limit of detection, for further experiments or applications with the addition of various biosensors. A pH sensitive dye, fluoresceinamine (FLA), used as the transducer is immobilized in a poly vinyl alcohol (PVA) matrix for the characterization. The system exhibits a sensitivity of  $8.66 \times 10^5 \text{ M}^{-1}$  as the Stern-Volmer constant,  $K_{SV}$ , in  $\text{H}^+$  concentration measurement range of  $0.002 - 891 \text{ } \mu\text{M}$  (pH of  $3.05 - 8.69$ ). A mathematical model is introduced to describe the Stern-Volmer equation's non-idealities, which are fluorophore fractional accessibility and the back reflection. Channel-to-channel uniformity is characterized with the modified Stern-Volmer model. Combining the FLA with appropriate enzymatic biosensors, the system is capable of 1,2-dichloroethane (DCA) and ethylene dibromide (EDB) detection. The calculated limit of detection (LOD) of the system can be as low as  $0.08 \text{ } \mu\text{g/L}$  for DCA and  $0.14 \text{ } \mu\text{g/L}$  for EDB.

The performances of fused fiber coupler and bifurcated fiber assembly were investigated for the application in the fiber optic PL-based sensor systems in this thesis. Complex tradeoffs among back reflection noise, coupling efficiency and split ratio were analyzed with theoretical and experimental data. A series of experiments and simulations were carried out to compare the two types of fiber assemblies in the PL-based sensor systems in terms of excess loss, split ratio, back reflection, and coupling efficiency. A noise source analysis of three existing PL-intensity-based fiber optic enzymatic biosensor systems is provided to reveal the power distribution of different noise components. The three systems are a single channel system with a spectrometer as the detection device, a lab-developed multi-channel system, and a commercial prototype multi-channel system

both using a photomultiplier tube (PMT) as the detection device. The thesis discusses the design differences of all three systems and some of the circuit design alteration attempts for performance improvements.

## TABLE OF CONTENTS

Chapter 1 Introduction .....	1
1.1 Introduction .....	1
1.2 Motivation .....	2
1.3 Overview of the Chapters .....	3
1.4 References .....	6
Chapter 2 Background .....	7
2.1 Introduction .....	7
2.2 Optical Sensing Scheme .....	8
2.3 Detection Methods ... ..	14
2.4 Fiber Optics ... ..	19
2.5 Optical Pathway Splitting Methods.. ..	20
2.6 Optical Detection Parameters .. ..	24
2.7 Workings of Optical Detectors ... ..	26
2.8 References .....	29
Chapter 3 Literature Review of Fiber Optic Chemical Sensor Systems .....	31
3.1 Introduction .....	31
3.2 Intensity-Based Fiber Optic Sensor Systems .....	32

3.3	Multi-Analyte-Capable Sensor Systems .....	38
3.4	Fiber-Optic Splitting Mechanism .....	45
3.5	The Non-Idealities in Stern-Volmer Relationship .....	52
3.6	References .....	58
 Chapter 4 Characerization of the Multi-Channel Fiber Optic Fluorescence Detection		
	System .....	60
4.1	Introduction .....	60
4.2	System Configuration .....	61
4.3	Optodes Fabrication .....	65
4.4	Measurements Protocols .....	66
4.5	Sensitivity Measurement Results .....	67
4.6	Channel-to-Channel Uniformity Measurements .....	73
4.7	Discussion .....	75
4.8	References .....	81
 Chapter 5 A Comparison Between Multimode Fused Fiber Coupler and Bifurcated Fiber		
	Assembly in Photoluminescence (PL) - Based Biosensor Systems .....	83
5.1	Introduction .....	83
5.2	Motivation .....	84
5.3	Experimental Set-up .....	86
5.4	Split Ratio and Excess Loss Results and Discussion .....	88
5.5	Back Reflection Results and Discussion .....	91

5.6	Coupling Efficiency Results and Discussion .....	94
5.7	References .....	101
Chapter 6 Existing Photoluminescence (PL) - Based Fiber Optic Systems		
	Comparison.....	103
6.1	Introduction .....	103
6.2	Configuration .....	104
6.3	Noise Analysis .....	108
6.4	References .....	116
Chapter 7 Conclusion and Future Work .....		
7.1	Conclusion .....	117
7.2	Future Work .....	119
Appendix A PH Buffer Solutions Protocols .....		
A.1	Introduction .....	121
A.2	Calculation Principles .....	122
A.3	Stock Solutions Protocols .....	122
A.4	Buffer Solutions Protocls .....	124
Appendix B Radio Frequency (RF) Interference Measurements .....		
B.1	Discovery of the Problem .....	130
B.2	RF Interference Measurements .....	131
Appendix C Oxygen Sensitive Optodes Measurements .....		
C.1	Motivation .....	136

C.2	Principles and Experimental Set-up .....	137
C.3	Preliminary Experimental Results .....	140
C.4	Notes on Future Works .....	143
C.5	References .....	144
Appendix D Back Reflection With Index Matching Measurements .....		145
D.1	Motivation .....	145
D.2	Experimental Set-up .....	146
D.3	Preliminary Experimental Results .....	147
Appendix E System II Documents .....		152
E.1	Introduction .....	152
E.2	Electronic Schematics .....	153
E.3	Bill Of Materials .....	154
E.4	User's Manual .....	156
Appendix F System III Documents .....		161
F.1	Introduction .....	161
F.2	Electronic System .....	162
F.3	Bill Of Materials .....	165
F.4	User's Manual .....	165
Appendix G ST Connector Related Problems .....		168
G.1	Introduction .....	168
G.2	Fiber Inspections .....	169

G.3	An Analysis On the Variation .....	170
G.4	Cleaning Procedures .....	171

# Chapter 1

## INTRODUCTION

### 1.1 Introduction

The use of fluorescence or phosphorescence, also known as photoluminescence (PL), for sensing has grown tremendously during the past few decades. The applications have been expanded to many extensive fields, such as biotechnology, medical diagnostics [1], cell and molecular biology analysis, cellular and molecular imaging, and chemical compounds detection, just to name a few. It is no accident that the PL is widely used in numerous disciplines because of its fast response and highly sensitive in detection. This thesis emphasizes the use of the PL as the transducer [2] for chemical or biological sensors as the detection tool for chemical compound concentrations [3] [4]. As an interaction of the sensor and the target analyte in the environment occurs, the interaction directly or indirectly alters the signal generated by the transducer. In this manner, the signal generated by the transducer carries the information reflecting the analyte, and thus realizes the detection of the analyte. Chemical or biological sensors are often superior choices for practical applications given their advantages of miniaturized size, real-time

response, and specificity in detection. This thesis focuses on the use of biological sensors or biosensors as the sensing device for its ease of alteration to detect a wide range of analytes. Among various biosensors, enzymatic biosensors are widely utilized for their advantages of requiring no alteration and the specificity achieved through genetic engineering processes [5].

## **1.2 Motivation**

Measuring multiple analyte concentrations is essential for a wide range of environmental applications, which are important for the pursuit of public safety and health. Target analytes are often toxic chemical compounds found in groundwater or soil. Conventional methods often require preservation and pretreatments of the samples prior to the measurements resulting in slow and expensive detection processes. However, *in-situ* measurement of such analytes still faces various challenges. Some of these challenges are rapid response for near-real time monitoring, simultaneous measurements of multiple analytes in a complex target environment, and high sensitivity for low analyte concentration without sample pretreatment. A robust, rapid response, multi-analyte, *in-situ* measuring sensor system is desired.

A multi-channel fiber optic fluorescence system for *in-situ* measurements in environmental applications was designed and constructed using a time-division multiplexing [6] architecture. The system was designed based upon an indirect sensing scheme with a pH or oxygen sensitive dye molecules working as the transducer that is easily adapted with various enzymes for detecting different analytes. The principles of the sensing scheme that underlies the system design is presented in Chapter 2. The ease

of adapting the transducer and the specificity of the sensors makes the system architecture suitable for detecting different analytes without major modification and for simultaneous detection of multiple analytes sharing a common architecture.

### **1.3 Overview of the chapters**

Chapter 2 of this thesis presents some critical background subjects regarding the enzymatic biosensor indirect sensing scheme. Based on the transducer-sensor mechanism, two common detection methods are presented. Also, fiber optic related subjects are covered to provide a general insight of the knowledge of fiber optic transmission and coupling devices. The workings of different detection devices are provided for an understanding of the artifacts and noise sources associated with system performance.

The photoluminescence based sensor systems in current publications are reviewed in Chapter 3 of this thesis. Because of the wide usage of the sensor systems, numerous relevant research papers have been published although only closely related studies are reviewed in the chapter. Two of the photoluminescence intensity based fiber optic sensor systems are studied and compared in terms of the design and the detection abilities. These systems have common properties such as using the same fundamental of hardware and using fiber-optics as the optical transmission component for its apparent advantages in field applications. Then two multi-analyte-capable sensor systems are presented with comparison to the system in this thesis. Because the inherent properties of PL intensity based sensor systems, the optical pathway splitting mechanism is required. Many methods of doing so have been explored, such as free-space coupling, fused fiber coupler

and bifurcated cables. The chapter provides a comparison of different optical pathways splitting methods. Furthermore, some non-idealities of the classic principles have been observed and reported in recent studies, and the chapter provides a review of published explanations and associated mathematical models of those non-ideal elements.

A characterization of the multi-channel fiber optic fluorescence detection system was carried out and described in Chapter 4 of this thesis. Experiments were designed with for investigating this system's performance with only the transducer, thus providing reference figures of merit, such as sensitivity and limit of detection, for further experiments or applications with the addition of various biosensors. The transducer used in this chapter is a pH sensitive dye, fluoresceinamine (FLA), immobilized in a poly vinyl alcohol (PVA). Combining the FLA with appropriate enzymatic biosensors, the system is capable of 1,2-dichloroethane (DCA) and ethylene dibromide (EDB) detection. System configuration, experimental set up, transducer fabrication procedures, and experimental procedures are provided. A series of experiments for the measure of the system sensitivity were presented with results and discussions. Also, the uniformity between channels for the multichannel system is characterized in the chapter.

The performances of fused fiber coupler and bifurcated fiber assembly were investigated for the application in the photoluminescence (PL)-based biosensor systems in Chapter 5. Complex tradeoffs among back reflection interference, coupling efficiency and split ratio were analyzed with theoretical and experimental data. A series of experiments and simulations were carried out to compare the two types of fiber assemblies in the PL-based biosensor systems in terms of excess loss, split ratio, back reflection, and coupling efficiency.

In Chapter 6, a frequency analysis of three existing PL-intensity-based fiber optic enzymatic biosensor systems is provided to reveal the power distribution of different noise components. The three systems are a single channel system with a spectrometer as the detection device, a lab-developed multi-channel system, and a commercial prototype multi-channel system. The chapter discusses the design differences of all three systems and some of the design alteration attempts for performance improvements.

Conclusions and future work are included in Chapter 7. A number of appendices document related supplementary subjects for the purpose of future references. Appendix A provides the protocols for pH buffer solution preparation. This is used for the characterization using the pH sensitive transducers. Appendix B presents an RF interference experiment with the multi-channel PL based fiber optic system. Effective solutions are also provided in this appendix. In Appendix C, a new experimental approach of oxygen sensitive transducer characterization is suggested. The new method leaves out the cumbersome set-up with the nitrogen gas, and realized a robust compact design that is suitable for *in-situ* calibration procedure with the oxygen sensitive transducers. This appendix also provides some experimental results as an example. Appendix D is a further exploration of Chapter 5. The appendix provides some preliminary results on the index matching method suggested in Chapter 5 to eliminate the back reflection interference existed in the fused fiber coupler devices. Appendix E and Appendix F are the related documentation of the two multi-channel PL-based fiber optic systems, and they include system block diagrams, electrical circuitry schematics, Bill of Materials, and user's manuals. Appendix G presents an ST-connector-induced variation problem, and provides a theoretical analysis and solutions of prevention.

## 1.4 References

- [1] Rongjin Yan et al., "Waveguide biosensor with integrated detector array for tuberculosis testing," *Applied Physics Letters*, vol. 98, no. 1, p. 013702, Jan 2011.
- [2] Sean B. Pieper, "Optical Characterization of Phosphorescent Dyes for Biosensor Transducer Applications," Colorado State University, Fort Collins, Thesis 2008.
- [3] K. F. Reardon, D. W. Campbell, and C. Müller, "Optical fiber enzymatic biosensor for reagentless measurement of ethylene dibromide," *Eng. Life Sci.*, vol. 9, no. 4, pp. 291–297, Aug 2009.
- [4] D. W. Campbell, C. Müller, and K. F. Reardon, "Development of a fiber optic enzymatic biosensor for 1,2-dichloroethane," *Biotechnol Lett*, vol. 28, no. 12, pp. 883–887, May 2006.
- [5] Zhangjing Yi et al., "A Multi-Channel Fiber Optic Photoluminescence System for Multiplex Biosensor Arrays," in *Proceedings of SPIE-The International Society for Optical Engineering Optical Fibers and Sensors for Medical Diagnostics and Treatment Applications X*, San Francisco, CA, 2010.
- [6] K. F. Reardon, Z. Zhong, and K. L. Lear, "Environmental applications of photoluminescence-based biosensors," in *Advances in Biochemical Engineering/Biotechnology*, T. Scheper, Ed.: Springer, 2010, ch. 116, pp. 99-123.

# Chapter 2

## **BACKGROUND**

### **2.1 Introduction**

In this chapter, some critical background subjects related to this thesis are included. Section 2.2 introduces the enzymatic biosensor indirect sensing scheme, which relies on two parts, indicators and corresponding biological components. Based on this mechanism, two very common and well developed methods of detection using fiber optics are presented in Section 2.3, and they are intensity detection and phase-angle detection. Next, basic information on fiber optics are included in Section 2.4 to prepare the audience to better understand the coupling mechanisms of the different types of optical pathway splitting apparatus in Section 2.5. Important parameters in evaluating an optical detector are included in Section 2.6 to provide readers with understanding and insight of artifacts associated with system performance. The workings of few different optical detectors, such as spectrometers, photodiodes, and photomultiplier tubes (PMT), are explained in Section 2.7. Section 2.8 covers some system performance factors that commonly exist in electro-optical systems, and potential solutions for them.

## 2.2 Optical Sensing Scheme

There are two optical sensing schemes in chemical sensors and biosensors, direct and indirect sensing. In the first, the intrinsic optical properties of the analyte are measured, while in the second the “color” of an immobilized indicator dye, label, or optically detectable bioprobe is monitored [1]. The direct sensing scheme is beyond the scope of discussion in this thesis, and the indirect sensing scheme is briefly introduced here. An indirect sensing scheme often relies on luminophores as the indicator, and a biocomponent as the sensor.

Luminophore is briefly defined as a material that emits photoluminescence (PL). PL is the result of a process of the photonic excitation of an atomic or molecular system that releases a portion of the excitation energy as a photon of another color [2]. To explain from the energy states stand of point, PL process can be schematically illustrated by a Jablonski diagram [3], shown in Figure 2.1. The singlet energy states of ground, first and second vibrational states are indicated by  $S_0$ ,  $S_1$ , and  $S_2$  respectively. The transition depicted as vertical lines from the ground state to the higher energy states is to illustrate the process of light absorption. The large gap between the ground states and the excited states results in the photonic excitation instead of thermally induced excitation at room temperature. After the light absorption, the fluorophore is excited at a higher vibrational state  $S_1$  or  $S_2$ , and then rapidly ( $< 10^{-12}$  s) relax to the lowest allowed level of  $S_1$  through a process called internal conversion. After that the process of excited electrons fall back to the ground states with the emission of photon at a longer wavelength with respect to the absorption wavelength is called fluorescence. The resulting spectral shift is known as the Stokes shift, as shown in Figure 2.2 with Hoechst 33342 as an example of luminophore

[4]. There are two types of luminophores, which are fluorophores and phosphors, and the corresponding PL processes are fluorescence and phosphorescence. The phosphorescence has a very similar process except the electrons at  $S_1$  can undergo a intersystem crossing to a forbidden triplet state  $T_1$ . The transition from  $T_1$  to the ground states is forbidden, and as a result, the relaxation from triplet states takes longer than the fluorescence process and has a longer wavelength emission.

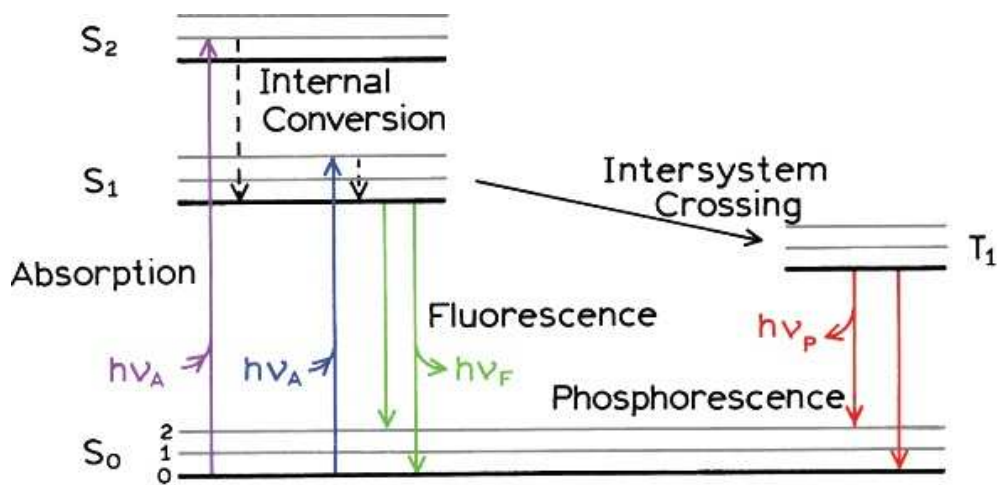


Figure 2.1. A Jablonski diagram to illustrate the fluorescence and phosphorescence processes. Reproduced from Reference [3].

Two parameters of the PL process are typically very important to characterized the emission. First is the quantum yield, which defined as the ratio of the total number of emitted photons to the absorbed number. During the relaxation from the excited states  $S_1$  to the ground state, two types of processes occur, photon emission with decay rate of  $\Gamma$  and non-radiative decay with rate of  $k_{nr}$ , and the quantum yield  $Q$  is defined as

$$Q = \frac{\Gamma}{\Gamma + k_{nr}} . \quad 2-1$$

Second parameter is the fluorephore lifetime, which the average time an excited photon takes to decay back to the ground state. The lifetime is defined as

$$\tau = \frac{1}{\Gamma + k_{nr}} . \quad 2-2$$

A formal distinction between the two is that fluorescence is characterized by a fast radiative recombination transition with decay lifetimes less than 10 ns and generally a small Stokes shift, while phosphorescence has its decay lifetimes longer than 10 ns and a larger Stoke's shift [5].

When the luminophores is encountered by the another kind of molecules, known as the quencher, in the adjacent environment, the quantum yireld is inhibited by the quencher, and that process is called quenching. There are two types of quenching, static and dynamic or collisional quenching. A quantitative definition of the collisional quenching is known as the Stern-Volmer equation, which is described in details in the next section of this chapter. Static quenching is the process involving the quencher and the excited luminophore forming a complex and relaxing to the ground states without any photon emission.

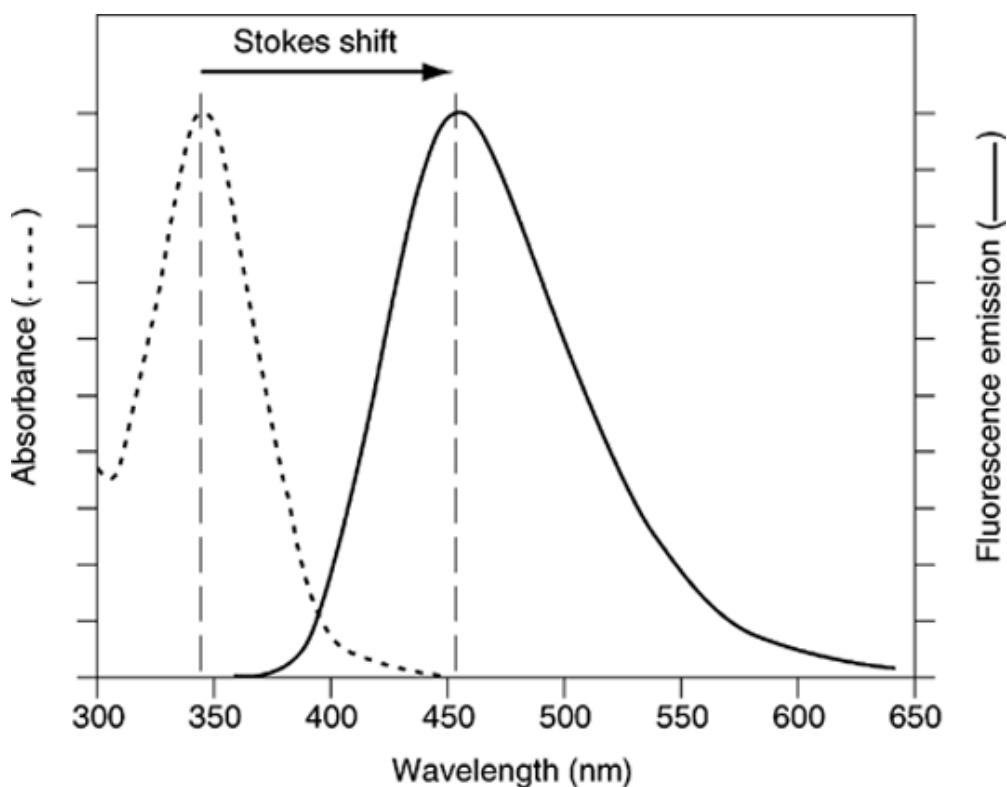


Figure 2.2. Absorption and emission spectra of a fluorophore named Hoechst 33342 (Molecular Probes), a dye that is used to stain DNA. The dye is excited with monochromatic light, typically near the  $\lambda_{\text{max}}$  of the absorption spectrum (in this case, ~350 nm), and the emission at 450 nm is measured with a spectrofluorometer. Spectra have been normalized. Reproduced from Reference [4].

Utilizing the fluorophore mechanism and the enzyme catalysis mechanism can form the enzymatic biosensor sensing scheme. An illustrative explanation of the luminophores-quencher pair working mechanism is shown in Figure 2.3. The quencher's presence in the luminophores' near-by environment alters the PL efficiency of the luminophores, and as a result, higher quencher concentration decreases the associated PL emission under the constant excitation power.

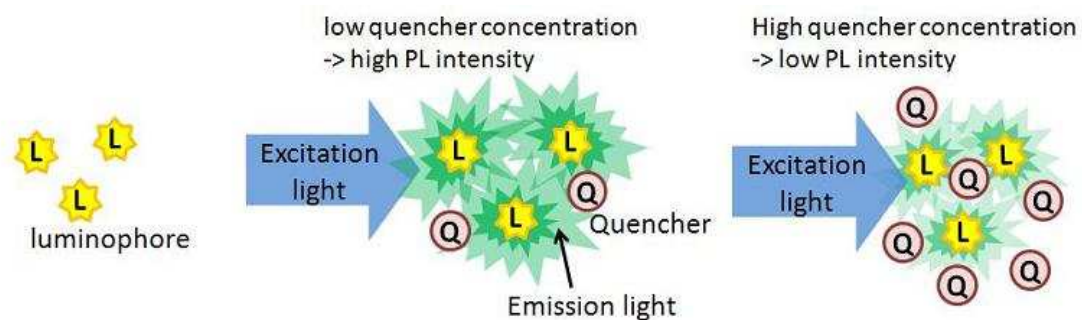


Figure 2.3. A simplified illustration of a luminophore-quencher pair working mechanism. The presence of the quencher in the adjacent environment of the luminophores alters the associated PL emission intensities under the same excitation intensity.

In the biosensor sensing process, a biological component is often used to recognize the analyte's information. Typical components include enzymes, antibodies, oligonucleotides, and whole cells [1], and among those, enzymes are widely used. Enzymes are proteins that catalyze chemical reactions. Like all catalysts, enzymes work by lowering the activation energy for a reaction, thus dramatically increasing the rate of the reaction to equilibrium. Enzymes have the advantages as all catalysts that no consumption by the reactions they catalyze, and no alteration to the reaction equilibrium; yet enzymes are more specific than most other catalysts. With those properties, enzymes are an ideal candidate for in-situ measurements of specific analyte. Genetically engineered enzymes can be designed to accelerate a reaction with the target analyte being one of the substrates of the reaction, and quencher as one of the products. With this mechanism, shown in Figure 2.4, a higher concentration of the analyte produces a higher concentration of quencher in the adjacent areas of the enzyme.

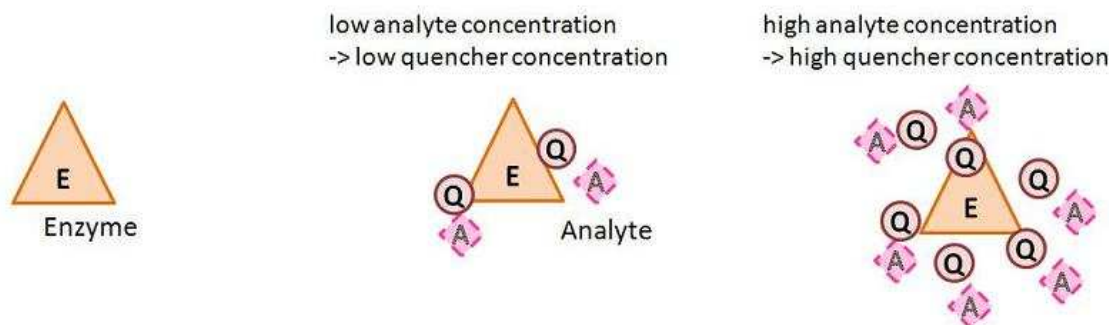


Figure 2.4. A simplified diagram of an enzymatic reaction with the target analyte being one of the substrates and quencher being one of the products. A higher analyte concentration in the enzyme adjacent areas results in a higher concentration of produced

An indirect analyte sensing scheme forms as the biocomponent, enzymes, works in conjunction with the luminophores. As shown in Figure 2.5, enzymatic reaction of the analytes produces quencher to inhibit PL efficiency of the luminophores, and in this way the biosensor transduces the target analyte information into PL intensities. Therefore, by detecting the PL intensities from the luminophores we can tell how much analyte concentration there is in the area of interest.

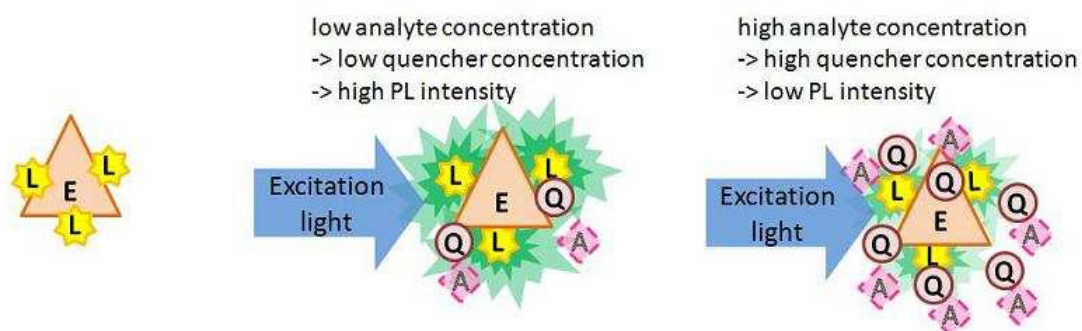


Figure 2.5. A simplified illustration of the indirect sensing scheme using the enzymatic biosensors working in conjunction with the luminophore-quencher pair.

## 2.3 Detection Methods

Two common detection methods used in the PL-based sensor systems are intensity and phase-angle measurements. First, the intensity measurement is based on the Stern-Volmer relationship, named after Otto Stern and Max Volmer. The kinetics of the PL quenching process follows the Stern-Volmer equation [6],

$$\frac{I_0}{I} = 1 + K_{SV}[Q] = 1 + k_q\tau_0[Q], \quad 2-3$$

where  $I$  and  $I_0$  are the PL emission intensities in the presence and in the absence of the quencher respectively,  $[Q]$  is the quencher concentration, and  $K_{SV}$  is the Stern-Volmer quenching constant, which depends on the biomolecular quenching constant,  $k_q$ , and the unquenched decay lifetime,  $\tau_0$ . As an example in Figure 2.6, the PL emission spectra and the Stern-Volmer ratio  $I/I_0$  at  $\lambda$  of 550 nm collected from quantum dots (QDs) for various analyte concentrations [7].

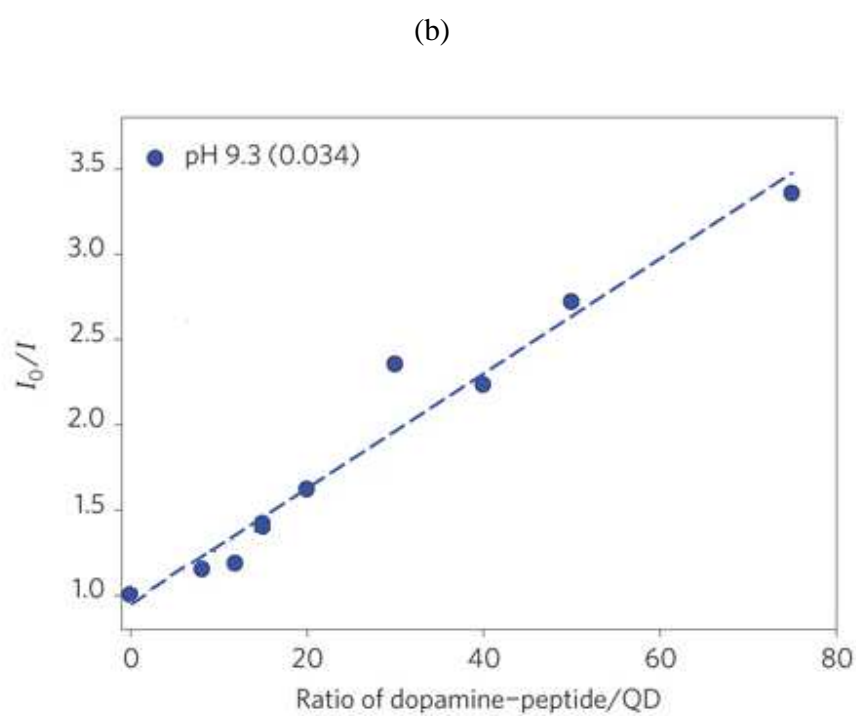
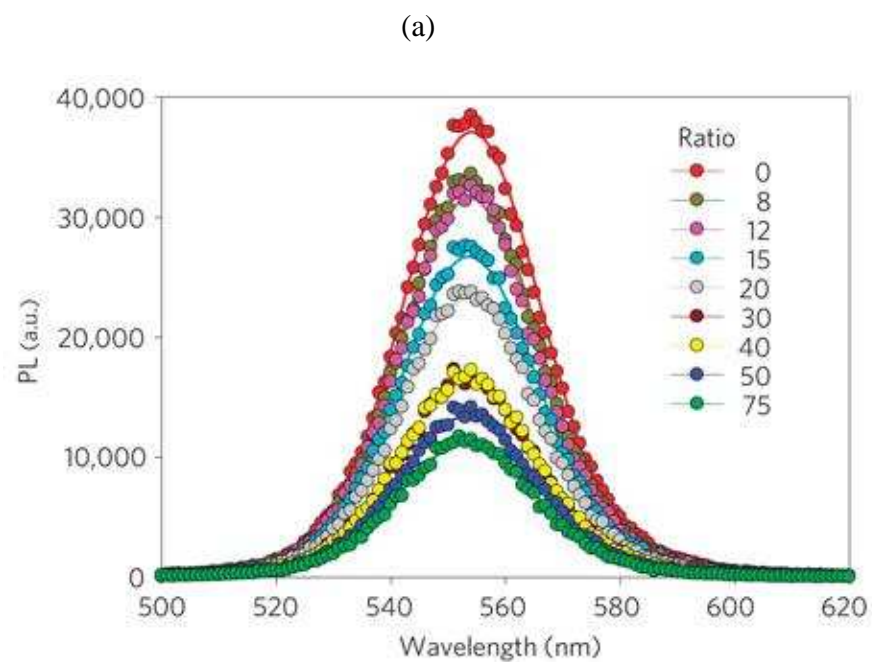


Figure 2.6 (a) Representative PL spectra collected from 550-nm-emitting QDs self-assembled with an increasing ratio of dopamine-peptide (analyte) added to PBS buffer at pH 9.3. (b) Plots of increasing ratio of dopamine-peptide/QD in a Stern-Volmer format ( $I_0/I$  versus ratio of dopamine/QD) at pH 9.3. Reproduced from Reference [7].

Another well-known technique used in PL-based biosensor system is the phase-angle method. This method uses the PL lifetime of the indicators as information and uses the phase modulation technique to evaluate the lifetime [8]. In place of PL intensity as the measureable parameter, the PL decay lifetime  $\tau$  can be used, provided that the PL decay is a single exponential. The quenched steady state intensity  $I$  can be seen as the averaged intensity during the decay for one time constant

$$I = \int_0^{\infty} I_{max} e^{-t/\tau} dt = I_{max}\tau, \quad 2-4$$

where  $\tau$  is the lifetimes with the presence of the quencher. And the unquenched intensity  $I_0$  becomes

$$I_0 = \int_0^{\infty} I_{max} e^{-t/\tau_0} dt = I_{max}\tau_0, \quad 2-5$$

The take Eqn. 2-4 and Eqn. 2-5 back into Eqn. 2-3, which now becomes

$$\frac{I_0}{I} = \frac{I_{max}\tau_0}{I_{max}\tau} = \frac{\tau_0}{\tau}, \quad 2-6$$

Therefore, the Stern-Volmer equation, Eqn. 2-3, is then written [9] as,

$$\frac{\tau_0}{\tau} = 1 + K_{SV}[Q] = 1 + k_q\tau_0[Q], \quad 2-7$$

where  $\tau$  and  $\tau_0$  are the lifetimes with and without the presence of the quencher, respectively. When a luminophore is excited with sinusoidally modulated light, its lifetime causes a time delay of the emitted light signal. In technical terms this delay is the phase angle between the exciting and emitted signal. This phase angle is shifted as a

function of the quencher concentration, as the example shown in Figure 2.7 [10].

Assuming the excitation light has modulated function

$$y_{ex}(t) = A \cdot \sin(\omega_0 t), \quad 2-8$$

where  $A$  is the amplitude, and  $\omega_0$  is the angular frequency of the modulation. PL intensity has a function

$$y_{PL}(t) = B \cdot \sin(\omega_0 t + \Phi), \quad 2-9$$

where  $B$  is the magnitude,  $\Phi$  is the phase shift of PL intensity function due to the decay lifetime, thus the function can also be seen as

$$y_{PL}(t) = B \cdot \sin[\omega_0(t + \tau)], \quad 2-10$$

where  $\tau$  is the PL decay lifetime. Combine Eqn. 2-9 and Eqn. 2-10, the relationship between the lifetime  $\tau$  and the phase angle  $\Phi$  is given by [3] [11],

$$\Phi = \omega_0 \tau = 2\pi f_{mod} \tau, \quad 2-11$$

where  $\Phi$  is smaller than  $2\pi$ . For  $\Phi$  larger than  $2\pi$ , the phase angle can be defined as

$$\tan(\Phi) = \omega_0 \tau = 2\pi f_{mod} \tau, \quad 2-12$$

where  $f_{mod}$  is the excitation light modulation frequency, and  $\Phi$  is the phase angle. Due to the non-linear nature of the tangent function, the modulation frequency has to be chosen carefully,

$$f_{opt} = \frac{1}{2\pi\sqrt{\tau_1\tau_2}}, \quad 2-13$$

where  $f_{opt}$  is the optimal modulation frequency,  $\tau_1$  and  $\tau_2$  are the upper and lower lifetime of analytical interest, which are defined by the measuring range.

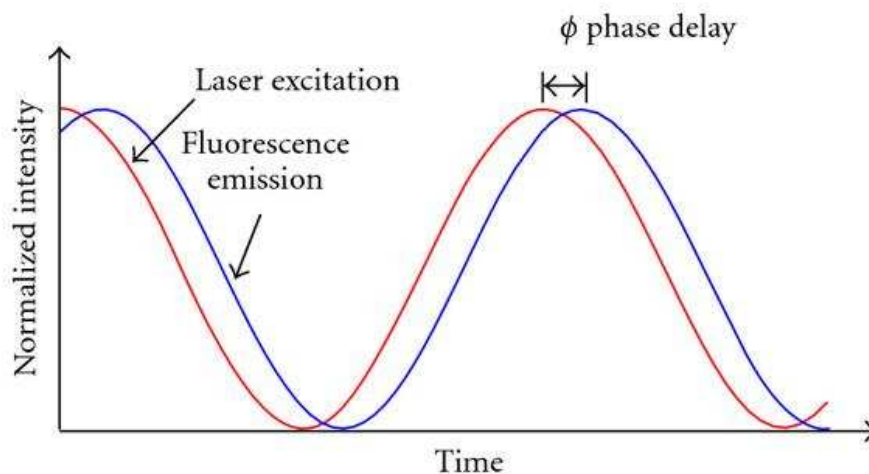


Figure 2.7. Illustration of frequency-domain fluorescence lifetime measurement. The excitation light (red) is modulated in amplitude at a frequency  $f_{mod}$ , while the fluorescence light (blue) is emitted with the same modulation frequency but with a phase shift in time,  $\Phi$ . For a single exponential lifetime, the value of the fluorescence lifetime is related by  $\tan(\Phi) = 2\pi f_{mod}\tau$ . Reproduced from Reference [10].

Comparing the two methods described above, there are obvious advantages and disadvantages with both methods. In the case of PL intensities measurement, the measured signals can depend on the surrounding environment's light conditions, the excitation light intensity, and the dark current of the detector. However, this dependency can be avoided by measuring those factors and subtracting them out of the measured signals to obtain the real PL intensities. Using the phase-angle detection method can avoid any problems that are inherent to the intensity-based measurements, but poor modulation frequency choices can be fatal to the measurements, because  $\tau_1$  and  $\tau_2$ , the upper and lower lifetime of analytical interest, are different case by case and often unknown. An inevitable problem with both methods is when the excitation photons carrying sufficient energy to excite the luminophore molecules causing photochemical irreversible destruction of the luminophore molecules, resulting in permanent changes in their PL

properties. This process is referred to as photobleaching, and it affects both the PL intensities and lifetime measurements. Photobleaching can be sufficiently controlled by reducing the intensity of the excitation light exposure, by using higher wavelength excitation light thus reducing the photon energy of the exposure light, or by employing luminophores that are less vulnerable to bleaching.

## 2.4 Fiber Optics

In a PL-based sensor system, transmitting the excitation light to the luminophores and collecting emission light back from the luminophores are the primary job of the optics in the system. Fibers are unequaled at this job in almost all practical applications due to their properties of long-distance and high-bandwidth transmission abilities, environmental robustness, ease of use, and low cost. An optical fiber typically consists of a higher refractive index core surrounded by a cladding material with a lower index of refraction. Light is kept in the core by total internal reflection to guide the electromagnetic waves along the fiber. Some fiber parameters are summarized in Table 2.1.

Table 2.1 Fiber Optics Parameters

Core radius	$a$
Core index	$n_1$
Cladding index	$n_2$
Normalized index difference	$\Delta = \frac{n_1^2 - n_2^2}{2n_1^2}$
Numerical Aperture (NA)	$NA = \sqrt{n_1^2 - n_2^2} = n_1 \sqrt{2\Delta}$

---

Allowed angles ( $\theta$ )	$\theta \leq \sin^{-1}\left(\frac{NA}{n_1}\right)$
Normalized frequency (the $V$ number)	$V = \frac{2\pi a}{\lambda} \sqrt{n_1^2 - n_2^2} = \frac{2\pi a}{\lambda} NA$
Number of modes ( $N_m$ )	$N_m = \frac{V^2}{2}$

---

Fibers that support many propagation paths or transverse modes are called a multi-mode fiber, which have a large  $V$ ; while those that only support a single mode are called single-mode fibers [12]. A single mode has the  $V$ -number value of 2.045. Multimode fiber is much more suitable to the applications of PL-based sensor systems because it is significantly easier for the emission light modes to match some modes that are supported. In other words, with larger  $NA$ , multimode fiber can capture emitted light propagating at a larger range of allowed angles,  $\theta$ , thus more emission power can be coupled using multimode fiber. Moreover, between the choices of a step-index multimode fiber and a graded-index multimode fiber, in the case of coupling non-spatially coherent light, step-index multimode fiber is a better choice because. However, multimode fiber is inherently more lossy than single mode. Because high-angle modes are weakly guided and so are vulnerable to scatter from irregularities in the fiber or to bending and pressure. It can be seen as a gradual decrease of the measured  $NA$  of the fiber as its length increases [13].

## 2.5 Optical Pathway Splitting Methods

The objective of the optics of the system is to connect the luminophores to an illumination source and a photodetector at the same time. Since an excitation source and

a photodetector are two separate devices that cannot allow illumination and viewing along the same optical path, the system requires a splitting configuration in the optical pathway. This dull but necessary work is commonly done by beam splitters or optical fiber coupler assemblies.

First, a beam splitter is essentially a dichroic mirror or filter, meaning an enhanced reflection coating on one side and often an anti-reflection coating on the other. In its most common form, a cube, it is made from two triangular glass prisms which are glued together at their base. The diagonal internal surface is coated with metal-dielectric coating that allows a nonpolarized even split of optical power between the two outputs. A schematic representation of a beam splitter used in a PL-based system is shown in Figure 2.8. Since the light encounters the beam splitter twice, once in the reflected excitation light and once in the transmitted emission light. The transmission efficiency of each encounter is 50%, so multiplying 50% by 50% yields the roundtrip optical efficiency is 25% with a 50:50 beam splitter. However, layers of different optical coatings with different indices of refraction and thicknesses can be designed to produce selectively constructive interference at certain wavelength and destructive interference at other wavelength in order to improve the efficiency ideally up to 100%. Beam splitter is a crucial part of most interferometers because its great performance in the wavefront preservation. When it comes to other field applications, the disadvantage of extreme sensitivity to shock and vibrations establishes that a beam splitter may not be superior to other choices.

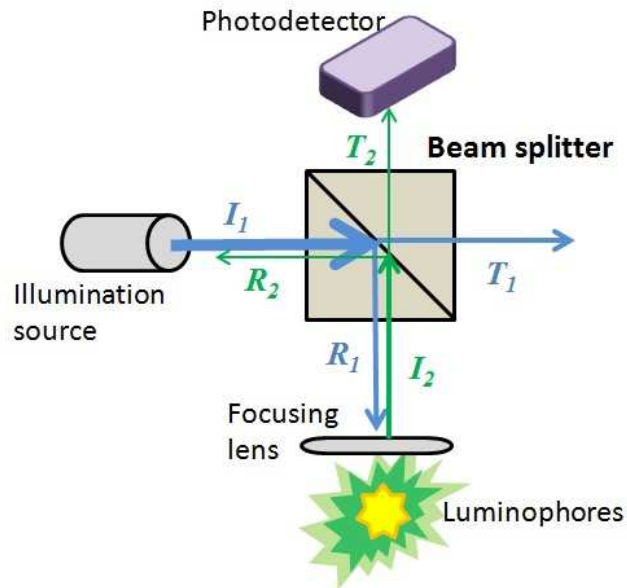


Figure 2.8. A schematic representation of a beam splitter used in a PL-based system, where  $I_1$  is the incident excitation light,  $T_1$  is the transmitted excitation light,  $R_1$  is the reflected excitation light,  $I_2$  is the incident emission light,  $T_2$  is the transmitted emission light, and  $R_2$  is the reflected emission light. The excitation light has a wavelength of  $\lambda_1$  and the emission light has a wavelength of  $\lambda_2$ .

Second, optical fiber coupler assemblies can be an alternative option than a beam splitter as the optical pathway splitting configuration. There are two kinds of fiber optic coupler assembly, fused fiber couplers and bifurcated fiber assemblies. Since the emission light is difficult to guide in a single-mode fiber with sufficient intensity, the fiber coupler assemblies we discuss here are multimode. A fused fiber coupler is usually made by fusing two fibers together and stretching the fused region until the coupling region diameter is slightly less than that of a single fiber [14], as shown in Figure 2.9 [15]. Sometimes, manufacturers have a known illumination source on one side of the fused region, and monitoring the two branches on the other side of the coupling region, and apply heat to fuse the coupling region while stretching the coupling region until the

desired splitting ratio achieved at the monitors. Moreover, the other widely used fiber optic coupler assembly is bifurcated fiber assemblies. A bifurcated fiber assembly is simply combining multimode optical fibers together with one end bundled together sharing the same jacket while the other end remain separate branches with each individual jacket, as shown in Figure 2.10. No coupling between individual fibers to each other ever occurs in the entire assembly.

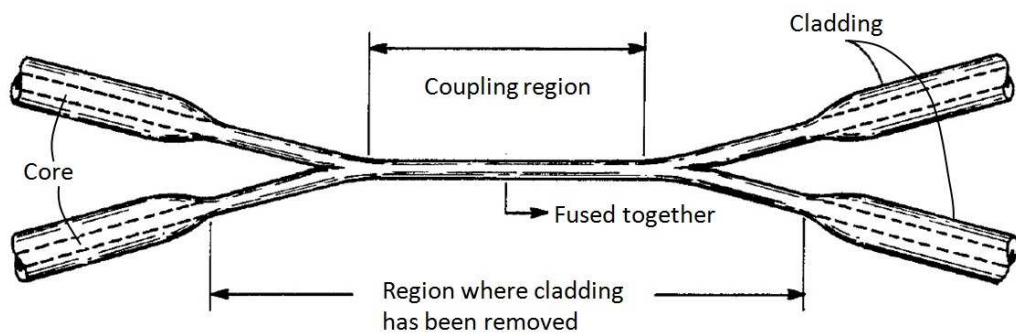


Figure 2.9. A schematic drawing of a 2×2 fused fiber coupler shows the coupling region between two originally separate fibers is fused together. Reproduced from Reference [14] and [15].

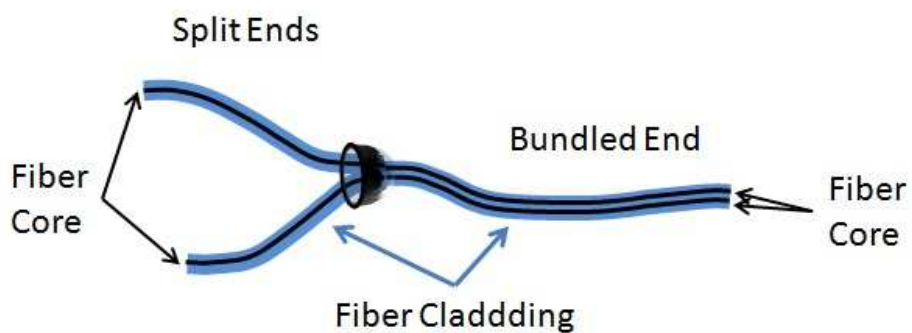


Figure 2.10. A schematic drawing of a 1×2 bifurcated fiber assembly.

Many factors during manufacturing can affect the fiber coupler assemblies, especially the fused fiber coupler. Provided that the taper is sufficiently gentle, the reflections are small, and the excess loss, defined as the power ratio of output to input, for large-core multimode splitters can be 1.5 dB, and some single-mode ones reach 0.1 dB [13]. With bifurcated fiber coupler there is less dependence on the fabrication but the configuration at the bundled end yields worse coupling performance. Moreover, back reflection and split ratio also play important roles in the whole system performance. Therefore, between the two choices of fiber coupler assemblies, one is not superior to the other. A quantitative comparison between the two approaches is included in Chapter 5 of this thesis.

## **2.6 Optical Detection Parameters**

In an optoelectronic system, the optical detector and its associated accessories are normally the most critical components of all optics in the system simply because to be able to extract any useful optical information requires the detector to be sufficiently sensitive. Optical signals can be lost due to the ineffective detectors, or bad optical characteristics matching between the light and the device, e.g. the responsivity of the detector is low at detecting wavelength. Also, even after the detector transferring the optical signal into electronic signals, the signal can still be swamped into the intrinsic noise of the detector. It is necessary to understand many parameters associated with different workings of numerous detectors. The signal-to-noise ratio, quantum efficiency, and responsivity will be discussed here.

First, signal-to-noise (SNR) is quite often the most straight forward measure of how much signal is corrupted by noise in many applications. SNR is defined as the signal power divided by the noise power. Notice SNR is defined in terms of power, and the SNR of the photocurrent power is square of the SNR of the optical power. This is because optical detectors are square-law devices, which means the electrical power resulting from the optical power of incident is proportional to the square of the optical power. This can be explained with the following. Every photon with a given frequency carries energy of  $h\nu$ , and the optical power is proportional to the number of photons in a fixed period of time onto a fixed area, in other words, photon flux. As the incident photons strike the detector, each photon transfers its energy to create an electron-hole pair, which is known as the photo-electric effect, hence, the photocurrent is proportional to the photon flux. The photocurrent power is proportional to the square of the current.

Second, in optical detection devices, the quantum efficiency (QE) is the most basic parameter of how efficient a detector is. The QE is defined as the percentage of incident photons that will create an electron-hole pair. Photographic film typically has a QE of much less than 10%, while charge coupled devices (CCDs) can have a QE of well over 90% at some wavelengths [13]. Since the shot noise is directly proportional to the square root of the number of photons collected, the QE can a major factor in SNR. Although cranking up the gain can reduce the effects of circuit noise, gain has no effect on shot noise.

Third, the responsivity of an optical detector is defined as the output photocurrent,  $I$ , divided by the incident optical power,  $P$ , shown in Eqn. 2-14 [13], usually expressed in amperes per watt,

$$R = \frac{I}{P} = M \frac{q_e}{h\nu} \eta_{QE}, \quad 2-14$$

where  $M$  is the intrinsic multiplication gain of the detector (unity for photodiodes because one photon creates one electron-hole pair; but not unity for photomultiplier because one photon generates multiple electrons),  $q_e$  is the charge of an electron,  $\eta_{QE}$  is the QE,  $h\nu$  is the energy carried by a single photon at a given frequency  $\nu$ . The responsivity is a useful parameter to look at because it takes in the consideration of both the intrinsic gain and the QE into the same parameter. QE of a photodetector is usually a strong function of wavelength, and working its advantage towards the benefits, for instance, having a high responsivity at desired wavelengths and cutoff at other wavelengths.

## 2.7 Workings of Optical Detectors

Among numerous kinds of photodetectors, photodiodes are the most widely used. A photodiode operates similarly to a PN junction or PIN structured semiconductor diode except for that the photosensitive areas are exposed. As photons strike the photodiode and create electron-hole pairs in or near the depletion region, as shown in Figure 2.11, of the junction, intrinsic or applied electric field in the depletion region separates the pairs before they recombine. The electric field sweeps the electrons towards the cathode and the holes towards the anode of the diode, and therefore, creates a photocurrent. The depth of the depletion region can be varied by applying a reverse bias voltage across the junction. The depletion region is important to photodiode performance since most of the sensitivity to radiation originates there [16]. With the photo-electric effect as its fundamental mechanism, photodiodes exhibit great linearity. The QE of the photodiodes are sufficiently high for many applications. Also, they are usually low cost. Integrating

arrays of silicon photodiodes with shift registers and on-chip amplifiers makes imaging array detectors, such as the charge-coupled device (CCD). CCDs are commonly used in spectrometers for PL-based sensor systems.

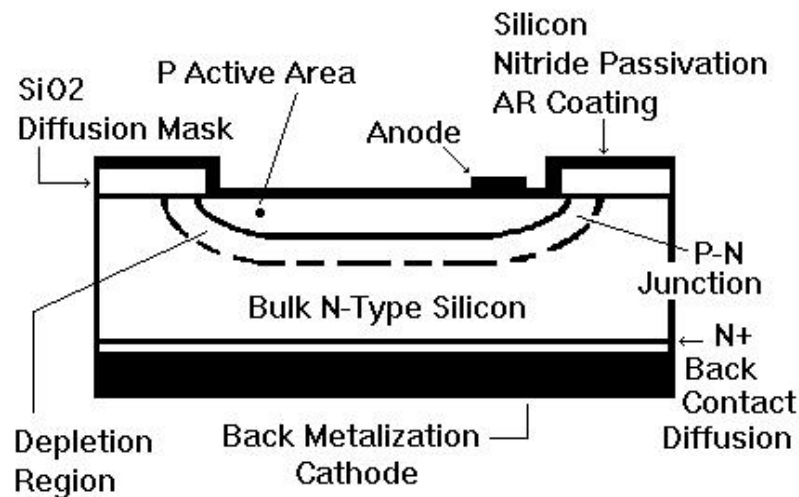


Figure 2.11. A structural illustration of a PN junction photodiode. Reproduced from Reference [16].

Despite operating at reverse or zero bias, photodiodes are also commonly operated near breakdown region and become highly sensitive photodetectors, known as avalanche photodiodes (APDs). By applying extremely high bias voltages across the diode, the photon generated electrons inherit enough energy to create more electrons via impact ionization. This intrinsic multiplying process results in a significant multiplication gain  $M$  in Eqn. 2-14.

Detection of extremely low intensity light signals is only limited by the shot noise in principles, however, in practice, Johnson noise and amplifier input noise can easily exceed the photocurrent signals. Photomultiplier tubes (PMTs) amplify the photoelectrons using the electron multiplication method before the signal gets buried in

the electronic noise. The operation of a PMT is explained in the following text, with the schematic of a PMT structure shown in Figure 2.12. As photons strike the photocathode, due to the photoelectric effect, the incident photons cause the photocathode to emit photoelectrons from its surface. Then the photoelectrons are accelerated and focused onto the first dynode due to the strong electric fields created by applied voltages. The dynodes are coated with materials that can easily have secondary electron emission. As the photoelectrons arrive the first dynode with higher energy, more low energy electrons are emitted, and these electrons in turn are accelerated toward the second dynode, and so on for 5 to 14 stages, before finally being collected by the anode, where the accumulation of charge results in a sharp current pulse indicating the arrival of a photon at the photocathode [17]. At this point, the photocurrent has been amplified well above the Johnson noise level of subsequent circuits. Although the amplification mechanism of the PMT is very effective, many issues still need careful attention to be paid, such as dark current, shock, drift, etc.

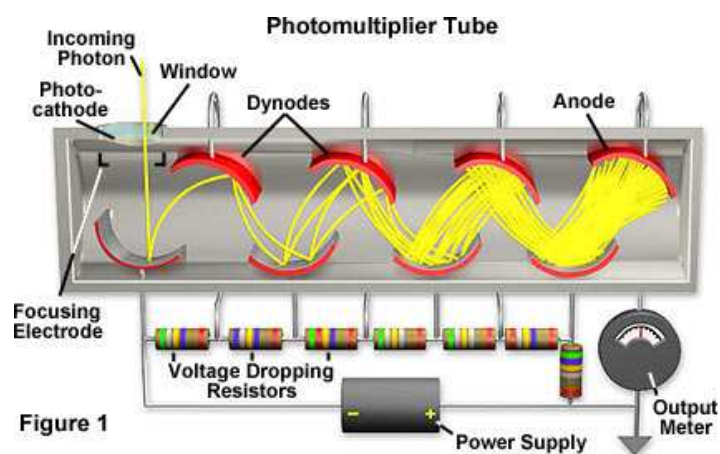


Figure 2.12. A schematic of PMT structure with a side-on design, where light enters the flat, circular top of the tube and passes the photocathode. Reproduced from Reference [17].

## 2.8 References

- [1] Otto S Wolfeis, "Fiber-Optic Chemical Sensors and Biosensors," *Analytical Chemistry*, vol. 72, no. 12, 2000.
- [2] Reardon F. Reardon, Zhong Zhong, and Kevin L. Lear, "Environmental Applications of Photoluminescence-Based Biosensors," in *Advances in Biochemical Engineering Biotechnology*. Berlin, Heidelberg: Springer-Verlag, 2009, ch. 116, pp. 99-123.
- [3] Joseph R. Lakowicz, *Principles of Fluorescence Spectroscopy*, 3rd ed. New York: Springer, 1983.
- [4] Bechara Kachar Donald Coling, "Principles and Application of Fluorescence Microscopy," *Current Protocols in Molecular Biology*, vol. 14, no. 10, May 2001.
- [5] Sean B. Pieper, "Optical Characterization of Phosphorescent Dyes for Biosensor Transducer Applications," Colorado State University, Fort Collins, Thesis 2008.
- [6] V. O. Stern and M. Volmer, "The fading time of fluorescence," *Physikalische Zeitschrift*, vol. 20, pp. 183-188, 1919.
- [7] Michael H. Stewart, Scott A. Trammell, Kimihiro Susumu, James B. Delehanty, Bing C. Mei, Joseph S. Melinger, Juan B. Blanco-Canosa, Philip E. Dawson, and Hedi Mattoussi Igor L. Medintz, "Quantum-dot/dopamine bioconjugates function as redox coupled assemblies for in vitro and intracellular pH sensing," *Nature Materials*, vol. 9, pp. 676-684, July 2010.
- [8] Johannes Pusterhofer, Marco J.P. Leiner, and Ottow S. Wolfbeis Max E. Lippitsch, "Fibre-optic oxygen sensor with the fluorescence decay time as the information carrier," *Analytica Chimica Acta*, vol. 205, pp. 1-6, June 1988.
- [9] C. A. Parker, "Photoluminescence of Solutions," *Angewandte Chemie*, vol. 81, pp. 1007-1008, 1968.
- [10] Omid Masihzadeh, Tim C. Lei, David A. Ammar, and Malik Y. Kahook Emily A. Gibson, "Multiphoton Microscopy for Ophthalmic Imaging," *Journal of Ophthalmology*, vol. 2011, p. 11, 2011.
- [11] Lakowicz JR. Berndt KW, "Electroluminescent lamp-based phase fluorometer and oxygen sensor," *Anal Biochem.*, vol. 201, no. 2, pp. 319-325, March 1992.

- [12] Robert D. Guenther, *Modern Optics*, 1st ed. United States: John Wiley & Sons, 1990.
- [13] Philip C. D. Hobbs, *Building Electrico-optical Systems: Making It All Work*, 1st ed., Joseph W. Goodman, Ed. New York, NY: Wiley & Sons, Inc., 2000.
- [14] Kenneth O. Hill, and Derwyn C. Johnson Brian S. Kawasaki, "Low Loss Access Coupler For Multimode Optical Fiber Distribution Systems," US4291940, Sept. 29, 1981.
- [15] Douglas R. Moore and Darrell L. Wuensch, "Multimode Fiber Optic Coupler and Method For Making," US4772085, Sep. 20, 1986.
- [16] Ernie Kim. A Primer on Photodiode Technology. [Online]. HYPERLINK "http://home.sandiego.edu/~ekim/photodiode/pdtech.html"  
<http://home.sandiego.edu/~ekim/photodiode/pdtech.html>
- [17] Mortimer Abramowitz and Michael W. Davidson. Hamamatsu articles. [Online]. HYPERLINK "http://learn.hamamatsu.com/articles/photomultipliers.html"  
<http://learn.hamamatsu.com/articles/photomultipliers.html>

## Chapter 3

# LITERATURE REVIEW OF FIBER OPTIC CHEMICAL SENSOR SYSTEMS

### 3.1 Introduction

This chapter reviews fluorescent and phosphorescent based sensor systems described in publications. PL based sensor systems have been widely applied in areas such as water analysis, biological and medical research, and industrial (bio)processes corrosion and combustion, therefore, numerous relevant studies have been published. This chapter groups related publications together in the following subjects. First, this thesis reviews a couple PL intensity-based fiber optic sensors systems with system configurations and experimental results. These systems have common properties such as using the Stern-Volmer equation for PL intensity being a function of the quencher concentration as the fundamental working principle of the system, using fiber-optics as the optical transmission component for their apparent advantages in field applications. Those systems do not have the ability to simultaneous detection multiple analytes. Second, two other systems are reviewed for their multi-analyte detection ability using the fluorophore-

quencher pair mechanism. Third, as mentioned in the previous chapter that due to the separation of the excitation source and the detection device for a fluorophore-quencher pair system, an optical pathway splitting mechanism is required. Many different methods of doing so have been reported, such as free-space coupling, fused fiber couplers and bifurcated cables. A comparison of those methods has been carried out from the related publications, as well as some inherent issues associated with certain devices have been investigated in the literature. Fourth, the Stern-Volmer equation has been adopted to quantitatively describe the quenching process, however, many papers have described some necessary modifications to the equation based upon the non-linearity in the Stern-Volmer equation observed from the experimental results. Some explanations and associated mathematical models have been reported and are reviewed in this chapter.

### **3.2 Intensity-Based Fiber Optic Sensor Systems**

Although the scope of this thesis does not expand to inorganic ion sensors, such as pH or oxygen sensors, with the quencher ions as the indicator of the luminophore-quencher pair detecting mechanism, the ion detection figure of merit is a critical parameter for understanding the system performance. Numerous fiber optic sensors have been reported for measurement of pH, oxygen and other quenchers, such as sulfite. Many sensor construction techniques have been applied including monoliths [1], thin films [2], micro-plates with sensing [3] spots and optodes including miniaturized micron-sized tips [4] and coated optical fibers [5]. However these systems have generally very similar structural configurations due to the sensing mechanism of the luminophore-quencher pair. Results are often reported in the form of normalized intensity or the Stern-Volmer ratio of  $I_0/I$  over the range of varying quencher concentrations.

Based on the luminophore-quencher detection mechanism, the system configuration for this type of experiments are generally similar to one another. Excluding the diversity in components, the common objective of the apparatus is to couple the excitation illumination source to the luminophore through a fiber optic and collect the PL light from the same luminophore and transport it to a photodetector.

Nivens et al. has demonstrated a single channel fiber optic fluorescent intensity-based sensor system for pH measurement. In Niven's system, a single fiber sensor is used as shown in Figure 3.1, the block diagram reconstructed from the description in Reference [6]. The absorption and emission spectra are measured with the lab-constructed system shown in the Figure 3.1, or with a UV-VIS spectrometer (Hewlett-Packard Model 8453). Two types of sensors are tested, and they are made by co-polymerizing tetraethylorthosilicate and silanol-terminated polydimethylsiloxane with 3-aminopropyltriethoxysilane (APTES) and/or 3-glycidoxypropyltrimethoxysilane (GPTMS). Both sensors are used in conjunction with fluorescein isothiocyanate (FITC), added to the dried sol-gel membranes; this dye addition method provides the advantage of fast pH response due to the reaction is only accessible with the surface amine groups, and long period of storage of the sensors.

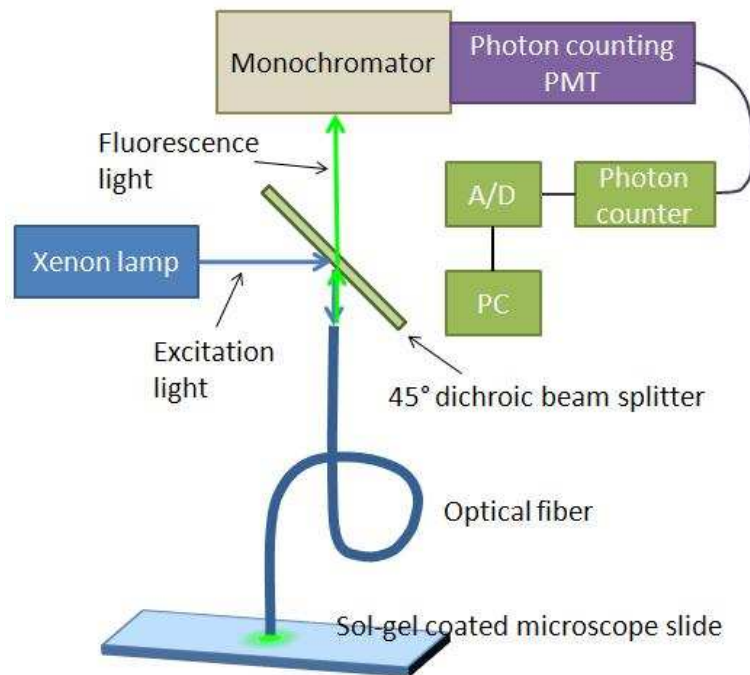


Figure 3.1. A system configuration block diagram reproduced from the description in Reference [6]. The components are a xenon lamp (Oriel, Stratford) light source, a 45° dichroic beam splitter (Chroma 507 DCSP), a 0.22 m single-beam excitation monochromator (SPEX Model 1681), a photon counting PMT (Hamamatsu Model R928P), a photon counter (EG & G Princeton Applied Research Model 1112, Princeton), analog-to-digital (A/D) converter (DGH Model D2141) and a PC connected to the A/D converter through a RS232 interface.

Similar configuration was adopted by Papkovsky [7] et al. in a phosphorescent intensity based sulfate sensing mechanism, where the sensing active areas are incorporated into the system fiber optics rather than separated from them as demonstrated by Niven et al. Using the compact configuration of the sensors has the obvious advantage of the ability of real-time measuring due to the separation of the sensing element and the analyte. Papkovsky's system has the configuration shown in Figure 3.2. The phosphorescent membrane as the sensing element is embedded with the fiber optics.

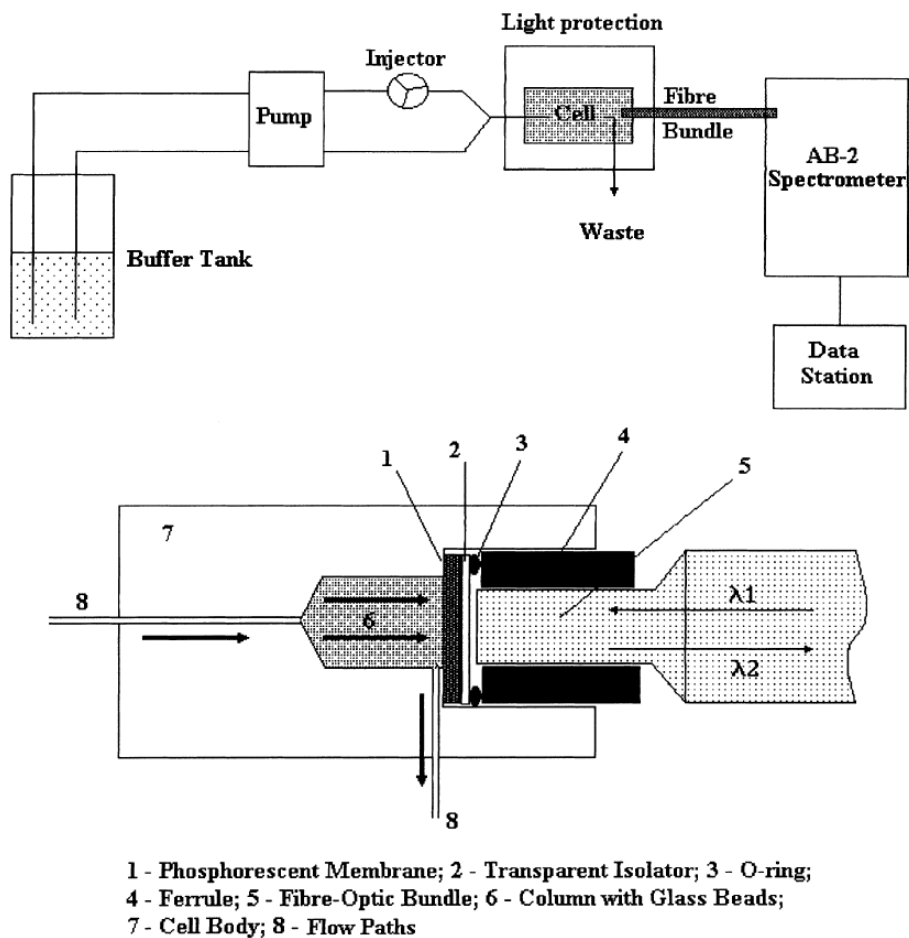
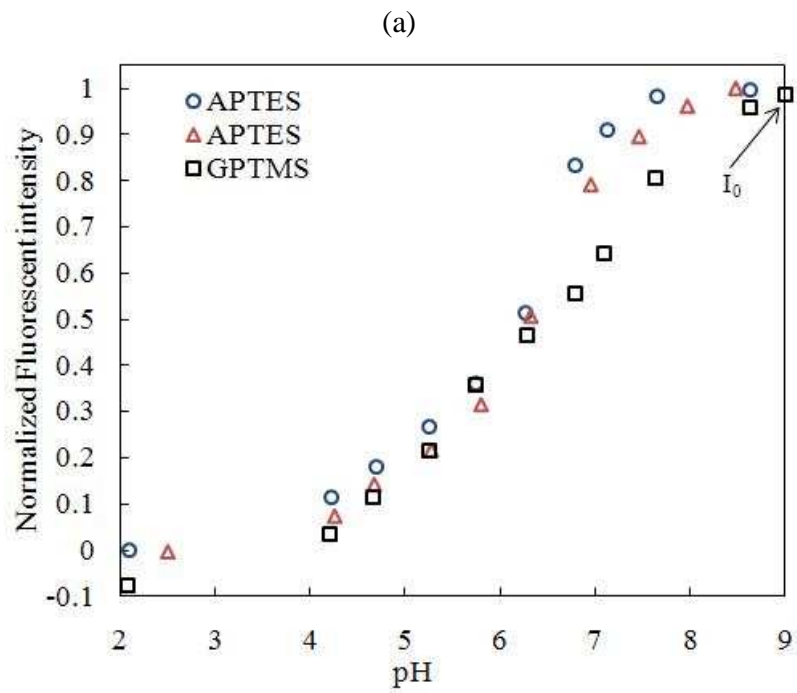


Figure 3.2. A block diagram of Papkovsky's system and the sensor tip in a flow cell fixture configuration. This figure is reproduced from Reference [7].

To enable to comparing the results of the two PL intensity-based fiber optic sensor systems, data has been extracted from the original publications and digitized using the GetData Graph Digitizer as shown in Figure 3.3 and Figure 3.4. Typically, the results of a PL intensity-based sensor are reported in forms of the calibration curves with the PL intensity being a function of the quencher concentration, as shown in Figure 3.3 (a) and Figure 3.4 (a); also results are often published in the form of the Stern-Volmer plot, which is the PL intensity in the absence of the quencher divided by the measured

intensities,  $I_0/I$ . This ratio is linearly related to quencher concentration, as shown in Figure 3.3 (b) and Figure 3.4 (b). The sensitivity of the sensor is often reported in the form of the Stern-Volmer constant,  $K_{sv}$ , which is the slope of the Stern-Volmer ratio  $I_0/I$  plot.



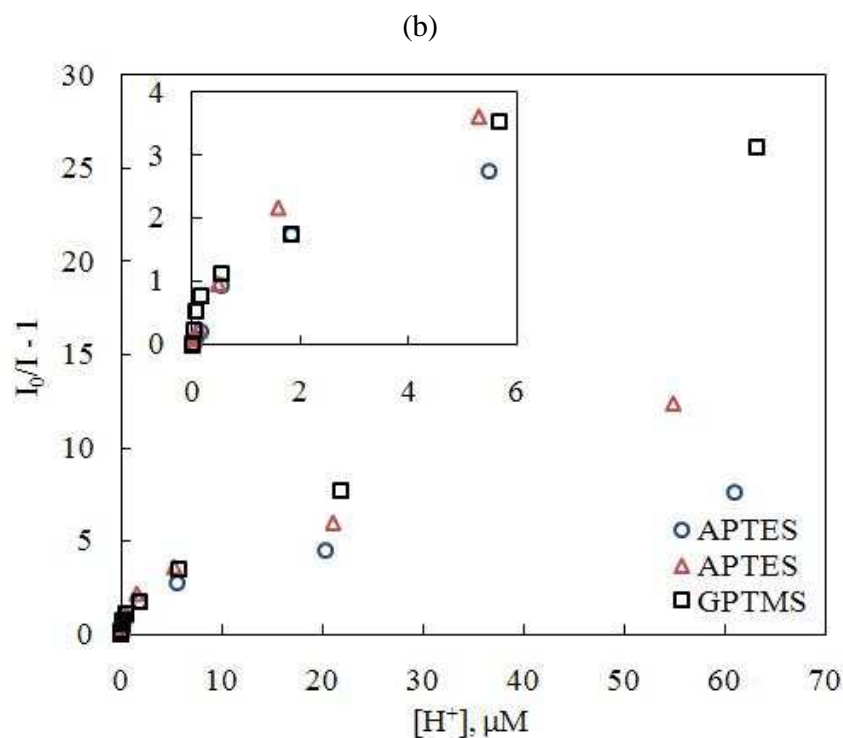
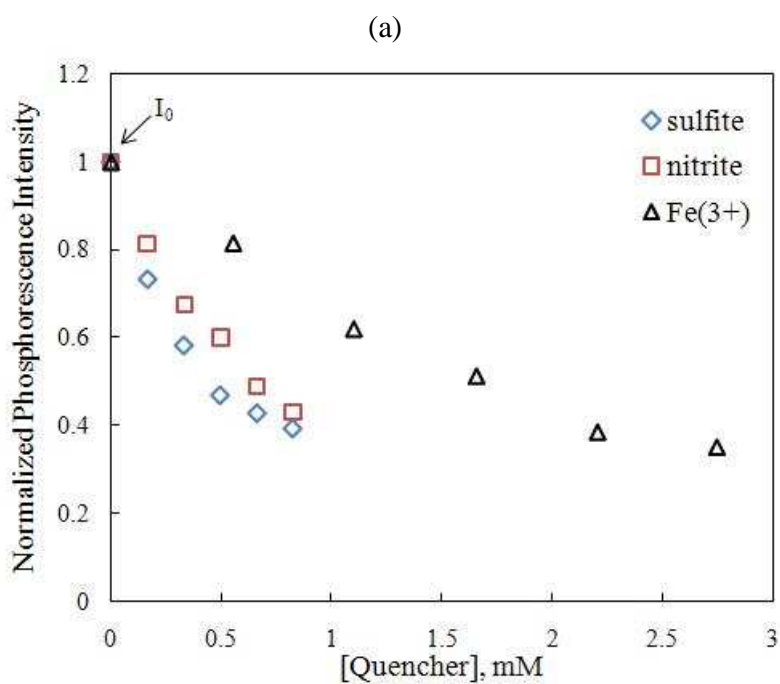


Figure 3.3. (a) The calibration curves of the Nivens' system with the fluorescent intensity normalized with the "unquenched" intensity  $I_0$  at the highest pH solution versus the pH values. Different curves indicate different sensor formulations, two APTES and GPTMS/APTES. Reproduced from Reference [6] (b) The Stern-Volmer ratio  $I_0/I$  versus the quencher,  $H^+$ , concentrations. Reproduced from Reference [6].



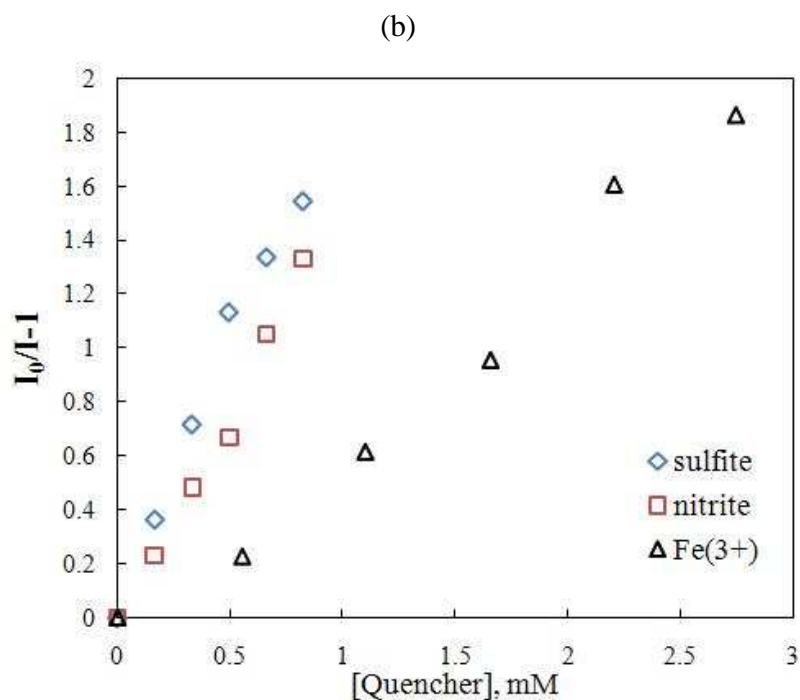


Figure 3.4. (a) The calibration curves of the Papkovsky's system with the phosphorescent intensity normalized with the intensity  $I_0$  with the absence of the quencher versus the quencher concentrations. Different curves indicate different types of quencher quenching the same sensor PtCP-BSA. Quenchers being tested here are sulfite, nitrite, and Fe(3+). Conditions: 10  $\mu\text{g/ml}$  PtCP-BSA in 0.05 M HCL (pH 1.3), air-saturated solution, 23  $^\circ\text{C}$ . Phosphorescence at 535/650 nm. Reproduced from Reference [7]. (b) A plot of the Stern-Volmer ratio  $I_0/I$  versus the quencher concentrations, with the quencher being three different types of sulfite ( $K_q = 1920 \text{ M}^{-1}$ ), nitrite ( $K_q = 1510 \text{ M}^{-1}$ ), and Fe(3+) ( $K_q = 664 \text{ M}^{-1}$ ). Reproduced from Reference [7].

### 3.3 Multi-Analyte-Capable Sensor Systems

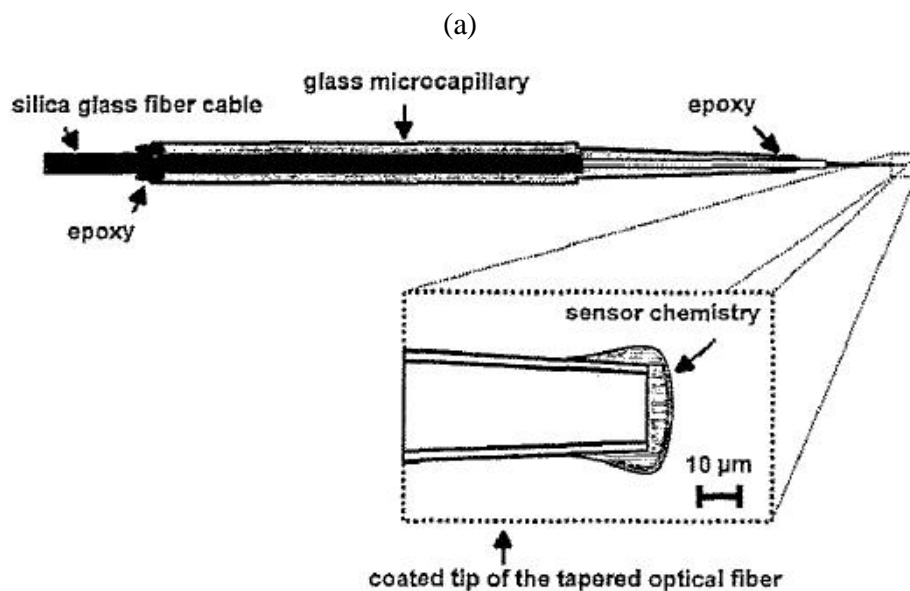
Most reported sensor systems or sensors are unlikely to be used for measuring multiple species of analyte, however, multi-analyte measurement capability is often required in practice. Biosensor systems are widely used and demanded in complex environments, such as ground water, body fluid, blood, and products in food processing industries, etc. These applications often require multiple chemical detection and/or monitoring simultaneously. The simple replica of the entire system for multi-analyte

measurements is not considered as a multi-analyte-capable sensor system in this work for performance comparison, and will be discussed as a single channel system.

A micro-optode array sensor system has been reported by Holst et al. [4]. The sensor relies on the basic oxygen-sensing mechanism using two types of sensors, ruthenium-II-tris-4,7,diphenyl-1,10-phenanthroline-ClO<sub>4</sub>, and platinum-octyethyl-porphine both immobilized in polystyrene matrices that have a good mechanical stability, as shown in Figure 3.5. The sensors are coated onto the tip of the tapered silica glass fiber of the micro-optodes, and each sensor is calibrated by a two-point calibration and using the modified (Eqn.3-1) [8] and ideal Stern-Volmer equations (Eqn. 2-2) to fit the calibration data.

$$\frac{\tau}{\tau_0} = \frac{0.85}{1 + k_q \tau_0 [Q]} + 0.15 \quad 3-1$$

The system adopted the phase-angle detection method as mentioned in Chapter 2.



(b)

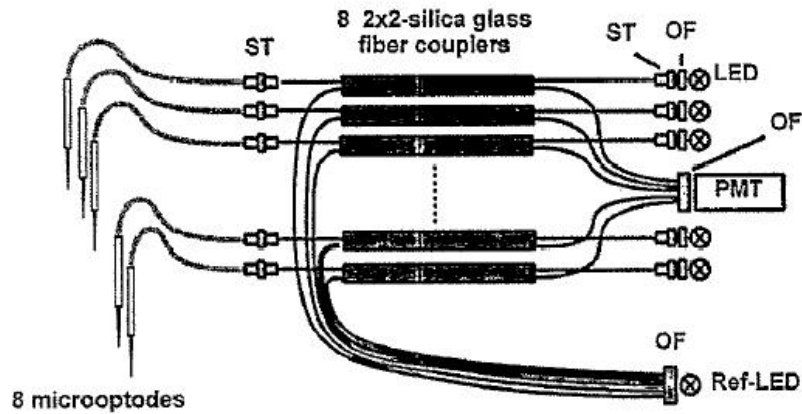


Figure 3.5. (a) Schematic drawing of an oxygen micro-optode. The oxygen indicator sensor layer is applied on to the tapered silica glass fiber by dip-coating. The fiber is fixed with epoxy in a glass micro-capillary for ease of handling. Reproduced from Reference [4]. (b) The optical setup of the micro-optode array sensor system. Eight micro-optodes are assembled in the way that the branches on the detector end are combined to a fiber cable and coupled via a 600  $\mu\text{m}$  silica-glass fiber and an optical filter in front of the PMT. Acronyms in the figure are: PMT, photomultiplier tube assembly; OF, optical filters; LED, light-emitting diode; Ref-LED, reference light emitting diode; ST, standard fiber connectors and receptacles. Reproduced from Reference [4].

The phase-angle detection adopted by Holst et al. is basically converting the phase angle between the excitation and the PL sinusoidal signals into a repetitive pulse whose width is related to the phase angle. An block diagram of the system design is shown in Figure 3.6. The PL signal gets picked up by the PMT, and the PMT outputs a current signal that is proportional to the PL optical power. The current signal from the PMT then gets converted into an amplified voltage proportionally. Then the voltage signal gets bandpass filtered at its peak frequency the same as the modulation frequency,  $f_{opt}$  from Eqn. 2-4, and becomes a signal with only one component at the modulation frequency. Then the signal gets amplified again and highpass filtered to reduce the amplifier offset influence. After that the “de-modulated” signal goes through a comparator or zero-

crossing-detector to transfer the sinusoidal shape into a rectangular signal. The excitation LED signal gets converted into a rectangular signal as well and is compared with the PL signal with a logical exclusive 'OR' (XOR). Now, the phase-delay of the PL signal is converted into a repetitive pulse, whose width is directly proportional to the phase-angle difference between the excitation and the PL. Eventually the pulse signal goes through a lowpass filter and yields a phase value ranged from  $0^\circ$  to  $180^\circ$  corresponding to 0 and 9.8V in the analog-to-digital (A/D) converter.

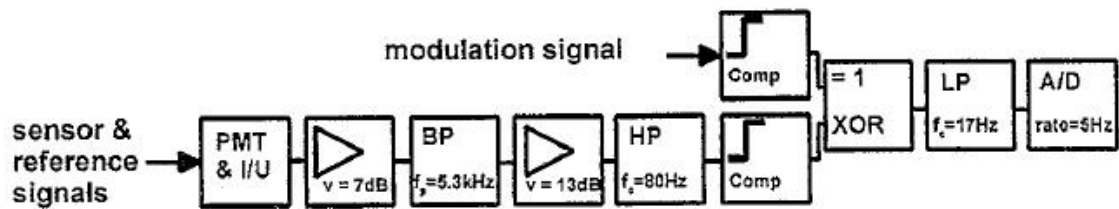


Figure 3.6. Schematic drawing of the control system of the phase-angle detection adopted by Holst et al. The acronyms in the figure are: PMT & I/U, photomultiplier tube and current to voltage converter;  $v$ , amplification; BP, electronic bandpass filter;  $f_p$ , the peak frequency of the bandpass filter; HP, electronic highpass filter;  $f_c$ , cutoff frequency; Comp, comparator; XOR, logical exclusive 'OR'; LP, electronic lowpass filter; A/D, analog-to-digital converter; rate, sampling rate of the converter. Reproduced from Reference [4].

Some designs of Holst's system are quite similar to this work, however, the differences, as concluded in Table 3.1, deserve attention. The comparison also includes the advantages (Pros) and the disadvantages (Cons) in Holst's system compared to the system of this thesis. Due to the difference in detection methods, the comparison excludes the differences in the electrical circuitry.

Unlike Holst's system that developed the multi-analyte-detection-capable sensor system by modifying a common single-channel sensing scheme [8], Wolfbeis et al. introduced a multi-channel system [3] that is very similar to the system often used

Table 3.1. A comparison of the optical apparatus configurations between this work and work done by G. Holst et al [4].

Comparing item	This work (Baseline)	G. Holst et al. (Comparing unit)	Pros	Cons
Source filter	Common source filter for all channels	Individual source filter for each channel	<ul style="list-style-type: none"> <li>• Less coupling loss</li> <li>• No source light cross-talk</li> </ul>	<ul style="list-style-type: none"> <li>• Non-uniformity</li> <li>• Expensive</li> <li>• Bulky</li> </ul>
Optode sensing tip fiber size	mm	$\mu\text{m}$	<ul style="list-style-type: none"> <li>• Sensing layer thickness coating uniformity</li> </ul>	<ul style="list-style-type: none"> <li>• Less coupling of PL</li> <li>• Non-uniformity in fiber tapering</li> <li>• Significant fabrication complexity and cost</li> </ul>
Detection method	Intensity	Phase-angle	<ul style="list-style-type: none"> <li>• Insensitive to the excitation power</li> <li>• Insensitive to <math>1/f</math> noise</li> </ul>	<ul style="list-style-type: none"> <li>• Fatal to incorrect choice of modulation frequency</li> </ul>
Ref-LED	No (Index matching material instead)	Yes	<ul style="list-style-type: none"> <li>• Ability to calibrate</li> </ul>	<ul style="list-style-type: none"> <li>• Back reflection interference</li> </ul>

for absorption and emission spectra measurements. In Wolfeis' work, many kinds of sensors were prepared for oxygen, pH, CO<sub>2</sub>, Potassium ion, Chloride, ammonia, urea, and glucose sensing. The corresponding indicators, polymers, and other parameters are compiled in Table 3.2. All the indicators are covalently immobilized to their corresponding polymers and then applied on top of a polyester foil that serves as an inert solid support. The sensor membranes then are punched in appropriate size and placed on either the bottom of the wells of a 96-well micro-plate using silicone vacuum grease, or inside a flow cell through which samples of known concentration of analyte or enzyme substrates were passed. A fiber-bundle connected to both a light source and a

spectrometer is used to couple the excitation and the emission light by placing the bundled end of the fiber in front of a sensor spot, as shown in Figure 3.7.

Table 3.2. Materials used for the set of luminescence decay time based sensors for measurement of blood gases, blood electrolytes, and enzyme substrates, and modulation frequencies employed in Wolfbeis' multi-analyte detection sensor system, reproduced from Reference [3].

Analyte	Polymer(s)	Indicator(s)	Additives	Modulation frequency (kHz)	Max change in decay time ( $\Delta\tau$ ), ns
pH	Hydrogel	Ru(didipy)/N9 <sup>a</sup>	None	75	740
Oxygen	Ormosil	Ru(dpp)	None	45	3100
CO <sub>2</sub>	Ethyl cellulose	Ru(didipy)/TB <sup>b</sup>	TOA	75	780
CO <sub>2</sub>	Buffer-in-silicone emulsion	Ru(pzth) <sub>3</sub> <sup>c</sup>	None	180	160
Potassium	PVC and CPDDE	Ru(didipy)/BTB <sup>d</sup>	Valinomycin	90	30 at pH 7.4 180 at pH 8.7
Na <sup>+</sup> , Ca <sup>2+</sup>	PVC and CPDDE	Ru(didipy)/BTB <sup>d</sup>	Ion carriers	90	--
Chloride	PVC and CPDDE	Ru(didipy)/BTB	TDMA-Cl	90	250
Ammonia	PVC/plasticizer	Ru(didipy)/CPR <sup>e</sup>	None	90	320-380
Urea	Carboxy-PVC/plasticizer	Ru(didipy)/CPR <sup>e</sup>	None	90	320-450
Glucose	Hydrogel	Ru(dipy)-BA	None	--	--

All sensors operated at excitation/emission wavelength of 465/610 nm

<sup>a</sup> A reactive indicator dye

<sup>b</sup> Thymol blue

<sup>c</sup> Excitation/emission wavelength of 450/635 nm

<sup>c</sup> 120 kHz are best

<sup>d</sup> Bromothymol blue

-

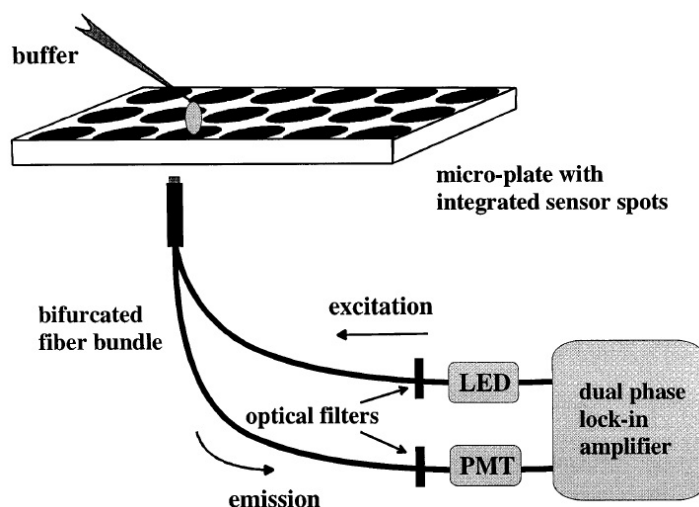


Figure 3.7. A schematic of the system setup of Wolfbeis' multi-analyte system for measurement of decay times of sensor spots contained in a micro-plate and covered with a sample. Reproduced from Reference [3]. The optical system consists of a blue LED as a light source ( $\lambda_{\text{peak}} = 470 \text{ nm}$ , NSPB 500, Nichia), a blue glass filter (BG 12, Schott), a bifurcated glass fiber bundle ( $\text{Ø} = 2\text{mm}$ ), an optical filter at the emission side (cutoff wavelength = 570 nm, OG 570, Schott), a red-sensitive PMT (H5701-02, Hamamatsu), a dual-phase lock-in amplifier (DSP 830, Stanford Research).

Although, Wolfbeis' work demonstrated excellent design and performance with the multi-analyte detection system, when implementing this system in practice, there are still a few issues worth paying attention to. First, the micro-plate design requires the analyte to be brought to the measurement site, and this requirement frustrates the *in situ* measurements. Wolfbeis et al. mentioned in the text that the sensing spot can be integrated in a flow cell where the analyte can pass through. This can be used along with a pumping system to achieve the *in situ* measurements. Second, Wolfbeis et al. did not describe in the paper a method for fiber bundle displacement. Aligning the fiber bundle with each sensor spot can be tedious and difficult in practical applications, because not only the size scale of the fiber and sensor pots are small, but also, the incident angle of

the fiber also plays an important part. A tiny misalignment can result in insufficient coupling, or cross-talk from adjacent sensor spots causing incorrect results.

### 3.4 Fiber-Optic Splitting Mechanism

As mentioned in Section 5 of Chapter 2, the objective of the optics of the system is to connect the luminophores to an illumination source and a detection unit at the same time. Since an excitation source and a detection unit are two separate devices that cannot allow illumination and viewing along the same optical path, the system requires a splitting configuration in the optical pathway. Because many excellent qualities of the optical fiber assembly, the fiber optic is often chosen over other beam splitting methods. However, few publications have studied some inherent issues with using a fiber optic in PL sensing related applications.

Valledor et al. [9] pointed out that the total optical power that gets coupled back to the detector at the tip of a fiber optic, where the sensor film or membrane is placed, is composed of components other than just the emission PL. Both of the cases of ‘wavelength-ratiometric methods’ and ‘dynamic-ratiometric methods’ that Valledor et al. analyzed in the paper, are intensity based methods; in other words, the emission PL intensity is a critical parameter in Valledor’s work as well as most other fiber-optic sensor systems. In Valledor’s work, the total optical power at the detector end is composed of three kinds of optical power, luminescence,  $I_{fluor}$ , specular reflectance,  $I_{SR}$ , and diffuse reflectance,  $I_{DR}$ ; they are defined as:

$$I_{fluor} = K_1 \cdot I_{ex} \cdot [Ind] \quad 3-2$$

where  $K_I$  is the proportionality constant that contains the absorption coefficient and the quantum yield of the sensors and the capability of the optical fiber in collecting and transmitting the light, and  $[Ind]$  is the indicator (the dye molecules) concentration.

$$I_{SR} = K_2 \cdot I_{ex} \quad 3-3$$

where  $K_2$  is the fraction of the reflected excitation light due to the refractive indices mismatch at the fiber-sensor interface defined by Snell's law. The specular reflectance,  $I_{SR}$ , is referred to as the back reflection in this work.

$$I_{DR} = -K_3 \cdot I_{ex} \cdot [Ind] \quad 3-4$$

where the diffuse reflectance,  $I_{DR}$ , is pH-dependent and  $K_3$  is a negative proportionality constant that is experimentally obtained. A schematic illustration of this process at the fiber-sensor interface is shown in Figure 3.8.

Velledor et al. introduced two methods to distinguish the three types of optical power at the detector end, the wavelength ratiometric method and the dynamic ratiometric method. Essentially the difference between the two methods is that the wavelength ratiometric method uses the optical filters while the dynamic ratiometric method digitizes the signals and separate them using digital signal processing based on their frequency components. The schematics of the two methods are shown in Figure 3.9.

The first method, wavelength ratiometric method, uses a bifurcated cable at the sensing end to collect the fluorescence emission and reflectance simultaneously and then appropriate wavelengths are selected by means of two bandpass optical filters, central

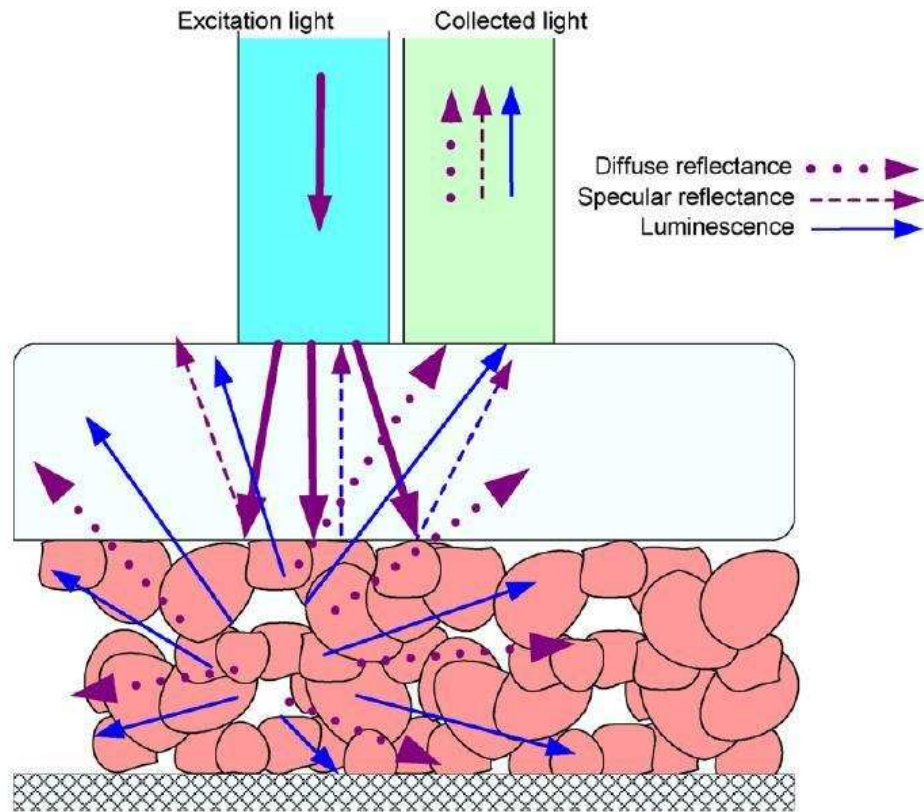


Figure 3.8. Different optical signals present in the collected light based on the reflectance measurements shown in Figure 3.9. Reproduced from Reference [9].

wavelengths at 550 nm and 470 nm for fluorescence emission and reflected excitation light respectively. Two Si photodiodes whose spectral responses are adapted to the emission of the chemical sensors are used. After the optical signals are interpreted into photocurrent signals, a transimpedance circuit is used to transfer the currents into voltages. As the excitation light is modulated sinusoidally at a fixed frequency, the fluorescence emission light signals can be separated from the ambient light or the diffuse reflectance,  $I_{DR}$ ; by implementing a band pass filter whose central frequency is the same as the excitation source modulation frequency.

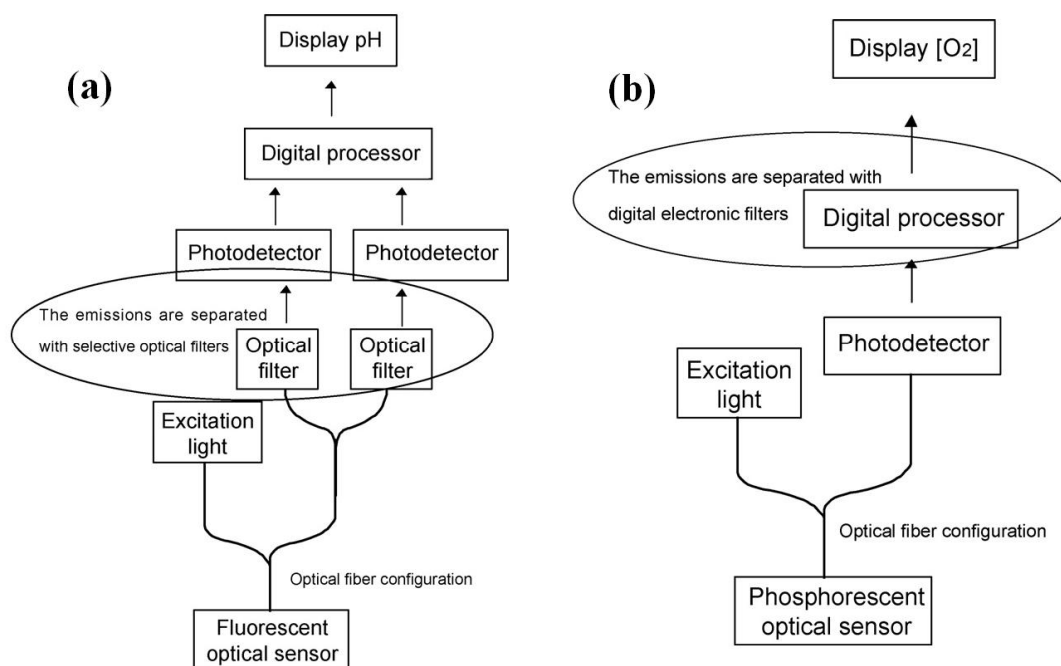


Figure 3.9. (a) Schematic instrumental setup of the wavelength ratiometric method with the separation mechanism being two bandpass optical filters. Reproduced from Reference [9]. (b) Schematic instrumental setup of the dynamic ratiometric method with the separation mechanism being the digitization of the signals and the digital signal processing based on the signals frequency components. Reproduced from Reference [9].

The second method, the dynamic ratiometric method, eliminates the duplicated photodiodes and optical filters, instead, uses a single low noise photodiode and a high gain transimpedance amplifier ( $10^8$  V/A). At the same time, the sinusoidally modulated excitation source is monitored using a less expensive photodiode. Then, the electronic filtering stage is used to separate the analyte dependent signal from the reference signal using a digital filter with a “Digital Signal Processor” (DSP) since an analog filtering device is not selective enough for this application.

Comparing both methods in Valledor’s work, there are some significant advantages as well as disadvantages of each method. Using the optical filtering mechanism, the

wavelength ratiometric method system responds fast enough to allow fluorescent sensor measurements where the lifetime is in the range of nanoseconds. However, the method adopts the two sets of instruments for two light channels, and the publication pointed out that this mechanism has a major drawback with the redundancy of instrumentation. Also, two stages of bifurcating the light pathways significantly decreases the intensity level of the optical signals that reaches the photodetector. Moreover, the imperfect filtering of the optical filters introduce interference to the detected optical signals. The dynamic ratiometric method substitutes the optical filtering with the digital filtering to resolve the redundancy problem in instrumentation. However, the digital filtering also slows down the process so that only phosphorescence lifetime (microseconds range) is within the detection range of the system.

Other than the optical splitting fiber assembly, bifurcated fiber assembly, used in Valledor's system, another widely used assembly is the fused fiber coupler. In many applications, the multimode fiber assemblies are considered for their better coupling, large core radius, and large numerical aperture. Due to the different fabrication procedures, as mentioned in Chapter 2, a bifurcated fiber assembly and a fused fiber coupler have very distinctive properties and therefore performances in many figures of merit. In sets of experiments carried out by Yasin et al., the two types of fiber assemblies are compared in terms of the performance as probes in displacement sensors [10].

Yasin et al. compared a 16:1 plastic multimode bifurcated fiber assembly and three plastic multimode fused fiber couplers with various coupling ratios such as 50:50, 90:10, and 80:20. The instrumentation setup of the experiments with both kinds of the fiber assemblies are shown in Figure **3.10**.

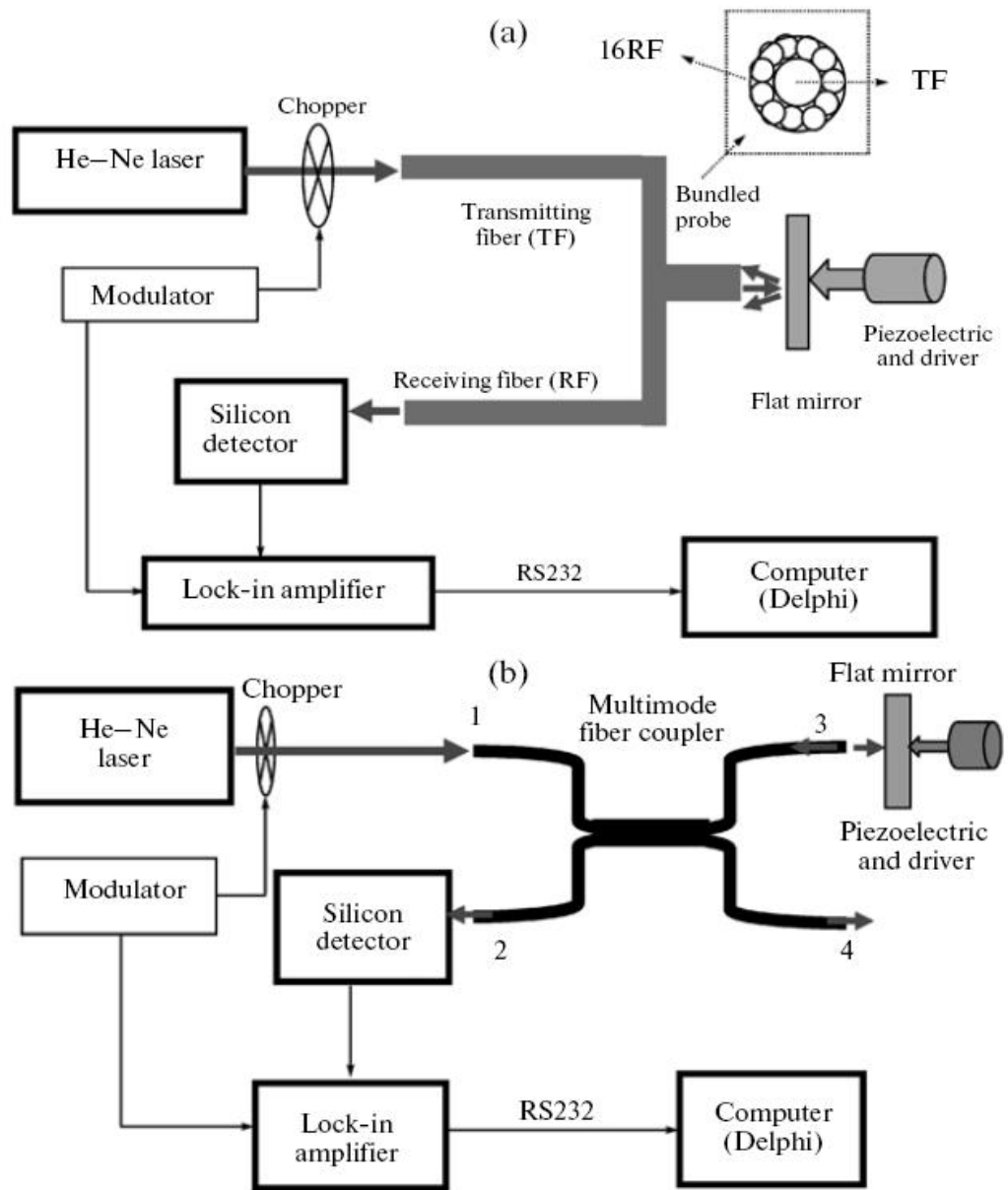


Figure 3.10. Schematic of the experimental setup of the displacement sensor using (a) a 16:1 plastic multimode bifurcated fiber assembly and (b) a plastic multimode fused fiber coupler. Reproduced from Reference [10].

In the first experiment with the bifurcated fiber assembly, the single inner core (diameter of 1 mm) branch of the assembly is connected to the light source, while the 16 outer core (diameter of 0.25 mm) branches are connected to the detector. Ideally, this

bifurcated fiber assembly has 3 dB coupling since the overall cross-section area of the 16 core is the same as the single core. In the experiments, a flat mirror is used to provide the necessary reflection that will be captured by the receiving fibers. In the second experiment, a similar setup as Figure 3.10(a) is used, except the bifurcated fiber assembly is replaced with a fused fiber coupler.

Although the paper compared the two types of fiber assemblies in terms of the performance of many figures of merit, such as the sensitivity, linear range, and resolution of the sensor, these results only apply to the displacement sensors, and thus are not directly applicable to the PL intensity-based sensor systems. However, a few conclusions drawn from the experimental results are useful in gaining intuition about those two types of fiber assembly. The results shown in Figure 3.11 are the output voltage, which is proportional to the optical power being reflected back into the fiber assembly from the flat mirror, with the displacement sensor using a bifurcated fiber assembly or a 2×2 fused fiber coupler. Some conclusions we can get from these graphs that are valuable towards a PL intensity-based sensor system are the following. First, when the displacement is zero, the reflected optical power is zero with a bifurcated fiber assembly; and this is due to the fact that transmitting and receiving are from different fiber cores. When using a bifurcated fiber assembly in a PL-intensity sensor system, not only the connecting device at the bundled end has to have an equal or greater cross section area as the total area of the bundled end, but also a non-contact coupling is a superior choice than an in-contact coupling. On the contrary, an in-contact coupling achieves its maximum coupling with a fused fiber coupler. Second, the maximum reflected optical is obtained with a splitting ratio of 50:50. The maximum reflected optical power obtained from a fused fiber coupler

is still about 4 times smaller than the reflected optical power obtained from a bifurcated cable with the same cross section area. This is due to the fused fiber coupler's insertion loss, mostly from the fused region, is significantly greater than that of a bifurcated fiber assembly.

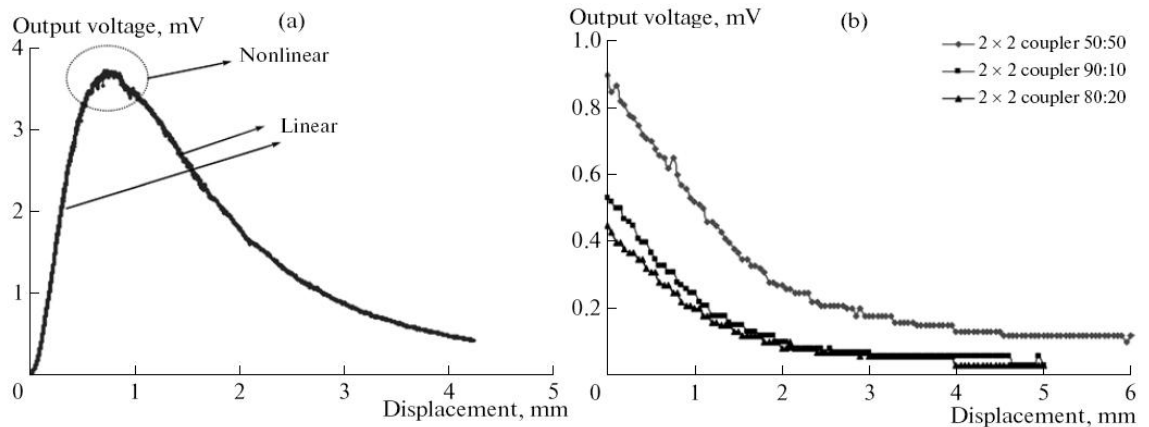


Figure 3.11. The output voltage of the lock-in amplifier as a function of displacement using (a) a 16:1 plastic multimode bifurcated fiber assembly and (b) a 2×2 plastic multimode fused fiber coupler with splitting ratio of 50:50, 90:10 or 80:20. Reproduced from Reference [10].

### 3.5 Non-idealities in Stern-Volmer Relationship

The Stern-Volmer kinetic relationship was first published in 1919 by Von O. Stern and M. Volmer [11] to quantitatively define the quantum yields of photophysical processes (e.g. fluorescence or phosphorescence) or photochemical reactions (usually reaction quantum yield) with the concentration of a given reagent which may be a substrate or a quencher [12]. It states that the ratio between the unquenched emission intensity and the emission intensity in presence of the quencher is linear to the quencher concentration with a slope of the Stern-Volmer constant,  $K_{SV}$ , and an offset of 1.

However, some publications have discovered some factors could cause alterations of the Stern-Volmer relationship.

During the quenching process of the fluorophore, there are two types of quenching, collisional (dynamic) quenching and static quenching. The collisional (dynamic) quenching is quantitatively described by the Stern-Volmer equation, with the Stern-Volmer quenching constant being represented by  $K_D$  when the quenching is known to be dynamic, otherwise  $K_{SV}$ . Quenching can also occur as a result of the formation of a nonfluorescent ground-state complex between the fluorophore and quencher. When this complex absorbs light, it immediately returns to the ground state without emission of a photon. Such a process is defined as the static quenching. Both the collisional (dynamic) quenching and the static quenching are linearly dependent on the quencher concentration, as illustrated in Figure 3.12. The two quenching processes can be distinguished by their differing dependence on temperature, as shown in Figure 3.12, and viscosity, or preferably by lifetime measurements. Higher temperatures result in faster diffusion and hence larger amounts of collisional quenching; also, higher temperature typically results in the dissociation of weakly bound complexes, and hence smaller amounts of static quenching. [13]

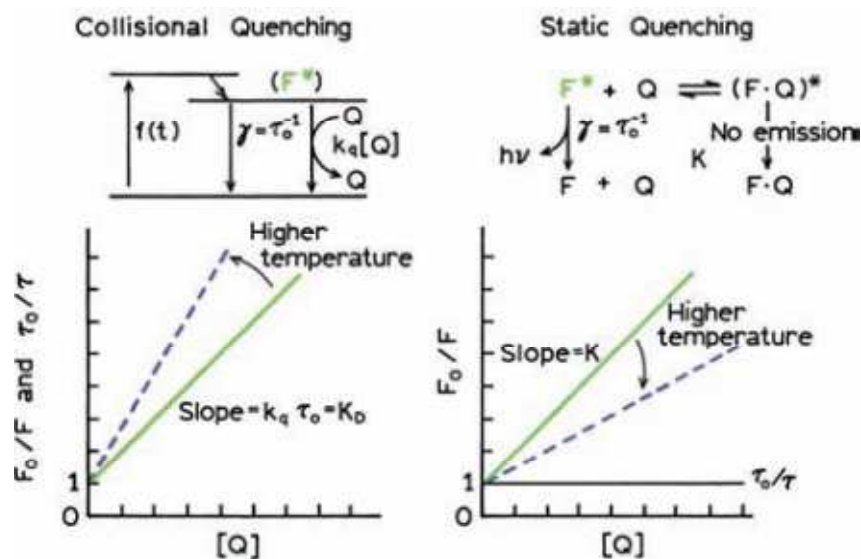


Figure 3.12. Comparison of dynamic and static quenching. Reproduced from Reference [13].

Although both types of quenching are linearly dependent on the quencher concentration, in many instances, the fluorophore can be quenched by both mechanisms with the same quencher. The characteristic feature of the Stern-Volmer plots in such circumstances is an upward curvature, concave towards the y-axis (positive second derivative), as shown in Figure 3.13 (left). A modified form of the Stern-Volmer equation for describing the case where both types of quenching processes is

$$K_{app} = \left[ \frac{F_0}{F} - 1 \right] \frac{1}{[Q]} = (K_D + K_S) + K_D K_S [Q], \quad 3-5$$

where the modified apparent quenching constant,  $K_{app}$ , which has its plot versus the quencher concentration to yield a straight line with an intercept of the sum of the dynamic and static quenching constants,  $K_D + K_S$ , and a slope of the multiple of the two,  $K_S K_D$ , as shown in Figure 3.13 (right).

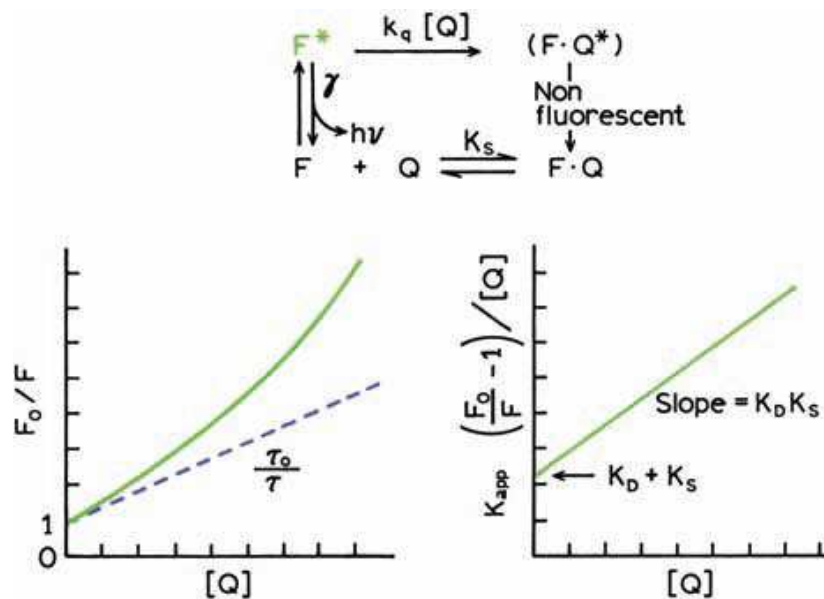


Figure 3.13. Dynamic and static quenching of the same population of fluorophores. Reproduced from Reference [13].

Many publications have studied the fluorescence inner filter effects and their impact on the non-linearity of the Stern-Volmer relationship. The inner filter effects is defined by the Compendium of Chemical Terminologies as, first, an apparent decrease in emission quantum yield and/or distortion of bandshape as a result of reabsorption of emitted radiation in an emission experiment, and second, absorption of incident radiation by a species other than the intended primary absorber during a light irradiation experiment [14]. This effects often cause the observed fluorescent intensity to be lower than the expected value at a given quencher concentration, and therefore, causes the Stern-Volmer plot to curve upward with increasing quencher concentration (a positive second derivative). Because of the nonlinearity of the Stern-Volmer plot, one cannot determine the quenching constant,  $K_{SV}$ . Such phenomena have been reported in numerous papers, such as Reference [15], [16], and [17]; in which mathematical models

have been given for a modified Stern-Volmer quenching constant,  $K_{SV}$ . Regardless of the quencher being used, it is important to determine if the inner filter effects are significant, and furthermore, correct the observed fluorescence intensities based on the effects. The lifetime-based fluorescence measurements are independent of the inner filter effects due to the fact that lifetime is independent of the total intensity.

In some other cases, the Stern-Volmer is observed to curve downwards towards the  $x$ -axis, such as in Reference [18], which is characteristic of two populations of fluorophore, one of which is inaccessible to the quencher. A mathematical model of the fractional inaccessibility of fluorophore can be described as the following. Suppose there are two populations of fluorophores, one of which is accessible to quenchers,  $a$ , and the other being inaccessible,  $b$ . Then, the total observed fluorescent intensities,  $I_0$  and  $I$ , being in the absence and in the presence of the quencher respectively, are defined as,

$$I_0 = I_{0a} + I_{0b} \quad 3-6$$

$$I = I_a + I_b \quad 3-7$$

Assume the accessible fluorophore fraction is  $f_a$ , thus the inaccessible fraction becomes  $(1-f_a)$ , as defined in an equation as

$$f_a = \frac{I_{0a}}{I_{0a} + I_{0b}} \quad 3-8$$

Then the observed fluorescent intensity in the presence of the quencher becomes

$$F = \frac{I_{0a}}{1 + K_a[Q]} + F_{0b} = \frac{\frac{1}{f_a} I_0}{1 + K_a[Q]} + I_{0b} \quad 3-9$$

where  $K_a$  is the Stern-Volmer quenching constant of the accessible fraction. Subtraction of Eqn. 3-9 from Eqn. 3-6 yields

$$\Delta I = I_0 - I = \frac{1}{f_a} I_0 \left( \frac{K_a [Q]}{1 + K_a [Q]} \right) \quad 3-10$$

Division of Eqn. 3-6 by Eqn. 3-10 yields the modified form of the Stern-Volmer equation:

$$\frac{I_0}{\Delta I} = \frac{1}{f_a K_a [Q]} + \frac{1}{f_a} \quad 3-11$$

A plot of the modified form of the Stern-Volmer equation as a function of  $1/[Q]$  yields  $f_a^{-1}$  as the intercept and  $(f_a K_a)^{-1}$  as the slope, as shown in Figure 3.14. Similar non-ideality behaviors were observed in experimental work presented in the later chapter of this thesis, a mathematical model is developed to describe both the fractional accessibility introduced here and another factor.

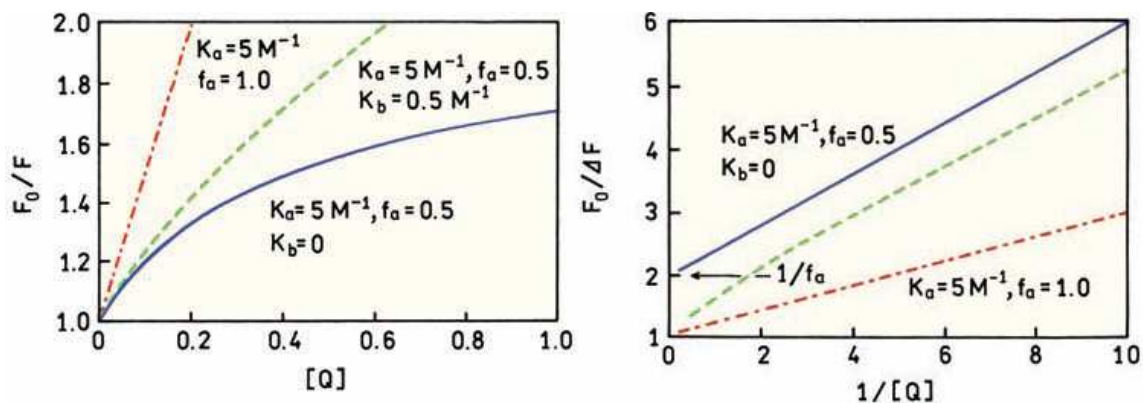


Figure 3.14. Stern-Volmer (left) and modified Stern-Volmer (right) plots for two populations of fluorophores. Red dash-dotted lines show all fluorophores are accessible ( $f_a = 1$ ), green dotted lines show half of the fluorophores are inaccessible ( $f_a = 0.5$ ) with the quenching constant of the inaccessible fluorophores  $K_b = 0.5 \text{ M}^{-1}$  being one-tenth of the quenching constant of the accessible population  $K_a$ . Reproduced from Reference [13].

### 3.6 References

- [1] C. Rottman et al., "Doped Sol-Gel Glasses As pH Sensors," *Materials Letters*, vol. 13, no. 6, pp. 293-298, May 1992.
- [2] S. C. Kraus, R. Czolk, J. Reichert, and H. J. Ache, "Optimization of the Sol-Gel Process for the Development of Optochemical Sensors," *Sensors and Actuators B-Chemical*, vol. 15, no. 1-3, pp. 199-202, Aug 1993.
- [3] O. S. Wolfbeis et al., "Set of luminescence decay time based chemical sensors for clinical applications," *Sensors and Actuators B*, vol. 51, no. 1-3, pp. 17-24, Aug 1998.
- [4] G. Holst, R. N. Glud, M. Kuhl, and I. Kilmant, "A Microoptode Array for Fine-Scale Measurement of Oxygen Distribution," *Sensors and Actuators B-Chemical*, vol. 38, no. 1-3, pp. 122-129, Jan 1997.
- [5] Z. J. Yi, Z. Zhong, C. Busse, K. F. Reardon, and K. L. Lear, "A Multi-Channel Fiber Optic Fluorescence Detection System for Multiplex Biosensor Arrays".
- [6] D. A. Nivens, Y. Zhang, and S. M. Angel, "A Fiber-Optic pH Sensor Prepared Using a Base-Catalyzed Organo-Silica Sol-Gel," *Analytica Chimica Acta*, vol. 376, no. 2, pp. 235-245, Dec 1998.
- [7] D. Papkovsky et al., "Optical Sensing of Sulfite With A Phosphorescent Probe," *Analytica Chimica Acta*, vol. 374, no. 1, pp. 1-9, Nov 1998.
- [8] I. Kilmant, M. Ktil, R. N. Glud, and G. Holst, "Optical measurement of oxygen and temperature in microscale: strategies and biological applications," *Sensors and Actuators B*, vol. 38, no. 1-3, pp. 29-37, Feb 1997.
- [9] M. Valledor et al., "A critical comparison between two different ratiometric techniques for optical luminescence sensing," *Sensors and Actuators B: Chemical*, vol. 139, no. 1, pp. 237-244, May 2009.
- [10] S. W. Harunb, Pujiyantoa, Z. A. Ghanid, and H. Ahmad M. Yasin, "Performance Comparison between Plastic-Based Fiber Bundle and Multimode Fused Coupler as Probes in Displacement Sensors," *Laser Physics*, vol. 20, no. 10, pp. 1890-1893, Sep 2010.
- [11] V. O. Stern and M. Volmer, "The fading time of fluorescence," *Physikalische Zeitschrift*, vol. 20, pp. 183-188, 1919.

- [12] A. D. McNaught and A. Wilkinson, "Stern–Volmer kinetic relationships," in *IUPAC Compendium of Chemical Terminology*, 1997.
- [13] J. R. Lakowicz, "Quenching of Fluorescence," in *Principles of fluorescence spectroscopy*. New York, United States: Springer, 2006, ch. 8, pp. 277-330.
- [14] M. Nic, J. Jirat, B. Kosata, and A. Jenkins, "Inner Filter Effect," in *IUPAC Compendium of Chemical Terminology (the "Gold Book")*. Oxford, United Kingdom: Blackwell Scientific Publications, 2006, p. 2247.
- [15] B. C. MacDonalda, S. J. Lvinb, and H. Patterson, "Correction of fluorescence inner filter effects and the partitioning of pyrene to dissolved organic carbon," *Analytica Chimica Acta*, vol. 338, no. 1-2, pp. 155-162, Feb 1997.
- [16] I. E. Borissevitch, "More about the inner filter effect: corrections of Stern–Volmer fluorescence quenching constants are necessary at very low optical absorption of the quencher," *Journal of Luminescence*, vol. 81, no. 3, pp. 219-224, Apr 1999.
- [17] B. Fanget and O. Devos, "Correction of Inner Filter Effect in Mirror Coating Cells for Trace Level Fluorescence Measurements," *Anal. Chem.*, vol. 75, no. 11, pp. 2790–2795, Apr 2003.
- [18] P. Midoux, P. Wahl, J. C. Auchet, and M. Monsigny, "Fluorescence quenching of tryptophan by trifluoroacetamide," *Biochim Biophys Acta.*, vol. 801, no. 1, pp. 16-25, Sep 1984.

## Chapter 4

# **CHARACTERIZATION OF THE MULTI-CHANNEL FIBER OPTIC FLUORESCENCE DETECTION SYSTEM**

### **4.1 Introduction**

Characterization of the multi-channel fiber optic fluorescence detection system is discussed in this chapter. Measuring multiple analyte concentrations is essential for a wide range of environmental applications, which are important for the pursuit of public safety and health. Target analytes are often toxic chemical compounds found in groundwater or soil. However, in-situ measurement of such analytes still faces various challenges. Some of these challenges are rapid response for near-real time monitoring, simultaneous measurements of multiple analytes in a complex target environment, and high sensitivity to allow detection of low analyte concentration without sample pretreatment. A robust, rapid response, multiple analyte, in-situ measuring sensor system was developed. Experiments were designed with interest in investigating this system's performance with only the optodes thus providing reference figures of merit, such as

sensitivity and limit of detection, for further experiments or applications with the addition of various biosensors. Because a common type (pH or oxygen sensitive) optode, working in conjunction with numerous kinds of enzymes, can be used to detect many different corresponding chemical compounds. The unit under test in this chapter is the pH model prototype assembled by OptiEnz, Inc. In Section 4.2 of this chapter, the system configuration of the unit under test is given, including sensing mechanism concepts and system optical and electrical circuits. Section 4.3 describes the detailed protocols for optode fabrication. Section 4.4 talks about the experimental procedures. In Section 4.5, a series of experiments for the measuring sensitivity are presented with results and discussion. Section 4.6 covers experiments on channel-to-channel uniformity measurements. Finally, Section 4.7 compares the experimental results obtained with the unit under test in this work to results from other published work.

## 4.2 System Configuration

The system was designed based upon the fluorescent emission mechanism of a chemically sensitive dye used as the transducer. The emission intensity of the dye is related to the quencher concentration by the Stern-Volmer equation,

$$\frac{I_0}{I} = 1 + K_{SV}[Q], \quad 4-1$$

where  $I$  and  $I_0$  are the emission intensities with and without the presence of the quencher,  $[Q]$  is the quencher concentration, and  $K_{SV}$  is the Stern-Volmer quenching constant. Since  $I_0$  depends on excitation intensity and transducer properties, an absolute emission intensity value  $I$  is difficult to interpret alone or to quantitatively compare with other

results. As a result, all results of the Stern-Volmer ratio  $I_0/I$  in this work are obtained from the intensity ratio defined as

$$\frac{I_2}{I_1} = \frac{1 + K_{SV}[Q]_1}{1 + K_{SV}[Q]_2} \approx \frac{I_0}{I_1}, \text{ when } [Q]_2 \ll K_{SV}^{-1} \quad 4-2$$

where  $I_1$  and  $I_2$  are respectively the emission intensities with the presence of the quencher at the concentrations of  $[Q]_1$  and  $[Q]_2$ . In some systems, such as a system with quencher being  $H^+$ , it is not realistic to measure the unquenched intensity  $I_0$  in an aqueous environment with the quencher  $H^+$  concentration being zero. As a result,  $I_2$  is approximated to be the unquenched intensity  $I_0$  when  $[Q]_2$  is very small, in other words,  $I_2/I_1$  is approximately equal to the Stern-Volmer ratio  $I_0/I$ . Optodes and optoelectronics hardware of the system were built based on this detection mechanism.

Motivated by the need to simultaneously sense multiple analytes with a multiplex biosensor array, several architectures for a multi-channel system were considered. First, the most straightforward approach is the simple duplication of the full system for each sensor, but this method is bulky and expensive. Since a common kind of transducer and optode structure can be used with different enzymes to detect various target analytes, the source, detector, filter, and fiber systems for each biosensor can be identical. As a result, a second approach of optical multiplexing has been implemented by others [2] and offers the lowest component count but relies on expensive custom mechanical switches for plastic optical fibers. A third approach adopted in this work applies electronic multiplexing [3]. Each optode is excited by its own optical source, and sources are sequentially driven one at a time by cycling through all channels with multiplexing circuitry. All channels share a single photomultiplier tube (PMT) as the detector to

reduce cost and variations from the hardware without sacrificing the sensitivity of the detector. Also, time division multiplexing reduces interference between channels.

The eight channel system hardware is comprised of a single PMT, two filters, eight blue LEDs, fiber optic and electronic circuitry. The block diagram of the system is shown in Figure 4.1. In the forward signal path, a microcontroller (PAX32A-Q44, Parallax Inc) is programmed to sequentially turn on the LED (IF E92B 470nm, Industrial Fiber Optics) of each channel, which launches excitation light through a plastic optical fiber (SH4001-1.3, 980 $\mu$ m core diameter, Industrial Fiber Optics), an excitation bandpass filter (HQ450/60m, Chroma Technologies), and a 2 $\times$ 2 fiber optic splitter (IF-540 custom order, Industrial Fiber Optics). While the fiber splitter is primarily used to divert a portion of the return signal, as a consequence, it also divides the excitation light into two forward paths, one of which is sent to a light absorber fixture while the other goes to the optodes. The excitation filter blocks LED light at wavelengths above 480 nm that are too close to the peak of the emission spectrum of FLA. In the return signal path, the emitted fluorescent light from the optode passes through the optical fiber splitter, an emission dichroic filter (D530/20x, Chroma Technologies), and eventually to the photocathode of a PMT (H5784-02, Hamamatsu). The emission filter blocks reflected excitation light at wavelengths shorter than 520 nm. Both the excitation and emission filters were incorporated to greatly reduce light from the LEDs reaching the PMT. The emitted fluorescence optical power is measured by the PMT and processed by a de-multiplexing data acquisition circuit, which consists of an A/D converter (AD7707BR, Analog Devices Inc.) and the same microcontroller that drives the LEDs. Finally the

fluorescence optical powers of all channels are reported and recorded as scaled digital signals at the user interface. The electronic circuitry of the unit is shown in Figure 4.2.

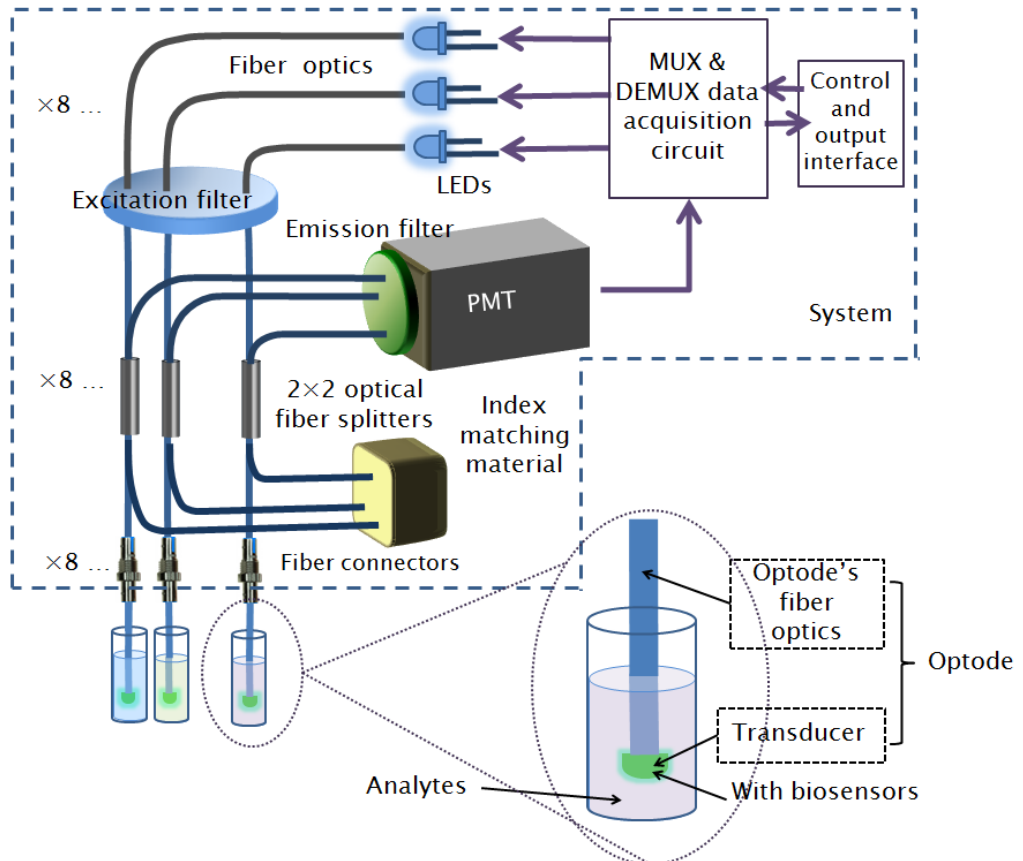


Figure 4.1. Block diagram of the multi-channel fiber optic fluorescence sensing system configuration.

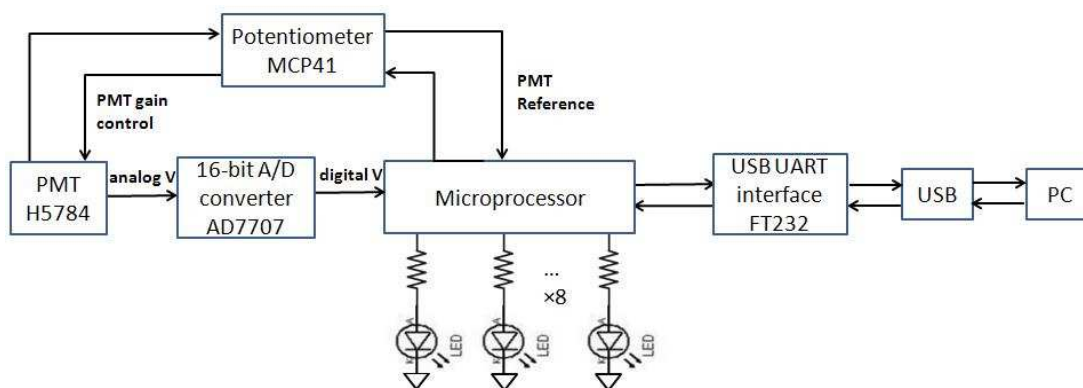


Figure 4.2. A block diagram of the electronic multiplexing/demultiplexing circuitry.

### 4.3 Optodes Fabrication

Optodes were designed to provide a platform for the biosensors to interact with analytes as well as to interpret the reaction information. An optode is comprised of a fiber optic and immobilized fluorophore molecules. Plastic fiber optics were preferred over glass fiber optics in an optode because the large 5% refractive index step between the core and cladding increases the numerical aperture to 0.5, which allows a wider light acceptance cone for improved collection of the fluorescent emission. Each optode's fiber optic was created from a 25 cm long ST connectorized PMMA fiber optic cable (SH4001-1.3 980 $\mu$ m core diameter custom order, Industrial Fiber Optics) terminated with the bare fiber end exposed. The bare end was polished with a 2000 grit 3  $\mu$ m polishing film (IF-TK4-RP2, Industrial Fiber Optics) to increase fluorescent light coupling efficiency.

PH sensitive fluoresceinamine (FLA) transducers (without the biosensor) are fabricated using cross-linked poly (vinyl alcohol) (PVOH) to realize the immobilization

of the fluorophore, FLA, onto a fiber-optic using the method published in Reference [4]. Transducer fabrication was done by CSU student Jacob Adam during 2009 – 2011 academic years using following protocols. PVOH gel is formed by combining 0.50 mL of PVOH solution with 0.050 mL each of 2% glutaraldehyde in water and 4.0 M HCL. Then to immobilize FLA is using the following steps. Cyanuric chloride (0.5 g) was dissolved in 20.0 mL of acetone, and 1.0 g of PVOH and 10.0 mL of water were added. The mixture was stirred and allowed to react for 20 min at room temperature. PVOH is insoluble in this medium and can be separated by filtration. After the PVOH-cyanuric chloride conjugate was washed with 50 mL of 1/1 acetone-water, the conjugate was reacted with a 10.0 mL solution containing 100mg fluoresceinamine in acetone. After 30 min at room temperature the product was separated and washed, first with acetone and then with water until no further unreacted indicator can be observed in the washings. This material was then dried and stored as a solid. The procedure can be repeated as necessary to increase the amount of immobilized indicator per gram of PVOH. Because the cross-linking process may vary each fabrication batch, the fluorophore concentration in each batch differs.

#### **4.4 Measurements Protocols**

The system detection figures of merit, such as sensitivity and system resolution, which is the smallest detectable change in the analyte concentration, were investigated using FLA optodes. Three replicates of pH sensitive FLA optodes were fabricated using the procedures described in Section 4.3 of this chapter. Optodes were tested in varying pH buffer solutions ranging from 3.05 to 8.69. Based on calculation, buffer solutions with different pH values were made with the following procedures. Buffers with pH

from 3.0 to 4.25 were prepared with 1M HCL and 1M acetic acid; buffers with pH from 4.5 to 5.5 were prepared with 1M sodium acetate and 1M acetic acid; buffers with pH from 5.75 to 6.25 were prepared with 1M bis-tris and 1M HCL; buffers with pH from 6.5 to 8.0 were prepared with 1M potassium dihydrogen phosphate ( $\times 7H_2O$ ) and 1M disodium hydrogen phosphate; buffers with pH from 8.5 to 8.75 were prepared with 1M bicine and 1M NaOH. The pH values of all buffer solutions were confirmed with a pH meter (Accumet AB15, Fisher Scientific). A detailed pH buffer solution recipe is attached in the Appendix A of this thesis.

The Stern-Volmer ratio was calculated from the fluorescence emission intensity readings. All fluorescence intensities  $I$  were obtained from the following equation,

$$I = R - R_b \quad 4-3$$

where  $R$  is the intensity reading of the optode in a pH buffer solution, and  $R_b$  is the background correction intensity reading when the channel is not connected to an optode and the end connector is capped to eliminate room light coupling.  $R_b$  reading values are typically 5% of  $R$  values.  $I_1$  in Eqn. 4-2 was the fluorescence intensity  $I$  measured in the varying pH buffer solutions, and  $I_2$  in Eqn. 4-2 was approximated to  $I_0$  with the fluorescence intensity  $I$  in the lowest  $H^+$  concentration solution. Therefore, the Stern-Volmer ratio  $I_0/I$  was approximated with  $I_2/I_1$ , as derived in Eqn.4-2. The unquenched intensity  $I_0$  was obtained in the pH buffer solution with  $H^+$  concentration of 1.78 nM (pH=8.69).

## 4.5 Sensitivity Measurement Results

To extract figures of merit of the system, such as the sensitivity, results of the fluorescent intensities over various concentrations of analyte are presented as the Stern-Volmer ratio of the fluorescent intensities as a function of the quencher concentrations. Over the entire measurement range of  $H^+$  concentration of 0.002 – 891  $\mu\text{M}$  (pH of 3.05 – 8.69), the fluorescent intensities behave differently from what is described in the Stern-Volmer equation, as shown in Figure 4.3. Measurements were repeated using nominally identical FLA optodes. In the plot, each data point is averaged from 200 rapid measurements with sampling rate at about 10 Hz, and the relative standard deviation between measurements for all conditions is less than 0.3%.

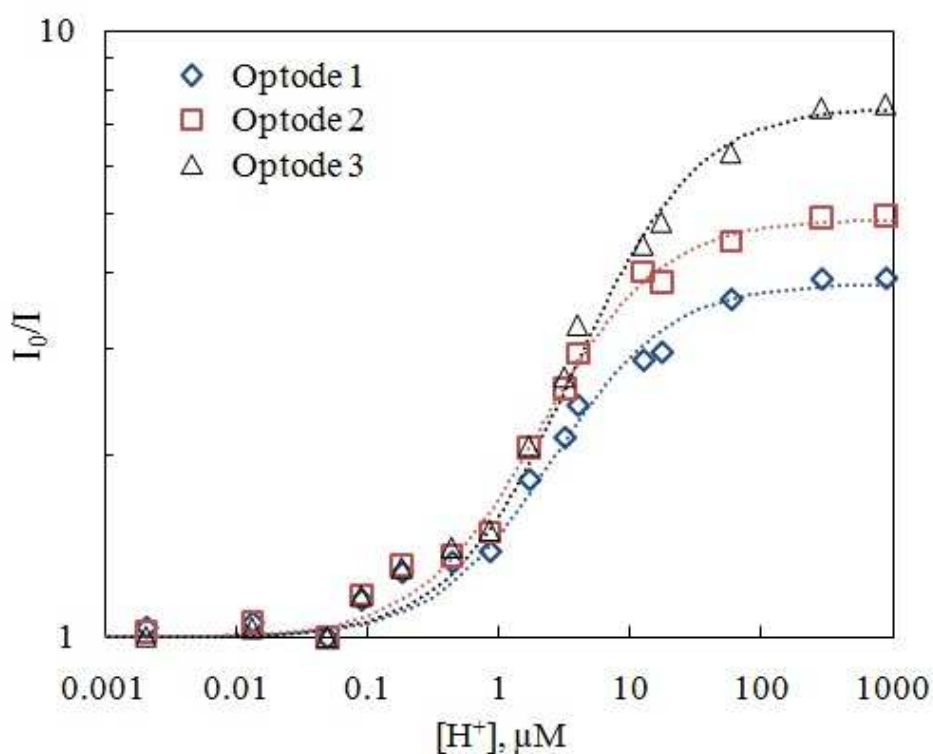


Figure 4.3. The Stern-Volmer ratio vs. varying  $H^+$  concentrations shown on a log-log scale.

The non-linearity observed from the Stern-Volmer plots is a departure from the ideal case and has been observed [5] and verified to be the result of two causes. First, the non-linearity is attributed to the fractional inaccessibility of the fluorophores in previous publications [6], and it is described as

$$\frac{I_0'}{I'} = \frac{\frac{1}{f}}{\frac{1}{1 + K_{SV} \cdot [Q]} + \frac{1}{f} - 1}, \quad 4-4$$

where  $I_0'$  and  $I'$  are the measured unquenched and quenched fluorescent intensities that are affected by the fractional accessibility,  $f$ , of the fluorophore. Second, the non-linearity of the Stern-Volmer plots can be ascribed to the back reflection [7] of the fiber couplers. The back reflection is defined as when the excitation light from the LED gets coupled into the fiber optic and transmits to the end of the fiber, an interface with different refractive indices on two sides, a portion of the excitation light gets transmitted through the interface while the other portion of the excitation light is reflected and coupled back. Although the back reflected excitation light reading from the PMT is significantly decreased in intensity by the emission filter, shown in Figure 4.1, due to the imperfection of the optical filters, a considerable amount of back reflection intensity can pass the filter and still be comparable to the fluorescent intensity, and thus becomes problematic to the measurements. The impact of the back reflection on the Stern-Volmer equation can be described as

$$\frac{I_0'}{I'} = \frac{I_{BR}/I_0 + 1}{\frac{1}{1 + K_{SV} \cdot [Q]} + I_{BR}/I_0}, \quad 4-5$$

where  $I'_0$  and  $I'$  are the measured fluorescent intensities that contain the back reflection intensity,  $I_{BR}$ , and  $I_0$  is the ideal unquenched fluorescent intensity. Ideally, as the Stern-Volmer equation described, the ratio of  $I_0/I$  is a linear function with the quencher concentration; however, due to the back reflection the measured ratio,  $I'_0/I'$ , is not a linear function of the quencher concentration. Considering both impacts of the fractional inaccessibility of the fluorophore and the back reflection, the modified Stern-Volmer model can be described as

$$\frac{I'_0}{I'} = \frac{\frac{1}{f} \cdot (I_{BR}/I_0 + 1)}{\frac{1}{1 + K_{SV} \cdot [Q]} + \frac{1}{f} \cdot (I_{BR}/I_0 + 1) - 1}, \quad 4-6$$

where  $I'_0$  and  $I'$  are the measured fluorescent intensities that are affected by the fractional inaccessibility of the fluorophore and the back reflection. Eqn. 4-6 contains both factors, therefore, when no fractional inaccessibility occurring,  $f = 1$ , Eqn. 4-6 is the same as Eqn. 4-5; when there is no back reflection,  $I_{BR} = 0$ , Eqn. 4-6 becomes identical to Eqn. 4-4; when neither of the non-ideal cases occur, Eqn. 4-6 equals to the ideal Stern-Volmer equation, Eqn. 4-1.

To analyze the experimental data in Figure 4.3, the non-idea model of the Stern-Volmer equation model is applied. Since the measurements were performed on the same channels for all three optodes, the back reflection intensities,  $I_{BR}$ , are assumed to be identical for all measurements. Eqn. 4-4 is utilized to fit the experimental data, as shown in dotted lines in Figure 4.3 with  $R^2$  of 0.986, 0.994, and 0.993 respectively. Fitting parameters of the quenching constant,  $K_{SV}$ , and the accessibility fraction,  $f$ , were extracted from Eqn. 4-4, as shown in Figure 4.4. Three optodes have an average  $K_{SV}$

value of  $8.66 \times 10^5 \text{ M}^{-1}$ , and an average  $1/f$  value of 1.25 ( $f = 79.7\%$ ). The error bars in Fig. 2 (b) show bounds within which fitting parameters satisfy that the mean squared error (MSE) between the model and the measurements is less than or equal to twice the minimum MSE. Concluded from Figure 4.4, the fractional inaccessibility model, Eqn. 4-4, is strongly dependent on  $f$  with error bounds tightly confined around the minimum MSE point, and on the other hand, the model is not sensitive to the varying of quenching constant,  $K_{SV}$ , because the the  $K_{SV}$  values of all optodes only vary within the bounds. LOD is defined as the analyte concentration corresponding to the mean of the sum of the blank measurement and 3 times (for a 99.7% confidence interval) the standard deviation of the blank measurement [8]. Since a solution without any  $\text{H}^+$  does not exist, a blank measurement is assumed to be at  $\text{H}^+$  concentration of 1.78 nM (pH=8.69). The LOD for all three optodes are 2.1, 0.75, and 1.3 nM of  $\text{H}^+$ .

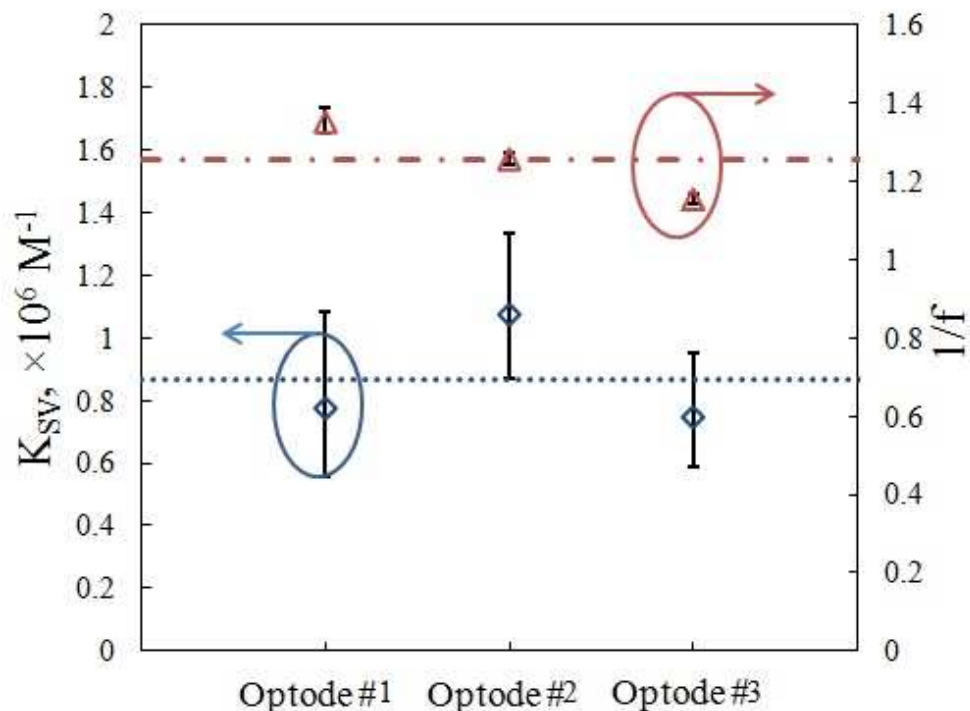


Figure 4.4. Calculated quenching constant,  $K_{SV}$  (left y-axis), and calculated the inverse of the fluorophore accessibility fraction,  $f$ , (right y-axis) three optodes are plotted. Error bars show bounds within which fitting parameters satisfy that MSE is less than or equal to twice the minimum MSE. The dotted line shows the value of  $K_{SV}$  and  $f$  averaged for all optodes.

When the experimental results are fit with a regression line, which models the ideal behavior, the  $R^2$  value as the coefficient of the determination does not fully reflect how closely the model fits the experimental results. As a result, model accuracy (MA) is introduced here as the measure of how accurately the model allows determination of the arbitrary analyte concentrations with a calibrated optode. Lower limit of detection (LLD), as previously defined by Anderson [9], differs from MA in that the LLD only applies to linear regression lines. To generalize MA for different types of regression lines, first, the error between the model and the measurement is first defined as

$$\epsilon_{model} = \sqrt{\frac{\sum_i^N \left[ \left( \frac{I_0}{I_i} \right)_{measured} - \left( \frac{I_0}{I_i} \right)_{model} \right]^2}{N - n_f}} \quad 4-7$$

where N is the number of measurements data points,  $n_f$  is the number of fitting parameters in the model,  $\left( \frac{I_0}{I_i} \right)_{measured}$  is the measured Stern-Volmer ratio, and  $\left( \frac{I_0}{I_i} \right)_{model}$  is the corresponding Stern-Volmer ratio from the model at the same analyte concentration. In the case of this work,  $n_f$  is 2 using Eqn. 4-7. Then, MA is defined as 3 times the error,  $\epsilon_{model}$ , divided by the sensitivity. MA calculated from the existing three optodes is 0.49, 0.32, and 0.80  $\mu\text{M}$ .

#### 4.6 Channel-to-Channel Uniformity Measurements

Fluorescence intensity of a single optode was measured on each channel of the multi-channel fiber optic fluorescence detection system to determine the channel-to-channel uniformity. The Stern-Volmer ratio dependence on low  $\text{H}^+$  concentrations over 0.025 – 3.55  $\mu\text{M}$  (pH 5.45 – 7.6) is shown in Figure 4.5 for the eight channels. The channel-to-

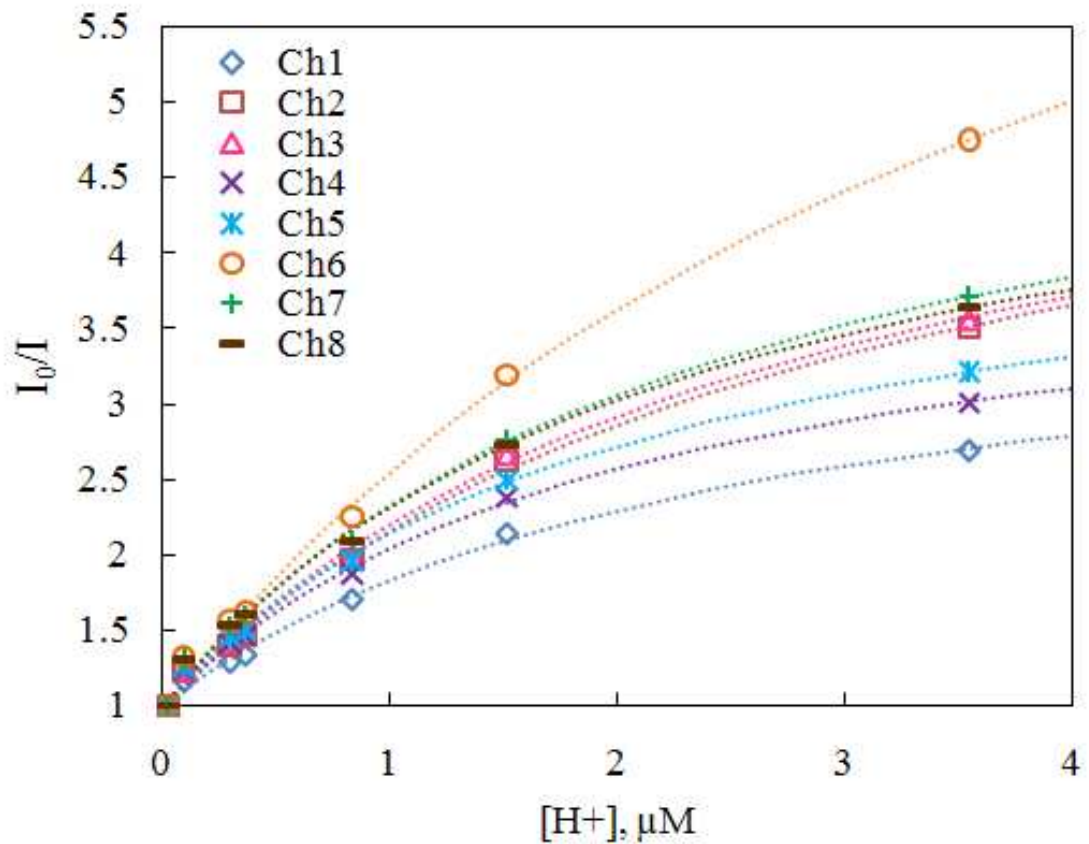


Figure 4.5. The fluorescent intensity (indicated with various shaped data points) for varying  $H^+$  concentrations measured with a single optode on all channels as an indication of channel-to-channel uniformity. The data is fit with the modified Stern-Volmer model that includes the back reflection effects (dotted lines).

channel variation in the excitation source power and the coupling efficiency of the fiber optics are eliminated by calculating the Stern-Volmer ratio,  $I_2/I_1$ . Since all channels were measured with the same optode, the fractional accessibility,  $f$ , of all channels are the same, the back reflection model in Eqn. 4-6 is adopted here. The cause of the channel-to-channel variation in is the slightly unequal back reflection intensities [7] of the fiber couplers used in all channels. The modified Stern-Volmer model in Eqn. 4-5 fits the experimental results very well with the  $R_2$  value averaged at 0.996. The quenching constants,  $K_{SV}$ , of all channels are shown in Figure 4.6, and is averaged at  $2.05 \times 10^6 M^{-1}$ .

The error bars in the graph show bounds within which the MSE between the model and the measurements is less than or equal to twice the minimum MSE. Similar to the results for a single channel, the model is not strongly sensitive to the varying of quenching constant,  $K_{SV}$ , and  $K_{SV}$  of all channels are varying roughly within the error bounds. Figure 4.6 also shows the calculated back reflection intensity as a fraction of the unquenched fluorescent intensity,  $I_{BR}/I_0$ , for all channels with error bars showing bounds within which MSE is less than or equal to twice the minimum MSE. The average value of  $I_{BR}/I_0$  of all channels is 24.3%.

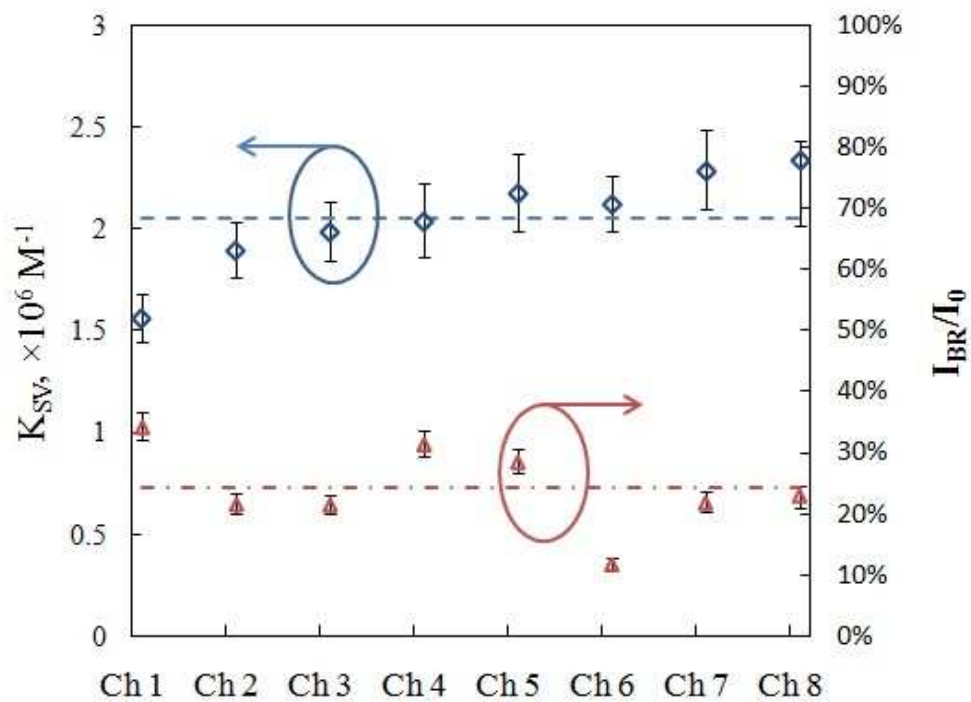


Figure 4.6. Calculated quenching constant,  $K_{SV}$  (left y-axis), and calculated back reflection intensity as a fraction of the unquenched fluorescent intensity,  $I_{BR}/I_0$ , (right y-axis) for all channels are plotted. Error bars show bounds within which the MSE between the model and the measurements is less than or equal to twice the minimum MSE. The dotted line shows the value of  $K_{SV}$  and  $I_{BR}/I_0$  averaged for all channels.

## 4.7 Discussion

While numerous fiber optic photoluminescence detection biosensor systems have been reported, Hols et al. [7] have demonstrated a fiber optic photoluminescence system with the ability to simultaneously detect multiple analytes. In that research, the system uses a phase-angle detection mechanism with oxygen as the quencher but did not provide quantized system detection figures of merit to compare with this work.

Although the system in this work was not intended for pH sensing, pH sensing ability is a critical parameter for understanding the enzymatic biosensor system performance. To understand the relative performance of the system presented here, results of other fiber-optic systems using immobilized pH sensors as probes [10] have been compared with the system presented here. The normalized fluorescence intensity with varying pH values is shown in Figure 4.7 with three nominally identical optodes. For comparison purpose, calculation of the sensitivity and the minimum detectable change is carried out using the method described by Nivens et al. [11]. The method is to determine  $pK_a$  as the midpoint of the linear portion of the calibration curve, and the minimum detectable change in pH is determined by twice the standard deviation of the intensities at the  $pK_a$ . The highest pH sensitivity of this work is 0.35 per pH unit ( $R^2 = 0.96$ ) at pH values between 4.5 and 7.5, and the minimum detectable change in pH is 0.0089 pH units ( $pK_a = 5.90$ ). The system demonstrated by Nivens et al., as shown in Figure 4.8, has a sensitivity of approximately 0.10 per pH unit for the APTES sensor and 0.08 per pH unit for the GPTMS/APTES sensor, and the minimum detectable change of 0.17 pH units for the APTES sensor and 0.13 pH units for the GPTMS/APTES sensor.

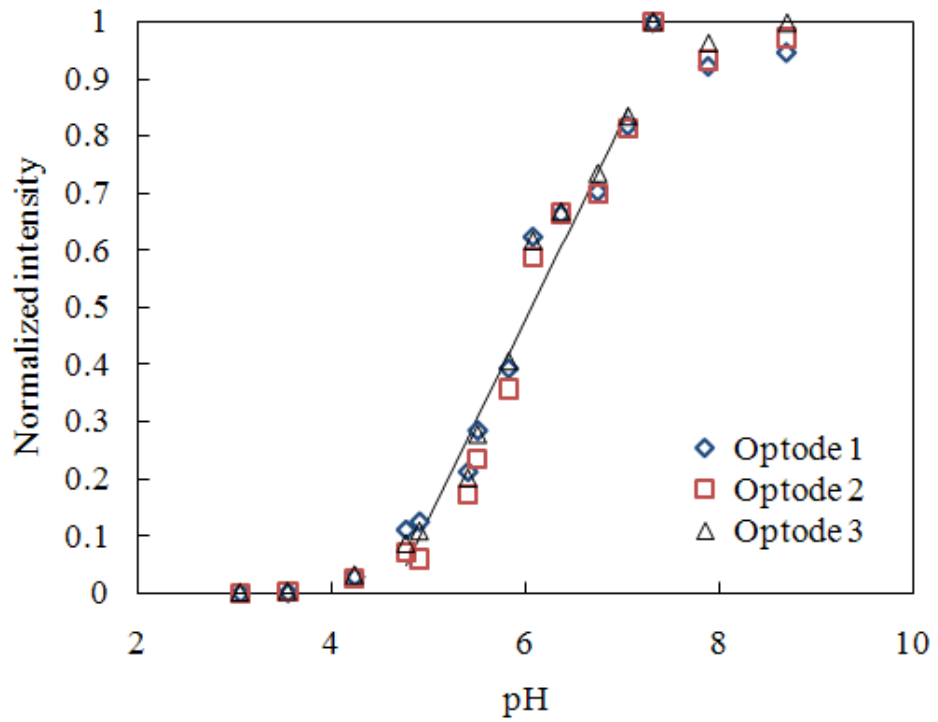


Figure 4.7. The normalized fluorescence intensity with varying pH values of three replicates of FLA optodes.

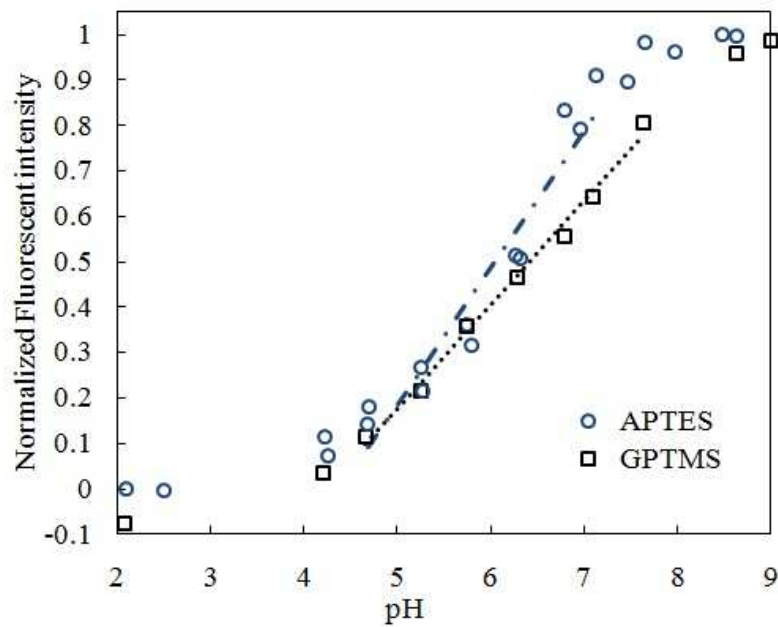


Figure 4.8. The relative fluorescence intensity calibration curves of Nivens' system with APTES and GPTMS/APTES formulation as the sensors. Reproduced from Reference [11].

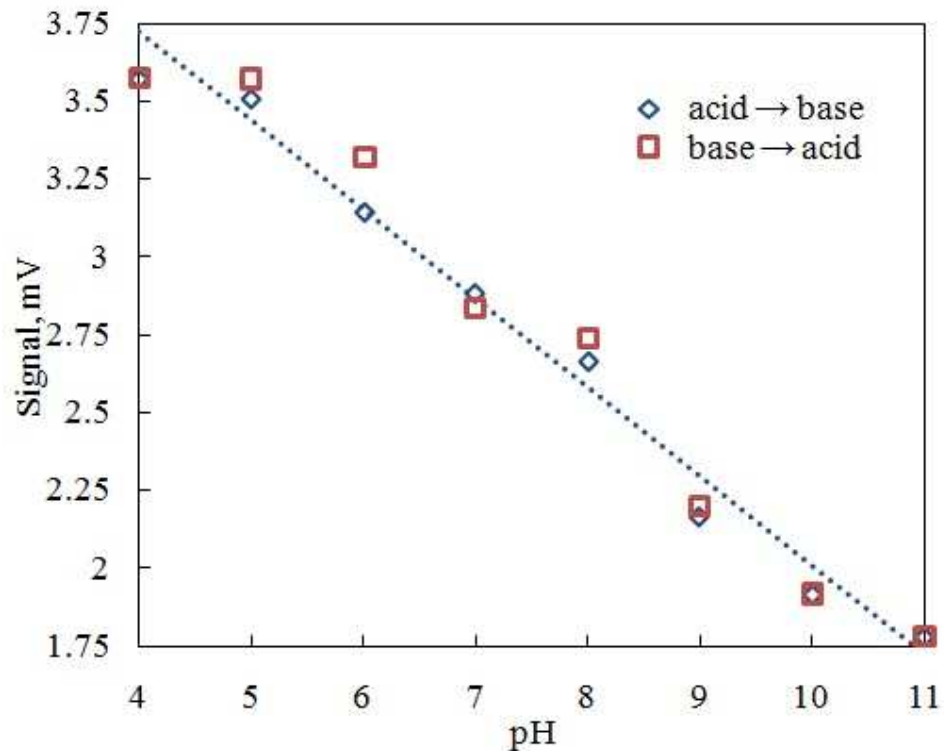


Figure 4.9. The full titration curve of Ben-David's system with the dynamic range claimed from pH 4 to 11. Reproduced from Reference [12].

Moreover, to determine how accurately the interpolation formula fits the measurement results, MA is calculated to compare the system performance between this work and other published work. MA of the system in this work is 0.52 pH units while the MA of the system demonstrated by Nivens et al. are 0.72 pH and 0.26 pH units for the APTES and GPTMS/APTES sensors, calculated within the same linear pH range (pH 4.5 – 7.5). Compared using either the method given by Nivens et al. or the method defined in this work, the multi-channel fiber optic fluorescence system has better figures of merit in sensitivity and MA. The pH dynamic range of this work is approximately from pH 3 to 9. Nivens et al. have demonstrated the dynamic range of the system from pH of 3 to 9. Ben-David et al. have demonstrated a system with dynamic range from pH 4 to 11, as

shown in Figure 4.9, and about 0.2 pH unit accuracy [12]. Using the digitized plot from the publication to calculate the sensitivity and the detection limit defined in this work, the system described by Ben-David et al. has a MA of 1.2 pH unit; the sensitivity is 0.29 per pH unit ( $R^2 = 0.97$ ). A summarized comparison of figures of merit between this work and the two systems demonstrated by Nivens and Ben-David is shown in Table 4.1.

Table 4.1 A Comparison of Figures of Merit Between This Work and Other Cited Works

System	Sensors	Sensitivity, per pH unit	Minimum detectable change (method from cited works), pH units	MA (method from this work), pH units
Cited work by Nivens et al.	APTES	0.10	0.17	0.72
	GPTMS/APTES	0.08	0.13	0.26
Cited work by Ben-David et al.	Not specified	0.29	~0.01	1.2
This work	FLA	0.35	0.0089	0.51

The multi-channel fiber optic fluorescence detection system is compatible with various enzymes as the biocomponent in the biosensor for many different types of analytes, such as 1,2-dichloroethane (DCA) and ethylene dibromide (EDB). For DCA in aqueous solution measurement described in an earlier report [13], the biocomponent is haloalkane dehalogenase, Dh1A (E.C.3.8.1.5) [14] in whole cells of the soil bacterium, *Xanthobacter autotrophicus* GJ10 [15]. For 1,2-dibromoethane, also known as EDB, in water measurement [5], the biocomponent is the hydrolytic haloalkane dehalogenase

DhaA in whole cells of *R. sp. GJ70*. In the enzyme catalyzed reactions, 1 M of H<sup>+</sup> production consumes 1 M DCA or 1 M EDB in the adjacent environment of the respective enzymatic biosensor. Assuming complete reactions occurring in a finite volume, the factor of diffusion is neglected in this analysis. LOD is calculated for both DCA and EDB. Since a blank measurement, being the fluorescent intensity in absence of the analyte, is dependent on the acidity of the starting solution; therefore, LOD of the analyte, is also dependent on the starting pH of the solution in the absence of the analyte, as shown in Figure 4.10. The minimum LOD is 0.08 µg/L for DCA and 0.14 µg/L for EDB. In preliminary reports, experimental results with similar prototype instrumentation was reported to have LOD of 1 µg/L for EDB [5], and 11 mg/L for DCA [13]. The US Environmental Protection Agency (EPA) restricts the maximum contaminant level (MCL) to be 5 µg/L of DCA and 0.05 µg/L of EDB in the drinking water standards [16]. Therefore, system measurement resolution of the multi-channel fiber optic fluorescence system readily meets the requirements for DCA measurements but is not sufficient in EDB measurements. Future work of improving the sensitivity and system resolution is desired for EDB measurements.

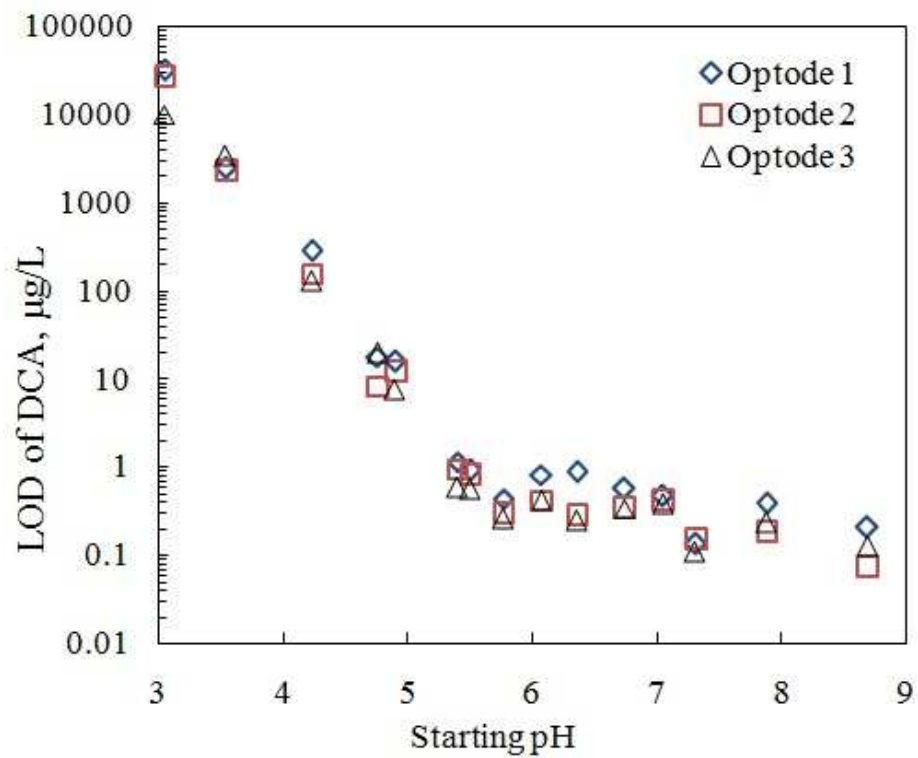


Figure 4.10. Analytical LOD of DCA and EDB as the analyte dependent on the acidity of the aqueous environment without the presence of the analyte.

## 4.8 References

- [1] V. O. Stern and M. Volmer, "The fading time of fluorescence," *Physikalische Zeitschrift*, vol. 20, pp. 183-188, 1919.
- [2] H. Hecht and M. Kölling, "A low-cost optode-array measuring system based on 1 mm plastic optical fibers — new technique for in situ detection and quantification of pyrite weathering processes," *Sensors and Actuators B: Chemical*, vol. 81, no. 1, pp. 76-82, Dec. 2001.
- [3] K. F. Reardon, Z. Zhong, and K. L. Lear, "Environmental applications of photoluminescence-based biosensors," in *Advances in Biochemical Engineering/Biotechnology*, T. Scheper, Ed.: Springer, 2010, ch. 116, pp. 99-123.
- [4] Z. Zhujun et al., "Poly(vinyl alcohol) as a Substrate for Indicator Immobilization for Fiber-Optic Chemical Sensors," *Anal. Chem.*, vol. 61, no. 3, pp. 202-205, Feb 1989.
- [5] K. F. Reardon, D. W. Campbell, and C. Müller, "Optical fiber enzymatic biosensor for reagentless measurement of ethylene dibromide," *Eng. Life Sci.*, vol. 9, no. 4, pp. 291–297, Aug 2009.
- [6] J. R. Lakowicz, "Quenching of Fluorescence," in *Principles of fluorescence spectroscopy*. New York, United States: Springer, 2006, ch. 8, pp. 277-330.
- [7] Z. J. Yi, K. F. Reardon, and K. L. Lear, "A Comparison between Multimode Fused Fiber Coupler and Bifurcated Fiber Assembly in Photoluminescence (PL)-based Biosensor Systems".
- [8] M. Nic, J. Jirat, and B. Kosata, "limit of detection (in analysis)," in *IUPAC. Compendium of Chemical Terminology (the "Gold Book")*. Oxford, United Kingdom: Blackwell Scientific Publications, 1997.
- [9] D. J. Anderson, "Determination of the Lower Limit of Detection," *Clinical Chemistry*, vol. 35, no. 10, pp. 2152-2153, Mar 1989.
- [10] Otto S Wolfeis, "Fiber-Optic Chemical Sensors and Biosensors," *Analytical Chemistry*, vol. 72, no. 12, 2000.
- [11] D. A. Nivens, Y. Zhang, and S. M. Angel, "A Fiber-Optic pH Sensor Prepared Using a Base-Catalyzed Organo-Silica Sol-Gel," *Analytica Chimica Acta*, vol. 376, no. 2, pp. 235-245, Dec 1998.

- [12] O. Ben-David, E. Shafir, I. Gilath, Y. Prior, and D. Avnir, "Simple Absorption Optical Fiber pH Sensor Based on Doped Sol-Gel Cladding Material," *Chem. Mater.*, vol. 9, no. 11, pp. 2255–2257, Nov 1997.
- [13] D. W. Campbell, C. Müller, and K. F. Reardon, "Development of a fiber optic enzymatic biosensor for 1,2-dichloroethane," *Biotechnol Lett*, vol. 28, no. 12, pp. 883–887, May 2006.
- [14] J. Kmuníček et al., "Comparative binding energy analysis of the substrate specificity of haloalkane dehalogenase from *Xanthobacter autotrophicus* GJ10," *Biochemistry*, vol. 40, no. 30, pp. 8905-8917, Jul 2001.
- [15] D. B. Janssen, A. Scheper, L. Dijkhuizen, and B. Witholt, "Degradation of halogenated aliphatic compounds by *Xanthobacter autotrophicus* GJ10," *Appl Environ Microbiol.*, vol. 19, no. 3, pp. 673–677, Mar 1985.
- [16] Environmental Protection Agency (EPA). (2009, May) National Primary Drinking Water Regulations. [Online]. HYPERLINK  
"http://water.epa.gov/drink/contaminants/index.cfm"  
<http://water.epa.gov/drink/contaminants/index.cfm>
- [17] G. Hols, R. N. Glud, M. Köhl, and I. Kilmant, "A micro-optode array for fine-scale measurement of oxygen distribution," *Sensors and Actuators B*, vol. 38, no. 1-3, pp. 122-129, Feb 1997.

## Chapter 5

# **A COMPARISON BETWEEN MULTIMODE FUSED FIBER COUPLER AND BIFURCATED FIBER ASSEMBLY IN PHOTOLUMINESCENCE (PL) - BASED BIOSENSOR SYSTEMS**

### **5.1 Introduction**

The performances of fused fiber couplers and bifurcated fiber assemblies were investigated for application to photoluminescence (PL)-based biosensor systems. Complex tradeoffs among back reflection noise, coupling efficiency and split ratio were analyzed with theoretical and experimental data. A series of experiments and simulations were carried out to compare the two types of fiber assemblies in PL-based biosensor systems in terms of excess loss, split ratio, back reflection, and coupling efficiency. In Section 5.25.2 of this chapter explains the motivation of this analysis. In Section 5.3 provides the experimental set-up including hardware configurations and component details. Section 5.4 presents the results of the experiments with excess loss and split ratio for the two types of fiber assemblies. In Section 5.5, measurements were performed to analyze the back reflection impact on the two types of fiber assemblies. Experimental

results as well as the expected calculation results are presented. Section 5.6 compares the coupling efficiency of the bifurcated fiber assembly and the fused fiber coupler.

Calculation methods and simulation results of the coupling efficiency are presented for the analysis.

## **5.2 Motivation**

Photoluminescence (PL)-based biosensor systems cover a broad field of applications, such as environmental chemicals measurements and monitoring, medical diagnosis and industrial process quality control. The systems require the biosensor transducer end to connect with both an excitation source and an optical detector, as a result, an optical pathway splitting mechanism is required [1]. Free-space splitting, often using dichroic mirrors, has been implemented in research work [2] [3]. However such a method involves precise alignment and is sensitive to vibration, which limits the system in field applications. Optical switches have also been designed [4], but the cost, bulkiness and the sensitivity to shocks are some of the associated disadvantages. A fiber optic splitter assembly is a good solution to the optical pathway splitting problem.

Two of the most common fiber optic splitter assemblies are fused fiber couplers and bifurcated fiber assemblies, and choosing between the two is not a simple matter of the maximum output coupling, but rather complex tradeoffs should be taken to the consideration. The first issue is back reflection. Back reflection is the excitation light reflected to the detector due to Fresnel reflection at the transducer end. The back reflection causes an error when the detector treats it as a part of the signal, which should only include the emission intensity of the PL transducer. Adding optical filters reduces

the effect of back reflection, but does not completely remove it. In low PL signal situations, the back reflection intensity, even after filtering, can be the same order of magnitude as the signal. This problem becomes more severe when part of the absorption spectrum of the PL transducer overlaps its emission spectrum. For instance, fluoresceinamine (FLA) has its absorption peak at 470nm and emission peak at 520nm [5], and the small Stoke's shift makes it difficult to effectively block the excitation light while passing the PL emission. Photodetectors that have no spectroscopic ability, such as photodiodes and photomultiplier tube (PMT), are unable to distinguish the back reflection interference from the PL signals. PL intensities are often normalized with a reference PL intensity to compensate the variations in the excitation light [6] [7], however, the back reflection cannot be eliminated by normalization. The second factor is the coupling efficiency. To obtain the maximum coupling efficiency requires balancing the tradeoff between the excitation light coupling from source to the transducer and the PL emission light coupling from the transducer to the detector. The third considered aspect is the split ratio. Due to the nature of manufacturing process, the split ratio of fused fiber couplers may not be uniform from unit to unit. Simulations and experiments are carried out in this work to analyze the tradeoffs in back reflection, coupling efficiency and splitting ratio.

In previous works, Yasin et al. have compared the fused fiber coupler and bundled fiber as probes in displacement sensors in terms of the system sensitivity, linear range, resolution etc. [8]. Yuan etc. have compared the absorbance stability and transmittance of three 1×3 assemblies in chemical sensor applications: a 400 μm fused glass fiber-optic coupler, a 1000 μm fused, plastic fiber-optic coupler, and a 1000 μm glass fiber-optic bundle [9]. Myrick etc. have investigated several fiber configurations for PL

measurements and Raman scattering; however, the study never compared the two kinds of fiber assemblies in that work [10]. The coupling efficiency of a multimode fused coupler has been theoretically studied by Li et al., but no comparison with other configurations was made [11].

### **5.3 Experimental Set-up**

To evaluate the performance of the two types of fiber assemblies, back reflection, split ratio and excess loss measurements were performed. The block diagram of the back reflection experimental set up is shown in Figure 5.1. A very fundamental difference between the structures of the bifurcated fiber assemblies and the fused fiber couplers is that the fused fiber couplers have multiple fiber optics fused together in a common region and branch out into separate ports at both ends of the fiber optics, while the bifurcated cable assemblies have one end of multiple fiber optics bundled up together. Figure 5.2 shows an example of a bifurcated fiber assembly [12] as an illustration. The back reflection measurements were performed on both kinds of fiber assemblies, but only the back reflection intensity of the fused fiber coupler can adjust using the index matching method. Three different index matching materials were applied: air ( $n=1.00$ ), water ( $n=1.33$ ), and silicone gel ( $n=1.40$ ). An LED (IF E92B, Industrial Fiber Optics) that peaks at 470nm along with a source filter (HQ450/60m, Chroma Technologies) were used as the excitation source. A  $2\times 2$  3dB fused coupler assembly (IF-540 custom order, each core diameter 980 $\mu\text{m}$ , Industrial Fiber Optics) and a  $1\times 2$  3dB bifurcated coupler assembly (BIF600-UV-VIS, each core diameter 600  $\mu\text{m}$ , Ocean Optics, Inc.) were studied. For the optode, both experiments use a 980 $\mu\text{m}$  core ST-connectorized plastic

optical fiber (POF, GH4001 custom order, Industrial Fiber Optics). The connectorized end of the optode was connected a ST-ST mating sleeve (Industrial Fiber Optics) and the distal end was covered with the transducer mixture, which is 1 mg of Ru(dpp)<sub>3</sub> dissolved in 1 mL chloroform and then blended into 200 mg silicone gel (clear RTV silicone, Permatex Inc.). When different index matching materials were applied, the spectra were recorded with a spectrometer (USB4000-FL, Ocean Optics Inc.). In the excess loss and the split ratio measurements, the launched input port optical power was determined using a single fiber (POF, core diameter 980µm, Industrial Fiber Optics) in place of the fiber couplers. Since PL does not affect the excess loss and split ratio performances, only the excess loss and split ratio experiments measure the output ports power individually without the optode's connected while the excitation sources is connected to one of the input ports.

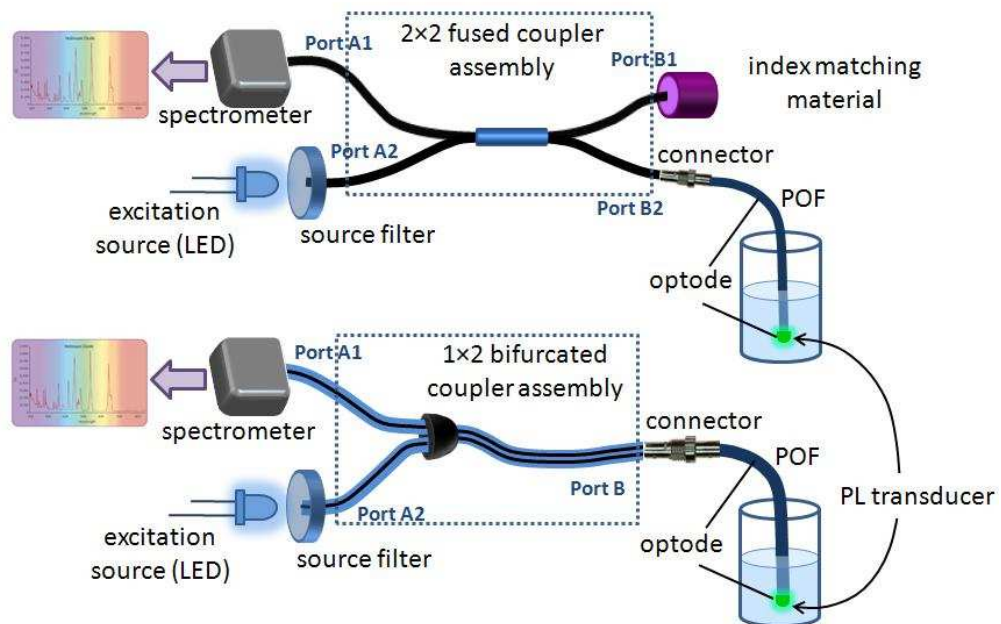


Figure 5.1. The block diagram of the back reflection experimental set up with (top), a 2x2 fused coupler assembly and (bottom), a 1x2 bifurcated coupler assembly.

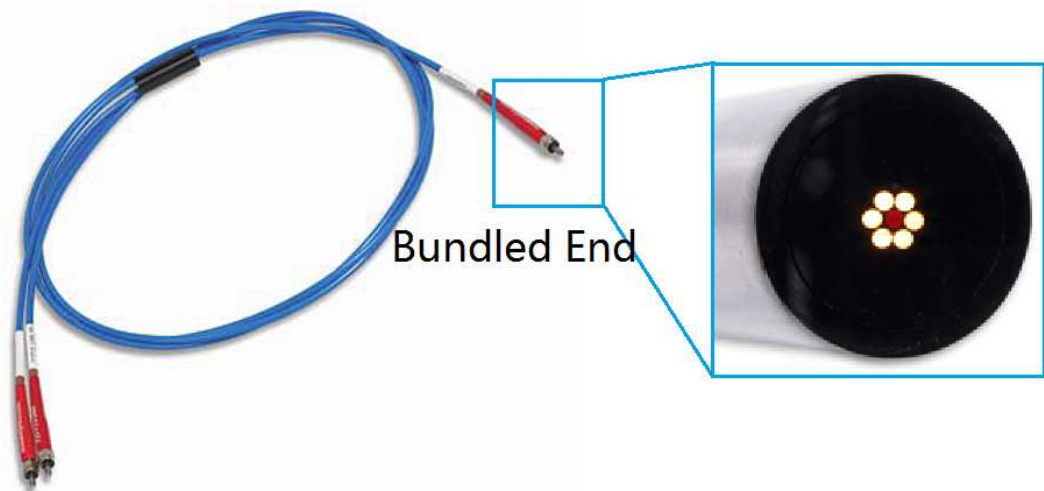


Figure 5.2. An example photo of a bifurcated fiber assembly (left), and the cross section illustration of the bundled end (right). In this specific example of an assembly, the red dot in the cross section illustration indicates the bundled port of the bifurcated fiber assembly is composed with a single fiber that extends into one branch and the other six separated fibers that extend into the other branch (shown as the six bright dots on the bundled end). Reproduced from Reference [12].

## 5.4 Split Ratio and Excess Loss Results and Discussion

This experiment is designed to characterize the split ratio and excess loss parameters of two identical  $1 \times 2$  bifurcated cable assemblies and another two identical  $2 \times 2$  3dB fused coupler assemblies. The excess loss is the measure of how efficient the assembly transmits optical power. The excess loss is determined by the physical structure, core and cladding indices of the assembly itself and is not related the coupling efficiency from the illumination source to the assembly or the coupling efficiency from the assembly to the photodetector. The split ratio can vary depending on the application and can be customized during manufacturing. The most commonly used split ratio of the optical pathway splitting assemblies is 50:50 (3 dB). For an ideal 3 dB splitter with mirrors at the output ends, after a roundtrip in the assembly, the reflected optical power would be

25% of the input power; and for a 90:10 splitter, the resultant optical power becomes 9%. Hence, the readers may have an argument of that the split ratio has very little effect on the optical power transmission because even with a very non-uniform split ratio the assembly still maintains around half of the roundtrip power compared to the assembly with an ideal 3 dB split ratio. However, fluorescence or phosphorescence emission have very low budget in optical power, so a small loss in optical power can bury the PL signals under the noise level. Moreover, with multiple assemblies used in a multi-channel apparatus, the uniformity of the assembly is affects the uniformity between channels.

The split ratio of an optical fiber coupler is defined as the ratio of the optical powers between all output ports of the coupler, or

$$SR_1 : SR_2 : \dots : SR_n = \frac{P_1}{\sum_{i=1}^n P_i} : \frac{P_2}{\sum_{i=1}^n P_i} : \dots : \frac{P_n}{\sum_{i=1}^n P_i} \quad 5-1$$

where  $P_i$  is the optical power at the  $i^{\text{th}}$  output port. For split ratio measurement with the fused coupler assembly, the excitation source is fixed at port A2 of the assembly, and the output powers,  $P_1$  and  $P_2$ , are measured at port B1 and B2 respectively. For split ratio measurement with the bifurcated fiber assembly, the excitation source is placed at port B, and the output power,  $P_1$  and  $P_2$ , are measured at port A1 and A2. Measured optical power is obtained from integrating over entire measurement spectral range.

The excess loss is defined as the amount of optical power lost in the coupler at all outputs compared to the coupled optical power at the input. It is defined as

$$Excess Loss (dB) = -10 \cdot \log \left( \frac{\sum_{i=1}^n P_i}{P_{input}} \right) \quad 5-2$$

where  $P_i$  is the optical power at the  $i^{\text{th}}$  output port, and  $P_{input}$  is the launched optical power at the input port. For the excess loss experiments, the input launched optical power is measured using a 20 cm long single core with core cross sectional area equal to that of the illumination source port of the fiber assemblies.

The experimental results of the excess loss and the split ratio with both kinds of assemblies, as shown in Figure 5.3, indicates less excess loss and more uniformity in the split ratio is achieved with the bifurcated fiber assemblies compared to the fused fiber couplers. Between the two types of 3 dB fiber splitter assemblies, as expected, the bifurcated fiber assemblies exhibit a split ratio closer to 50:50 due to that the coupled optical power in both fiber branches is only related to the cross sectional areas and NA. Higher excess loss is observed in fused fiber couplers than it is in the bifurcated fiber assemblies, and this is due to optical power lost in the fractional mismatched modes in the coupling region of the fused fiber coupler.

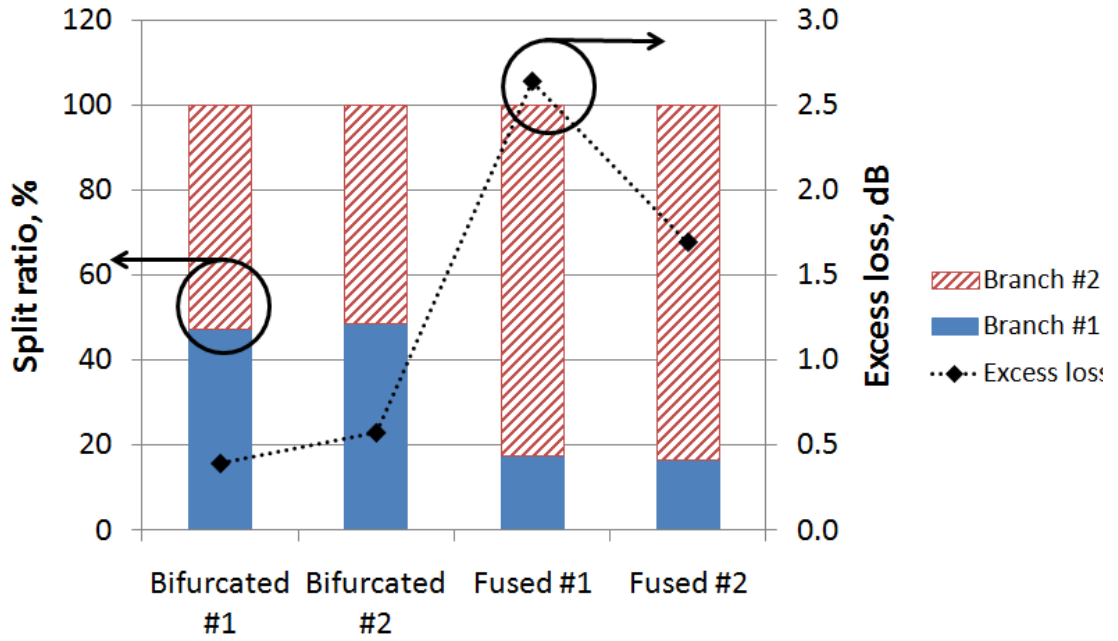


Figure 5.3. The plot of split ratio and excess loss of two 1×2 bifurcated cable assemblies and two 2×2 3dB fused coupler assemblies.

### 5.5 Back Reflection Results and Discussion

The back reflection of a fiber splitter assembly is defined as the reflected optical power from the output ports due to the index mismatch between the fiber core and the medium where the output ports are located. Derived from the Fresnel reflection equation, a theoretical expression of the back reflection,  $P_{BR}$ , is

$$\frac{P_{BR}}{P_{input}} = 10^{-\left(2 \frac{Excess\ Loss\ (dB)}{10}\right)} \cdot SR_1\% \cdot SR_2\% \cdot \left[ \left(\frac{n_c - n_{m1}}{n_c + n_{m1}}\right)^2 + \left(\frac{n_c - n_{m2}}{n_c + n_{m2}}\right)^2 \right] \tag{5-3}$$

where  $P_{input}$  is the coupled optical power at the input port,  $SR_1 : SR_2$  is the measured split ratio of the 3 dB assemblies,  $n_c$  should be the effective refractive index of the fiber which

is nearly the same as the refractive index of the fiber core for multimode fibers, and  $n_{m1}$  and  $n_{m2}$  are the refractive indices of the medium where the fiber splitter assemblies output ports are exposed to. The index of refraction of fiber core material, polymethylmethacrylate (PMMA), is 1.49. Therefore, to calculate the back reflection power as a fraction of the coupled optical power at the input port,  $n_{m1}$  is approximated as the refractive index of the silicone gel, 1.40, for the output port connected to an optode, and  $n_{m2}$  is the refractive index of the index-matching material, which varies from 1.00 to 1.50. Experimental results were obtained with the index-matching materials of air ( $n_{m2} = 1$ ), water ( $n_{m2} = 1.33$ ), silicone gel ( $n_{m2} = 1.40$ ), and a 50 cm long ST-connectorized PMMA fiber tightly wrapped around a 1 cm diameter rod for as many times as the fiber allows ( $n_{m2} = 1.49$ ), which creates fiber bent at a very small radius and thus significantly increases the loss in the connected fiber so that the amount of optical power reaching the interface at the fiber end is minimal. Since the bifurcated fiber assembly with an optode attached to the single output port is not compatible with any index matching method, the back reflection of the bifurcated fiber assembly is solely dependent on the connected material at the bundled end, which is an optode with the distal end covered in silicone gel. The back reflection of a bifurcated fiber assembly is

$$\frac{P_{BR}}{P_{input}} = 10^{-\left(2 \cdot \frac{Excess\ Loss\ (dB)}{10}\right)} \cdot \frac{A_{det}}{\sum_i^n A_i} \cdot \left(\frac{n_c - n_o}{n_c + n_o}\right)^2 \quad 5-4$$

where  $A_{det}$  is the core cross sectional area of the photodetector fiber branch, Port A1 as shown in Figure 5.1,  $\sum_i^n A_i$  is the sum of all core cross sectional areas of all fiber branches at the bundled end of the bifurcated fiber assembly,  $n_o$  is the refractive index of

the material covering the optode's distal end. Experimental and calculation results of the back reflection measurements are shown in Figure 5.4.

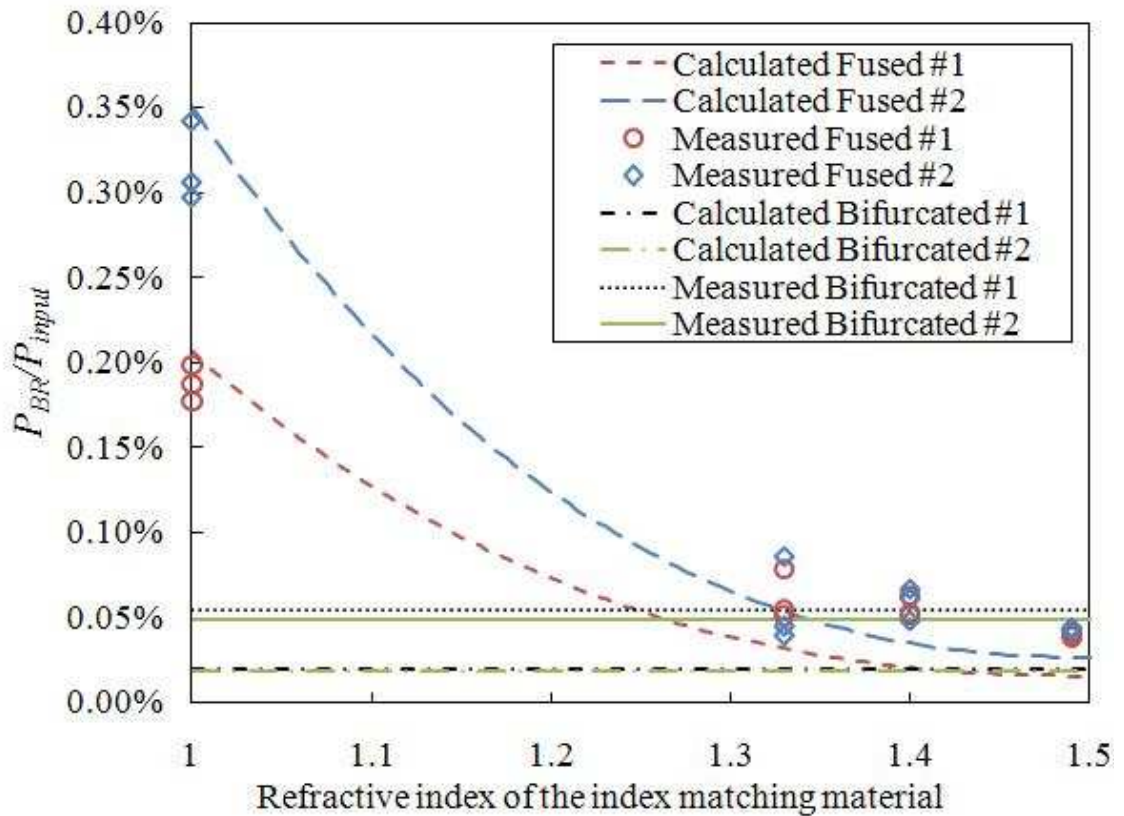


Figure 5.4. Experimental and theoretical results of the back reflection as a fraction of the input optical power with two 1×2 3dB bifurcated fiber assemblies and two 2×2 3dB fused coupler assemblies. Because the bifurcated fiber assembly has only a single output port, the experiments with various index matching materials were performed with only the two fused fiber coupler assemblies. Experiments with fused fiber coupler assemblies were repeated three times for each kind of index matching material. Experimental and theoretical results with bifurcated fiber assemblies were measured and calculated with the unit bundled end connected to an optode with its distal end covered in silicone gel which is used as the carrier for the biosensors in analyte measurement scenarios.

The calculation results in Figure 5.4 show that the bifurcated fiber assemblies have much less back reflection optical power than the fused fiber couplers do when the index

of the index matching material,  $n_{m2}$ , is not well matched with the index of the fiber core. This is because the large indices mismatch of the fused fiber couplers results in large back reflection intensities. However, as  $n_{m2}$  increases its value closer to the value of the index of the fiber core  $n_c$ , (i.e.  $1.35 < n_{m2} < n_c$ ), the calculated back reflection intensity of the fused fiber coupler drops below the back reflection intensity of the bifurcated fiber assembly.

The experimental results shown in Figure 5.4, which agree with the calculations, show that as the index of the index matching material increases closer to the index of the fiber core, the back reflection optical power of the fused fiber coupler drops from above to below the back reflection of the bifurcated fiber assembly. In other words, with appropriate index matching material, the fused fiber couplers have smaller back reflection than the bifurcated cable assemblies. The small inconsistency in the magnitude between the measured results and the calculated results of the back reflection is due to small uncertainties in the measured input power with the single core fiber optic due to excess loss and coupling loss being less than the calculated input power in the ideal case.

## **5.6 Coupling Efficiency Results and Discussion**

PL-based biosensor systems often observe very faint PL signals, and as a result, the system requires the optical pathway splitting mechanism to have a high coupling efficiency between the sensor and the system. Although the bifurcated fiber assembly has a superior performance in excess loss compared to the fused fiber coupler, the bundled end structure of the bifurcated fiber assembly results in a worse coupling efficiency between an optode fiber and the assembly, as shown in Figure 5.5. On the

other hand, the fused fiber coupler has its branch fiber core area entirely overlapping the optode fiber's core, so the coupling efficiency of the fused fiber coupler depends only on the excess loss and the split ratio.

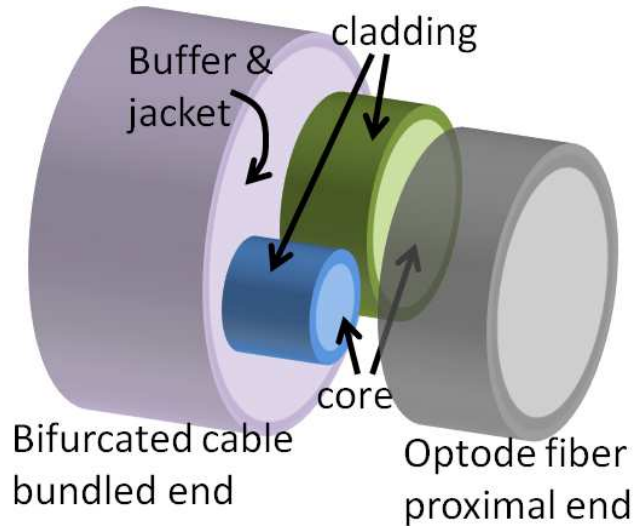


Figure 5.5. A 3D illustration of the configuration of the coupling between an optode fiber proximal end and a bifurcated cable bundled end.

Because of the tradeoff between using the two types of the fiber assemblies, an analysis was carried out to compare the coupling efficiency of both kinds of the coupler assemblies. In the simulation, all fiber assemblies are assumed to have no excess loss. Simulations were performed with varying of split ratios for both types of fiber assemblies. The split ratio is defined as  $SR_D:SR_S$ , where  $SR_D$  is the split ratio at the detector branch fiber and  $SR_S$  is the split ratio at the source branch fiber. For large core size multimode fiber coupling with the same core and cladding materials, the coupling efficiency is calculated based on the over lapping core area between two interfaced fiber

optics ( $S_1$  or  $S_2$ ). For instance, coupling efficiency from the bifurcated cable bundled end to the optode fiber's proximal end is calculated from the following equation,

$$\eta_1 = \frac{S_2}{\pi R_2^2} = \frac{R_2^2 \cos^{-1}\left(\frac{d^2+R_2^2-R^2}{2dR_2}\right) + R^2 \cos^{-1}\left(\frac{d^2+R^2-R_2^2}{2dR}\right) \frac{1}{2} \sqrt{(-d+R_2+R)(d+R_2-R)(d-R_2+R)(d+R_2+R)}}{\pi R_2^2}, \quad 5-5$$

where  $d$  is the distance between the two centers of the source end branch fiber core and the optode fiber's proximal end fiber core, and the other variables have their dimensions shown in Figure 5.6. So when calculating the coupling efficiency of the fiber assembly in the system, a roundtrip is considered with the forward path coupling of the excitation light and the backward path coupling of PL from the excitation source to the optode and back to the photodetector. Assuming the sensor at the distal end of the optode emits PL that has the same power as the excitation optical power it receives, also 100% of the emitted PL power gets coupled back into the optode fiber. Although this assumption is not realistic, the PL yield of the sensor has no impact on the analysis of the fiber coupler assembly coupling efficiency, and for the simplicity of the calculations, this assumption stands for this analysis. When the input excitation power is independent of the source branch fiber's cross sectional area, the coupling efficiency of a bifurcated fiber assembly is calculated from

$$\frac{P_{PD}}{P_{in}} = \eta_1 \cdot \eta_2 = \frac{S_2}{\pi R_2^2} \cdot \frac{S_1}{\pi R^2}, \quad 5-6$$

where  $P_{PD}$  is the detected PL power and  $P_{in}$  is the coupled excitation power. The assumption that the coupled excitation power is independent of the cross sectional area of the coupling fiber is not the case in reality but can be easily compensated by increase the

source illumination intensity. However, if considering the input excitation power as a function of the source branch fiber cross sectional area, the coupling efficiency of a bifurcated fiber assembly, modified from Eqn. 5-6, becomes

$$\frac{P_{PD}}{P_{in}} = \eta_1 \cdot \eta_2 \cdot \eta_f = \frac{S_2}{\pi R_2^2} \cdot \frac{S_1}{\pi R^2} \cdot \frac{\pi R_2^2}{\pi R_f^2}, \quad 5-7$$

where  $\eta_f$  is the normalization factor to normalize the coupled excitation power of the bifurcated fiber assembly with the coupled excitation power of the fused fiber coupler for comparison purpose assuming unity coupled excitation power with the fused fiber coupler source branch fiber core radius of  $R_f$ , 490  $\mu\text{m}$ . The cladding thickness of all fibers is fixed to be 30  $\mu\text{m}$ , and the diameter of the bundled end of the bifurcated cable is fixed at 1.32 mm, in other words,  $2R_1 + 2R_2$  is fixed at 1.2 mm, which is the simulated upper bound value of the varying optode's fiber core radius. The values of  $R_1$  and  $R_2$  are determined by the specific split ratio of interest, as shown in Eqn. 5-8.

$$R_1 : R_2 = \sqrt{SR_1} : \sqrt{SR_2} \quad 5-8$$

Because for the same split ratio, the bifurcated cable assembly has a different source fiber branch fiber core radius than the fused fiber coupler. To normalize the coupled excitation source power, a normalization efficiency parameter is introduced for comparison purposes as

$$\eta_{Norm.} = \frac{\pi R^2}{\pi R_f^2} \quad 5-9$$

Assuming the branch fiber of the fused fiber coupler has the core diameter fixed at 980  $\mu\text{m}$  and cladding fixed at 30  $\mu\text{m}$ , the coupling efficiency of a fused fiber coupler is defined as

$$\frac{P_{PD}}{P_{in}} = SR_1 \cdot SR_2 \cdot \frac{\pi R^2}{\pi R_f^2} \quad 5-10$$

where  $R$  is the optode fiber radius,  $R_f$  is the fused fiber coupler branch core radius, which is  $490 \mu\text{m}$ ,  $SR_1$  is the split ratio at the detector branch fiber and  $SR_2$  is the split ratio at the source branch fiber.

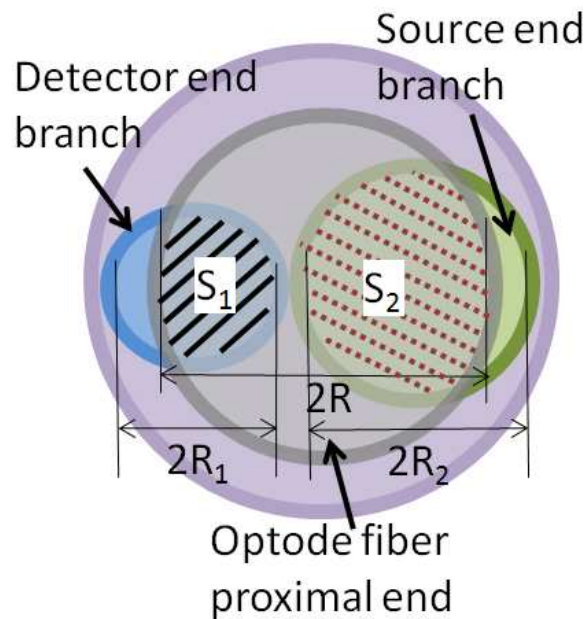


Figure 5.6. A cross-sectional illustration of the configuration of the coupling between an optode fiber proximal end and a bifurcated cable bundled end. In the drawing,  $R$  is the optode fiber core radius,  $R_1$  is the detector branch fiber core radius,  $R_2$  is the source branch fiber core radius,  $S_1$  is the overlapping area between the optode fiber proximal end and the detector branch fiber at the bundled end of the bifurcated fiber assembly, and  $S_2$  is the overlapping area between the optode fiber proximal end and the source branch fiber at the bundled end of the bifurcated fiber assembly.

The simulation varies the optode fiber core diameter from 0 to 2 mm, and the results of the coupling efficiency with both the bifurcated fiber assembly and the fused fiber coupler are shown in Figure 5.7 and Figure 5.8. Figure 5.7 shows the simulation results with the input excitation power independent of the source branch fiber's cross sectional

area calculated from Eqn. 5-6 and Eqn. 5-10, while Figure 5.8 is the calculation results with the input excitation power as a function of the source branch fiber cross sectional area calculated from Eqn. 5-8 and Eqn. 5-10. The bifurcated fiber assembly reaches the maximal coupling efficiency when the optode fiber radius is the same as the sum of the radii of the two fiber branches at the bundled end, which is  $600\ \mu\text{m}$ . The fused fiber coupler obtains the maximal coupling efficiency at the same radius as the branch fiber, which is  $490\ \mu\text{m}$ . In Figure 5.7, comparing the two types of fiber assemblies with same split ratios (shown in the same color in Figure 5.7), when connecting the larger split ratio branch to the detector, the bifurcated cable has higher coupling efficiency than the fused fiber coupler; on the other hand, when using the smaller split ratio branch as the detector branch, the bifurcated cable has comparable or lower coupling efficiency than the fused fiber coupler. However, if the source power is fixed and the coupled excitation power is proportional to the cross sectional area of the source branch fiber, the results of coupling efficiency with the bifurcated fiber assembly are altered, as shown in Figure 5.8. Regardless of which branch of the assembly connected to the detector or the source, bifurcated fiber assembly has the same coupling efficiency with the same split ratio. Comparing the two types of the fiber assemblies, the fused fiber coupler has approximately 3 times higher maximal coupling efficiency than the bifurcated fiber assembly with the same split ratio. Keeping in mind that the simulation does not consider the excess loss, the experimental results suggested that the fused fiber coupler (with excess loss of 2.6 dB or 55% and 1.7 dB or 68 % for the two units under test) has slightly worse performance in excess loss than the bifurcated fiber assembly (with excess loss of 0.39 dB or 88% and 0.57 dB or 91% for the two units under test). However, even with

the disadvantages in excess loss, the fused fiber coupler appear to have a higher coupling efficiency than the bifurcated fiber assembly.

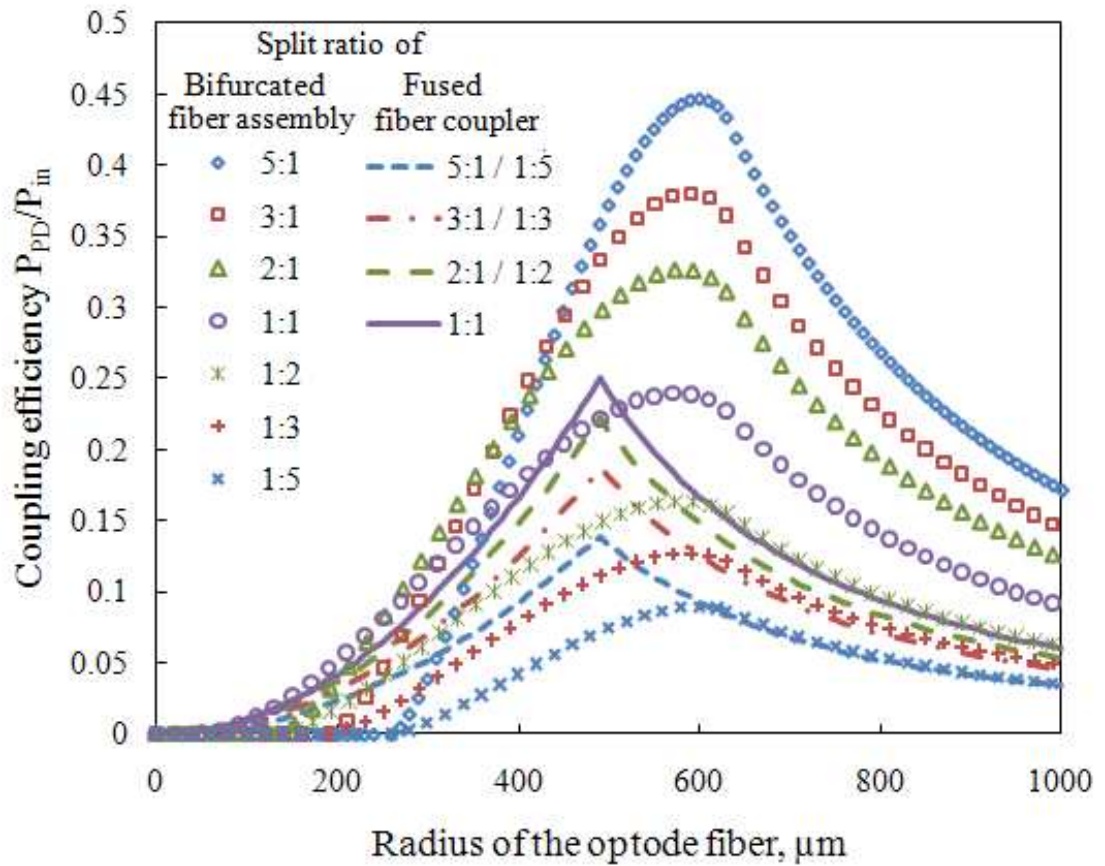


Figure 5.7. The simulation results of the coupling efficiency with both the bifurcated fiber assembly and the fused fiber coupler with the input excitation power is independent of the source branch fiber's cross sectional area.

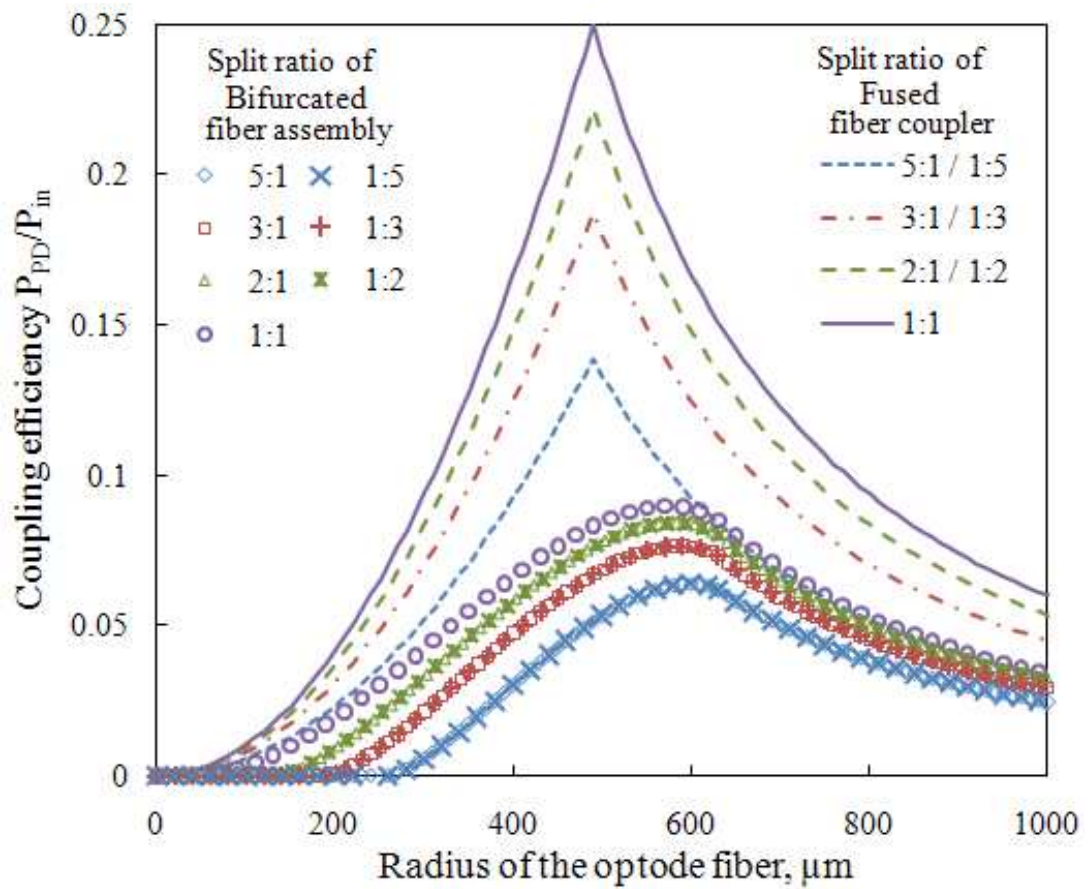


Figure 5.8. The simulation results of the coupling efficiency with both the bifurcated fiber assembly and the fused fiber coupler with the input excitation power is proportional to the source branch fiber's cross sectional area.

## 5.7 References

- [1] K. F. Reardon, Z. Zhong, and K. L. Lear, "Environmental applications of photoluminescence-based biosensors," in *Advances in Biochemical Engineering/Biotechnology*, T. Scheper, Ed.: Springer, 2010, ch. 116, pp. 99-123.
- [2] Z. Rosenzweig and R. Kopelman, "Analytical Properties and Sensor Size Effects of a Micrometer-Sized Optical Fiber Glucose Biosensor," *Anal. Chem.*, vol. 68, no. 8, pp. 1408–1413, April 1996.
- [3] R. B. Thompson and E. R. Jones, "Enzyme-based fiber optic zinc biosensor," *Anal. Chem.*, vol. 65, no. 6, pp. 730-734, March 1993.
- [4] H. Hecht and M. Kölling, "A low-cost optode-array measuring system based on 1 mm plastic optical fibers — new technique for in situ detection and quantification of pyrite weathering processes ," *Sensors and Actuators B: Chemical*, vol. 81, no. 1, pp. 76-82, Dec. 2001.
- [5] K. F. Reardon, D. W. Campbell, and C. Müller, "Optical fiber enzymatic biosensor for reagentless measurement of ethylene dibromide," *Eng. Life Sci.*, vol. 9, no. 4, pp. 291–297, Aug 2009.
- [6] Z. Zhong et al., "Fiber Optic Monooxygenase Biosensor for Toluene Concentration Measurement in Aqueous Samples," *Biosens Bioelectron.*, vol. 26, no. 5, pp. 2407-2412, Jan 2011.
- [7] Sean B. Pieper, "Optical Characterization of Phosphorescent Dyes for Biosensor Transducer Applications," Colorado State University, Fort Collins, Thesis 2008.
- [8] M. Yasin, S. W. Harun, Pujiyanto, Z. A. Ghani, and H. Ahmad, "Performance Comparison between Plastic Based Fiber Bundle and Multimode Fused Coupler as Probes in Displacement Sensors," *Laser Physics*, vol. 20, no. 10, pp. 1890-1893, 2010.
- [9] S. Yuan and M. DeGrandpre, "Comparison Between Two Detection Systems for Fiber-Optic Chemical Sensor Applications," *Appl. Spectrosc.*, vol. 60, no. 4, pp. 465-470, Apr 2006.
- [10] M. L. Myrick, S. M. Angel, and R. Desiderio, "Comparison of some fiber optic configurations for measurement of luminescence and Raman scattering," *Applied*

*Optics*, vol. 29, no. 9, pp. 1333-1344, Mar 1990.

- [11] Y F Li and J. W. Y. Lit, "Coupling efficiency of a multimode biconical taper coupler," *J. Opt. Soc. Am. A* , vol. 2, no. 8, pp. 1301-1306, Aug 1985.
- [12] Inc. Ocean Optics. (2011, June) Reflection/Backscattering Probes. [Online].  
HYPERLINK "http://www.oceanoptics.com/Products/reflectionprobesstandard.asp"  
<http://www.oceanoptics.com/Products/reflectionprobesstandard.asp>

## Chapter 6

# **EXISTING PHOTOLUMINESCENCE (PL) - BASED FIBER OPTIC SYSTEMS COMPARISON**

### **6.1 Introduction**

To improve the measuring abilities of the existing PL-intensity-based biosensor systems, signal reading fluctuations or drifts are often observed but the noise sources of those are not straightforward to spot without a careful analysis. Different noise sources often have each own distinctive frequency characteristics. A frequency spectrum is useful to reveal not only the frequency components of all noise sources but also the power distribution of all frequency components. Three existing PL-intensity-based fiber optic enzymatic biosensor systems are analyzed and compared in this chapter. System I is a single channel system with a spectrometer as the photodetector device; System II is a lab-developed multi-channel system that has been studied and evolved few times for improvements; System III is a commercialized prototype multi-channel system that built upon System II's design with several modifications. Section 6.2 introduces the system opto-electronic hardware set-up as well as the circuitry schematics. Section 6.3 gives the spectral analysis on the three systems. Few attempts including both software and

hardware approaches were made to improve the performance of System II. Results of signal-to-noise ratio (SNR) and standard error with each system are compared.

## **6.2 Configurations**

Although the designing guidelines for all three existing PL-based fiber optic systems are the same, the system configurations are quite different between each other.

System I is a single channel spectrometer system designed and built by a former graduate student, Sean B. Pieper, at Colorado State University, and its block diagram is shown in Figure 6.1. A typical measurement set up is shown at the top of the figure, and the hardware configuration of the modular LED source box is shown at the bottom of the figure. Inside of the modular LED source box, a circuit board of the 470 nm wavelength LED (IF-E92B, Industrial Fiber Optics) turns on manually by the switch at the front panel of the box. A SMA-connecterized PMMA fiber optic cable (SH4001-1.3 980 $\mu$ m core diameter custom order, Industrial Fiber Optics) terminated at the other end with the bare fiber end exposed, connected the LED fiber coupling housing to the in-line filter holder (FHS-UV, Ocean Optics). The in-line filter holder is the fixture to hold the source filter (HQ450/60m, Chroma Technology) to cut off the unwanted wavelength of the LED spectrum, which could overlap the fluoreophore emission spectrum and cause false PL intensity readings. The output of the filter holder is connected with a SMA-SMA connecterized PMMA fiber, and the other end of the fiber is connected to the SMA mating sleeve mounted on the front panel of the box, which connects the 1 $\times$ 2 bifurcated cable assembly (BIF-600-UV-VIS, SMA, Ocean Optics). The bifurcated cable assembly has its bundled end connected to an optode, and the other split end connected to an

spectrometer (USB-4000-FL, Ocean Optics) which outputs the spectral information to a PC through a USB interface. For a detailed configuration, pictures, and the bill of material (BOM) of the modular LED source box, refer to Reference [1].

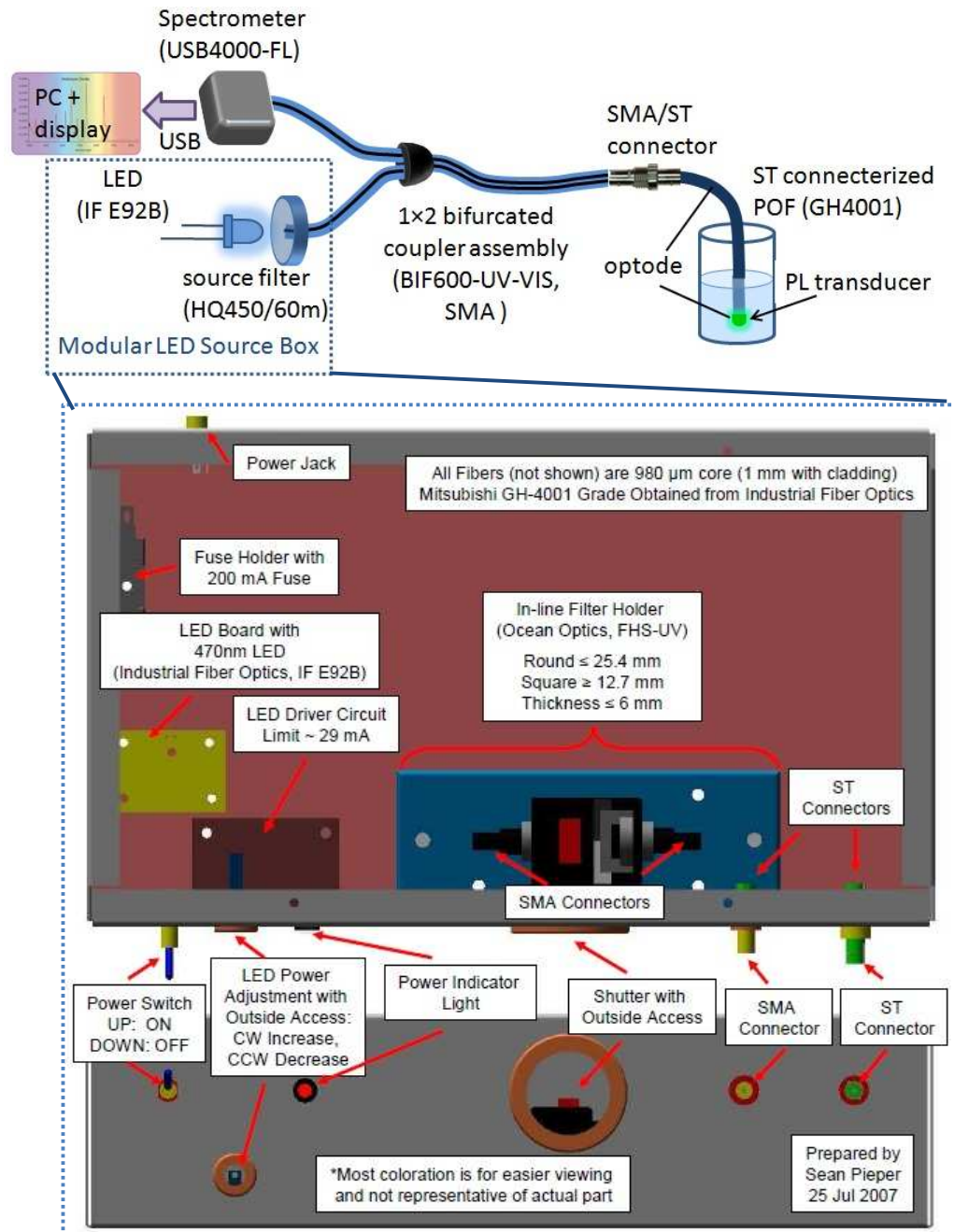


Figure 6.1. A block diagram of System I configuration. Modular LED source box schematics is reproduced from Reference [1].

System II is a lab-developed multi-channel system prototype that was constructed at Colorado State University by multiple senior design groups and graduate students. A typical experimental set up is shown in Figure 6.2, and the system I/O circuit schematic drawing is shown in Figure 6.3. The PMT module (H5783-01, Hamamatsu) used in System II has output of analog current, thus the system I/O circuit is composed with current-to-voltage front end, this case the 240  $\Omega$  resistor shown in Figure 6.3, and a voltage amplifier before the voltage signals are fed into a USB data acquisition module (iUSBDAQ - U120816, Hytek) and output to a PC. For a detailed configuration, pictures, and the BOM of System II, refer to Appendix E.

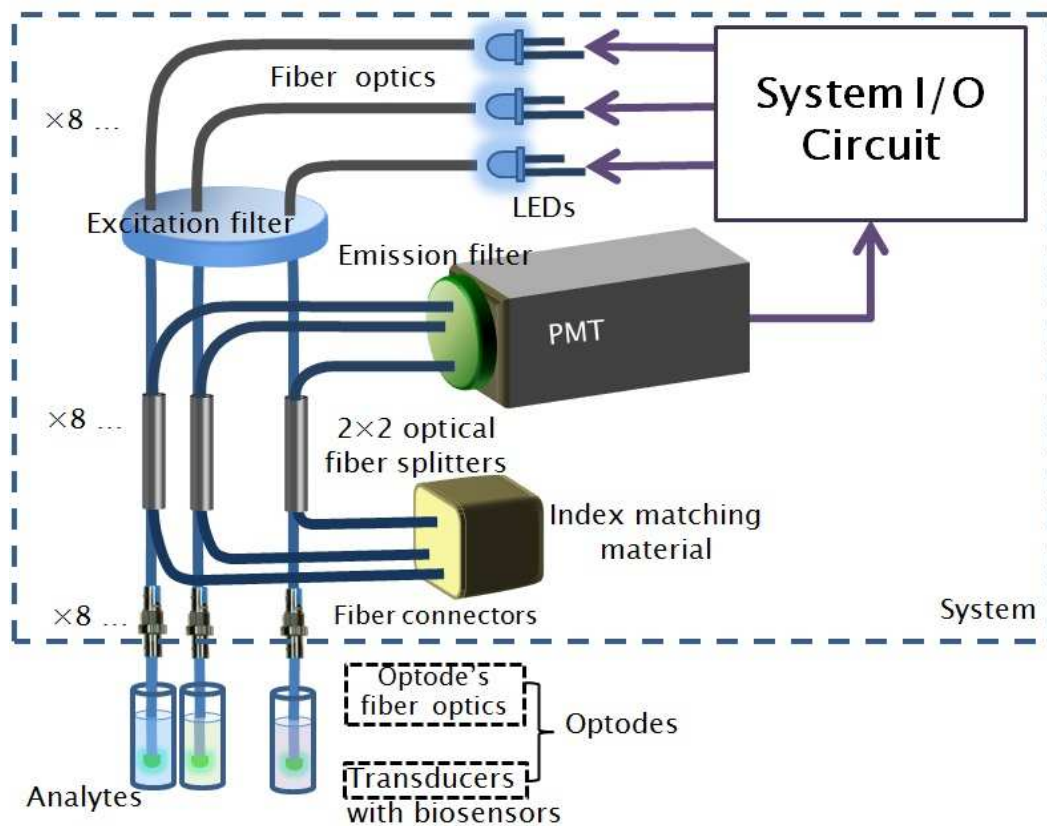


Figure 6.2. The block diagram of System II typical experimental set up.

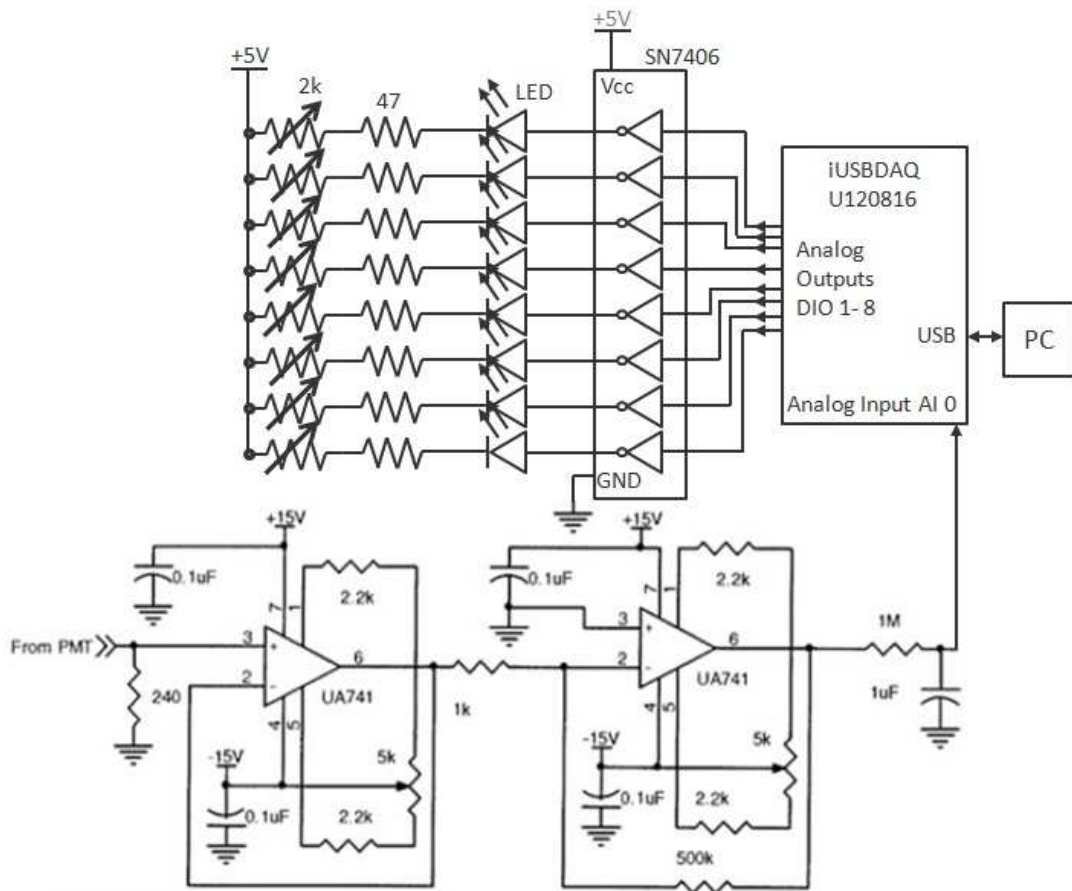


Figure 6.3. Schematic drawing of the System I/O circuit of System II.

System III is a commercial available prototype of the multi-channel system built by OptiEnz Inc, in 2010. Typical experimental set up is the same as System II, shown in Figure 6.2, and the difference is the system I/O circuit, as shown in Figure 6.4. Because a different PMT module that has a built-in transimpedance (TIA) is used in System III, the PMT output is digitized without any pre-amplification and read out by the microprocessor. For a detailed configuration, pictures, and the BOM of System II, refer to Chapter 4 and Appendix F.

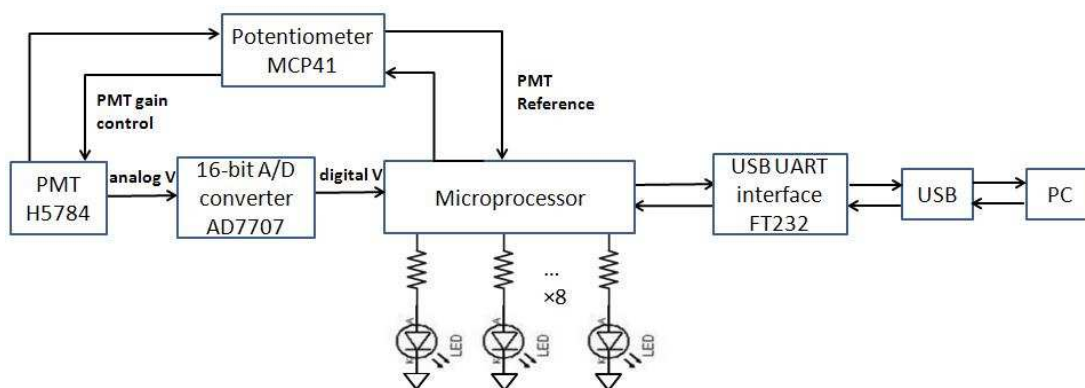


Figure 6.4. Schematic drawing of the System I/O circuit of System III.

### 6.3 Noise Analysis

Before the OptiEnz commercial prototype unit, System III, was designed and built, the single channel spectrometer system, System I, and the lab-based multi-channel system, System II, were first analyzed, compared, and improved. Although the PL intensities are not the points of interests for the frequency analysis, to avoid varying unnecessary variables, all measurements were performed using the same pH sensitive FLA optode exposed in the same pH solution. Data obtained from System II was on Channel 2. The number of data points taken with System I and II were both 136 and the same for all cases in this chapter. A fast Fourier transform (FFT) was performed on the two sets of data, shown in Figure 6.5. The frequency range is determined by the sampling frequency of each system, and the sampling frequency is 1 Hz for System I and 0.67 Hz for System II. Since all measurements are DC signals, it is obvious to see the majority power is distributed at the 0 frequency. For a clearer view of the power distribution of the rest of the frequency components, the y-axis is zoomed in from 0 to  $2 \times 10^{-3}$  in the figures. Both systems have the noise frequency distributed evenly throughout the spectra, thus it is fair

to conclude the most significant noise source is white noise. The signal-to-noise ratio (SNR) is 25.6 for System I and 10.2 for System II, as summarized in Table 6.1.

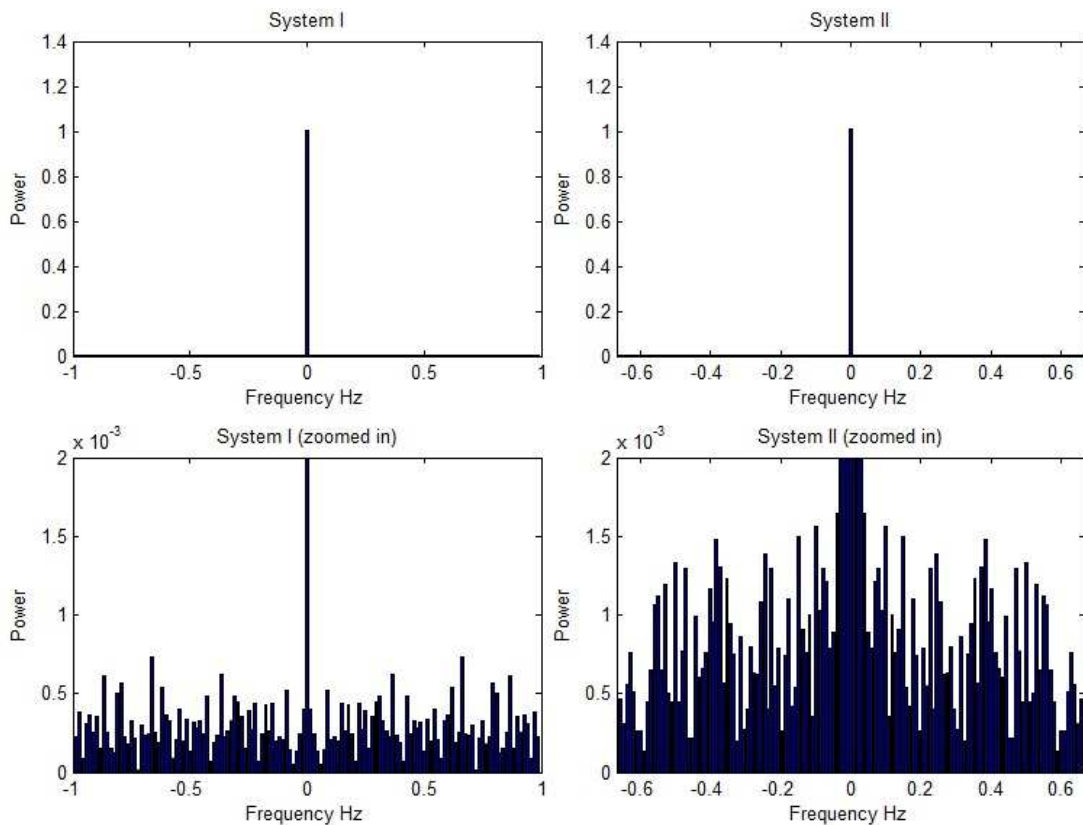


Figure 6.5. The frequency spectra of the same number (136) of data points for System I and System II (top). For a clearer view of the power distribution of all frequency components, the y-axis is zoomed in from 0 to  $2 \times 10^{-3}$  (bottom).

To improve the signal to noise performance of System II to be at least comparable to the single channel system, first software approaches were attempted. The LabVIEW program that controls the data acquisition unit and thus communicate with the system was modified, as shown in Figure 6.6. The first method, System II Software Method 1, was to average every 5 data points taken after 5 sampling time intervals; and the second method, System II Software Method 2, was to take 5 data points during the same

sampling time interval and average the 5 data points in each interval. The results of the two methods are shown in Figure 6.7. Spectra results are not able to provide a straightforward conclusion of the noise level increase or decrease. Calculation results show that SNR is not improved with Software Method 1 and drops from 10.2 to 8.83, but sustained comparable or slightly improved at 10.3 with Software Method 2. Overall the software approach does not have significant improvement to System II.

**USER INPUTS**

**Enter the number of channels to measure (1-8)** **Hytek Analog input**

**Enter the dwell time of a single channel (ms)(between 100 ms to 10s)**

**Averaging every # data points**

Data is taken from LabVIEW program: version8.2\_Multichannel Acquisition \_darkvoltage\_autosubtract\_averaging.vi

USER NOTES/COMMENTS

This measurement was taken on Wednesday, March 17, 2010

Dwell Time for each channel LED (ms) 500

Total Elapsed time (ms) 10109574.02

Averaged from # of data points

5

TIME	CHANNEL 0 (V)	CHANNEL 1 (V)	Ch1 StD	CHANNEL 2 (V)	Ch2 StD	CHANNEL 3 (V)	Ch3 StD	CI
4:26:24 PM	0.173	0.0744	0.00251	0.362	0.001414	0.0308	0.002775	
4:26:33 PM	0.172	0.075	0.002915	0.367	0.004	0.0328	0.000837	
4:26:41 PM	0.176	0.0708	0.000837	0.3632	0.002683	0.0328	0.001483	

Figure 6.6. A screen shot of the modified LabVIEW program (top) with added user's input parameter, and the output file format (bottom) for the software approach. LabVIEW program name that the output file generated from shown in the header of the file is to distinguish between Method 1 and 2.

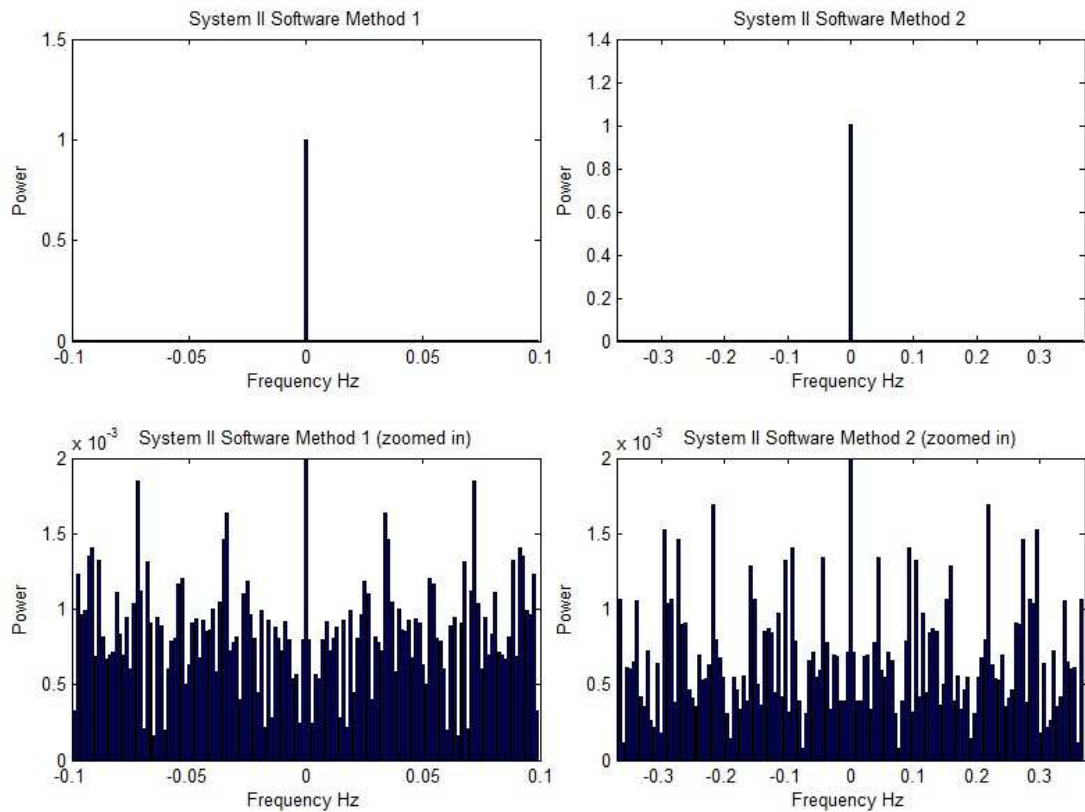


Figure 6.7. The frequency spectra of the same number of data points for System II after the software adjustment method 1 and 2 (top). For a clearer view of the power distribution of all frequency components, the y-axis is zoomed in from 0 to  $2 \times 10^{-3}$  (bottom).

The second approach to improve System II is through hardware modification. The existing design of the output signal processing circuit, as shown in Figure 6.3, PMT dumps the current out into the  $240 \Omega$  resistor followed by the first operational amplifier (op-amp) acting as a buffer, and the second op-amp is a voltage amplifier. So if the front end resistor is fairly large to maintain a decent pre-amplification, the response becomes very slow because the signal decay time constant,  $\tau = R \times C$ , becomes aggressively large [2]. Otherwise, a small front end resistor results in a small pre-amplification which could cause a faint signal to be buried in the system noise. Moreover, the non-inverting input

of the first buffer op-amp has a bias current, which could be a significant noise source mixed with the signal before being amplified. The original design uses an op-amp (UA741) that has a very significant bias current up to 0.5  $\mu\text{A}$ , and the PMT current is generally in nA and  $\mu\text{A}$  range. To avoid the compromise between the slow, noisy response and the significant noise source, it is a good idea to feed the PMT output current directly into the summing point of a TIA, shown in Figure 6.8. Before building the circuit up, a Spice simulation was performed and results are shown in Figure 6.9. Both op-amps used in the new TIA circuit have very low bias current of 10 to 70 nV/ $\sqrt{\text{Hz}}$ . The design can sustain a considerably large amplification to improve the SNR without trading in a fast clean response. Then the design was breadboarded with the first stage TIA circuit and integrated into the system. The results of the frequency response of the new design is shown in Figure 6.10. Two different feedback resistance values, 2M $\Omega$  and 10M $\Omega$ , were chosen as the Hardware Method 1 and 2. The SNR of the two methods are bumped up to 11.1 and 23.2, which is significantly better than the original 10.2 and comparable to 25.6 of System I, as shown in Table 6.1.

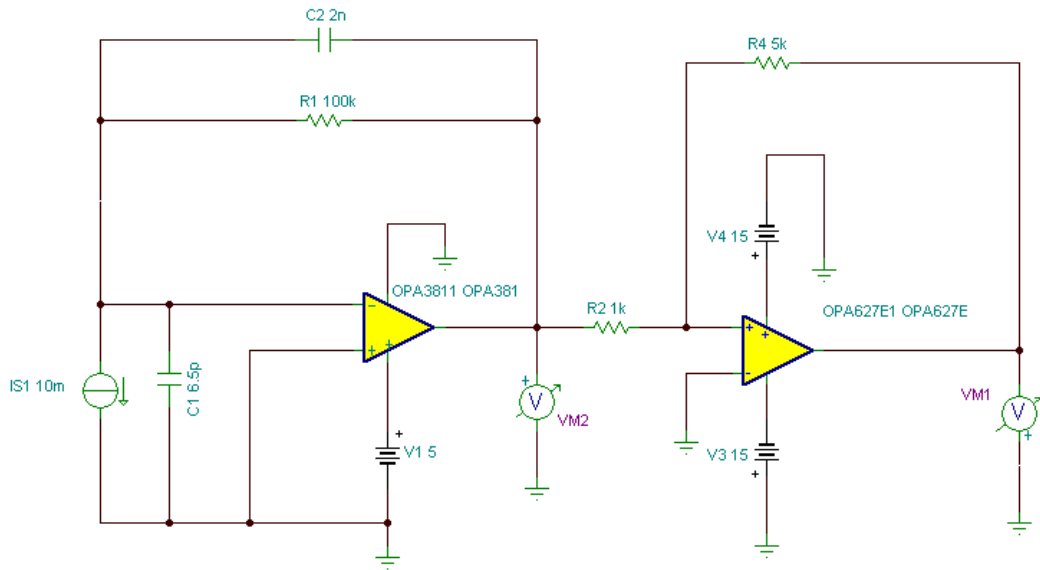


Figure 6.8. A schematic drawing of the new TIA circuit design.

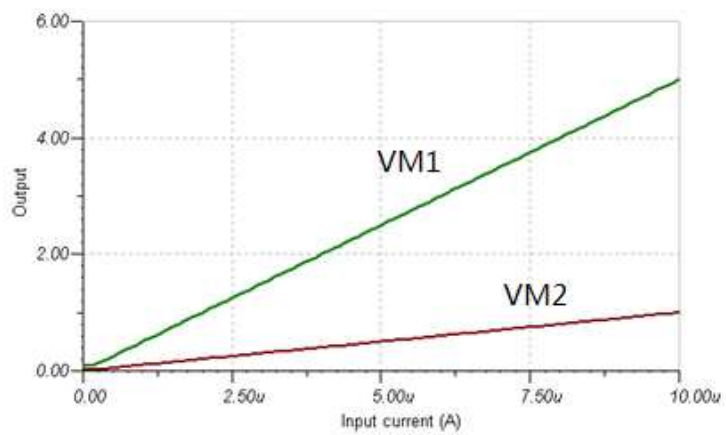


Figure 6.9 A Spice simulation result of the modified TIA circuit.

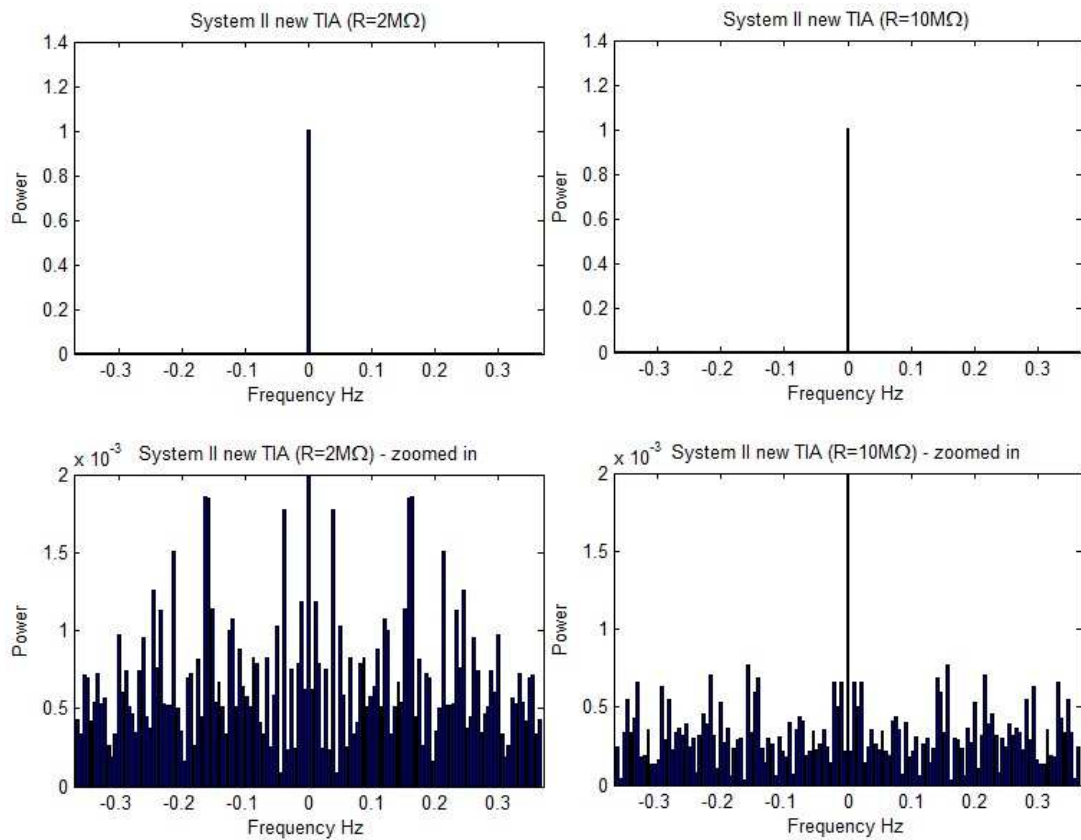


Figure 6.10. The frequency spectra of the same number of data points for System II after implementing the new TIA circuit design with different feedback resistance values of  $2\text{M}\Omega$  and  $10\text{M}\Omega$  (top). For a clearer view of the power distribution of all frequency components, the y-axis is zoomed in from 0 to  $2 \times 10^{-3}$  (bottom).

Evolved from the lab-developed systems, System III was built and analyzed. Two major improvements are using a PMT module with a built-in TIA and a higher bits A/D converter. Frequency analysis of System III is shown in Figure 6.11. The noise level of System III drops significantly compared to the other systems, and the dominant noise source becomes the  $1/f$  and  $1/f^2$  noise. SNR increases to 167.9 from the original 10.2. A comparison of SNR and standard error between all three systems is shown in Table 6.1.

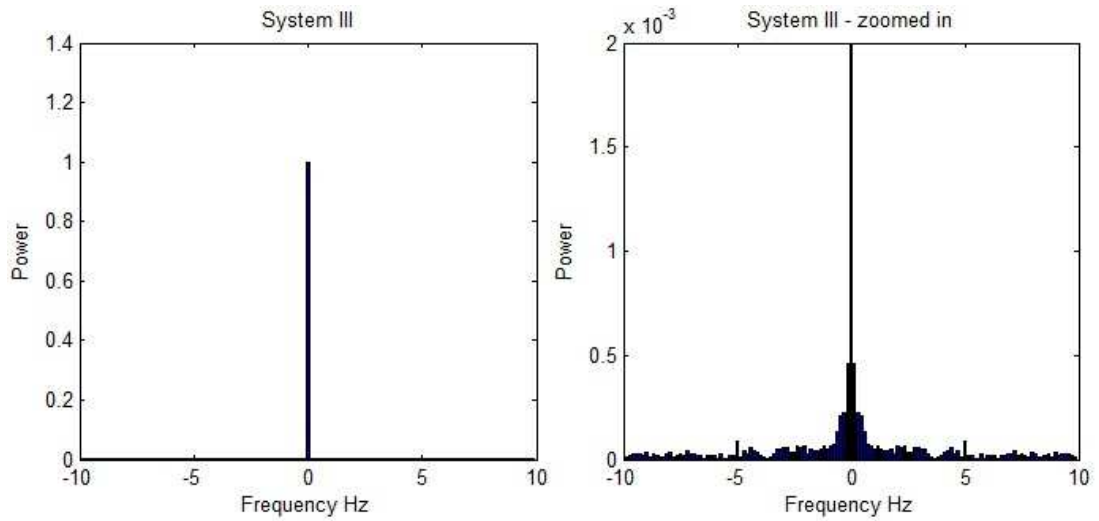


Figure 6.11. The frequency spectrum of the same number of data points for System III (left). For a clearer view of the power distribution of all frequency components, the y-axis is zoomed in from 0 to  $2 \times 10^{-3}$  (right).

TABLE 6.1  
A COMPARISON OF SNR FOR THREE EXISTING SYSTEMS

System	Modification	Standard Error	SNR
System I	N/A	0.033%	25.6
	N/A	0.109%	10.2
	Software Method 1	0.091%	8.83
System II	Software Method 2	0.075%	11.3
	Hardware Method 1	0.077%	11.1
	Hardware Method 2	0.037%	23.2
System III	N/A	0.008%	167.9

## 6.4References

- [1] Sean B. Pieper, "Modular Light Emitting Diode Source," in *Optical Characterization of Phosphorescent Dyes for Biosensor Transducer Applications*. Fort Collins, CO, USA: Colorado State University, 2008, ch. Appendix F, pp. 195-209.
- [2] A. G. Wright, "Amplifiers for use with photomultipliers—who needs them?," *Nuclear Instruments and Methods in Physics Research A*, vol. 504, pp. 245-249, 2003.

# Chapter 7

## CONCLUSION AND FUTURE WORK

### 7.1 Conclusion

The improvements of a multi-channel fiber optic photoluminescence (PL) based biosensor system for environmental toxic chemical compounds detection has been presented. Measurements of the detection abilities of the system have been carried out with the sensitivity and the limit of detection. Using pH-sensitive fluoresceinamine (FLA) as the transducer of the optodes for all characterization measurements, sensitivity of the system is  $8.66 \times 10^5 \text{ M}^{-1}$  as the Stern-Volmer constant,  $K_{SV}$ , in the  $\text{H}^+$  concentration measurement range of 0.002 - 891  $\mu\text{M}$  (pH of 3.05 - 8.69). Furthermore, the channel-to-channel uniformity is characterized to have sensitivities to be within the 95% confidence level of all channels. Based on the experimental results in combination with the  $\text{H}^+$  production of appropriate enzymes, the calculated limit of detection (LOD) of the system can be as low as 0.08  $\mu\text{g/L}$  for 1,2-dichloroethane (DCA) and 0.14  $\mu\text{g/L}$  for ethylene dibromide (EDB). In comparison, the minimum detectable change calculated

using the same approach in this work as others reported in the literature is lower than other reported values. During the characterization processes, non-ideality in the classic Stern-Volmer equations were observed. Besides a previously reported factor of the fractional accessibility of the fluorophores, another non-ideality factor of back reflection was found, proved, and mathematically modeled. Both of the non-ideality factors of the classic Stern-Volmer equation were incorporated into a modified Stern-Volmer equation to describe the non-idealities of the overall sensing system.

The performances of fused fiber coupler and bifurcated fiber assembly were investigated for applications in the photoluminescence (PL)-based biosensor systems. Complex tradeoffs among back reflection interference, coupling efficiency and split ratio were analyzed with theoretical and experimental data. Bifurcated fiber assemblies have more uniform split ratio and better excess loss performance than those of the fused fiber couplers. However, due to the configuration differences of the two kinds of the fiber assemblies, the fused fiber coupler can eliminate the back reflection interference to as low as 0.04% of the input optical power by using the index matching method while the bifurcated fiber assemblies do not have the options to apply the method. Furthermore, the coupling efficiency of both kinds of the fiber assemblies were investigated through simulations. For the two types of assemblies with the same split ratio, the fused fiber coupler has a maximum coupling efficiency of 25% while the bifurcated cable is only able to achieve a 9% maximum coupling efficiency.

To improve the measuring abilities of the existing PL-intensity-based biosensor systems, the noise sources that cause the fluctuations and drift in the measurements were investigated by using the power distributions in the frequency domain. Both two

software approaches and two hardware approaches were attempted to improve the signal-to-noise performance of a laboratory-developed multi-channel fiber optic PL-based biosensor system. The hardware approach improved the signal-to-noise ratio of the system from 10.2 to 23.2, and standard error of the measurements from 0.109% to 0.037%.

## **7.2 Future Work**

Future work is expected to continue the exploration of the non-idealities of the classic Stern-Volmer relationship and the correction for them. The current studies in this thesis have included some possible causes of the back reflection factor, yet the causes of the fractional accessibility factor of the non-ideality in other literatures have not been reported with experimental proof. To continue the research in this path, the following aspects of the problem are suggested to be investigated, the fluorophore concentration dependency, the fluorophore in poly vinyl alcohol matrix (PVA) layer thickness dependency, as well as the temperature dependency to the fraction of the inaccessibility of the fluorophore. These factors may all contribute to the fractional accessibility of the fluorophore and thus cause the non-ideality in the classic Stern-Volmer relationship of the quenching process. Furthermore, a more accurate mathematical model describing all the non-ideality factors needs to be structured.

Another area to be pursued is the emission intensity dependencies, such as the factors of the excitation optical intensity, the fluorophore concentration, the fluorophore in PVA matrix layer thickness, etc. How those factors can affect the emission intensity of the fluorophore has not yet been quantitatively defined.

Some work towards the integration of an excitation source intensity monitor and calibration system should be attempted. After exploring the dependency of the excitation source intensity, monitoring this parameter can be helpful to a calibration process in the environmental applications. The spare branch of the fused fiber coupler in the system can be used for the place to integrate a photodetector. The readings of the photodetector can be used to construct a feedback system for a calibration process. The goal is to develop an automated calibration process into the system before the actual analyte measurements.

Another area of interest may be the preservation of the optodes (without the enzyme component) and its impact on the sensitivity of the detection. A suspicion of fluorophore degradation throughout the preservation has been raised during the course of this thesis research. A quantitative investigation of the optodes degradation rate can be very useful to the future measurements.

# Appendix A

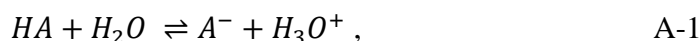
## PH BUFFER SOLUTIONS PROTOCOLS

### A.1 Introduction

All pH buffer solutions used in this thesis for system characterizations with pH-sensitive optodes measurements were made followed the protocols described in this appendix. A buffer solution is consist of an acid and its conjugate base or a base with its conjugate acid. Buffer solutions have the ability of maintaining a nearly constant pH value as a small amount of acid or base is added. With a known pH buffer solution, the fluorophore quencher,  $H^+$ , concentration can be easily calculated using pH definition. The calculation principles of the pH buffer solutions is included in Section A.2. Procedures of making pH buffer solutions are documented. First step is to make 1 M stock solutions as stated in Section A.3. The second step is, shown in Section A.4, mixing calculated amount of stock solutions for each pH buffer solution.

## A.2 Calculation Principles

The calculations of the pH buffer solutions follow the Henderson–Hasselbalch equation, which describes the derivation of pH. For an acid-base reaction,



then the pH can be determined as the Henderson-Hasselbalch equation,

$$pH = pK_a + \log \left( \frac{[A^-]}{[HA]} \right) , \quad \text{A-2}$$

where the  $pK_a$ , the acid dissociation constant, determines the buffer range. Thus, an important guideline to keep in mind is to make sure the choice buffer has  $pK_a$  range covering the target pH.

## A.3 Stock Solutions Protocols

First step is to make eight 1 M buffer stock solutions. All work and measurements MUST be done at 25 °C in order to be accurate. The recipe is design to make all stock solutions of 1 L in volume, however, it is often not necessary to make that much volume every time. To conserve materials, all of the weights and volumes are can be simultaneously decreased proportionally. The protocols of making the stock solutions are the following:

- a. 1 M Acetic acid
  - i. Add 57.42 mL of glacial (99.7% pure) acetic acid to 1 L volumetric flask.
  - ii. Fill volumetric flask to 1 L with DI water and transfer to labeled storage container.
- b. 1 M Sodium acetate

- i. Add 82.03g of sodium acetate to ~500mL DI water in a 1 L volumetric flask.
  - ii. Fill volumetric flask to 1 L with DI water and transfer to labeled storage container.
- c. 1 M Bis-tris Methane (Will need to purchase I think...CAS# 6976-37-0)
  - i. Add 104.6209g of bis-tris methane to ~200mL DI water in a 500mL volumetric flask
  - ii. Fill volumetric flask to 500 mL with DI water and transfer to labeled storage container.
- d. 1 M HCl
  - i. Add 50 mL of 37%(~10M) HCl to 500 mL volumetric flask.
  - ii. Fill volumetric flask to 500 mL with DI water and transfer to labeled storage container.
- e. 1 M Potassium dihydrogen phosphate
  - i. Add 136.1g of potassium dihydrogen phosphate to ~500 mL of DI water in a 1 L volumetric flask.
  - ii. Fill volumetric flask to 1 L with DI water and transfer to labeled storage container.
- f. 1 M Disodium hydrogen phosphate
  - i. Add 268.07g of disodium hydrogen phosphate ( $\times 7\text{H}_2\text{O}$ ) to ~500 mL of DI water in a 1 L volumetric flask.
  - ii. Fill volumetric flask to 1 L with DI water and transfer to labeled storage container.

g. 1 M Bicine

- i. Add 81.59g Bicine to ~250 mL DI water in a 500 mL volumetric flask.
- ii. Fill volumetric flask to 500 mL with DI water and transfer to labeled storage container.

h. 1 M NaOH

- i. Add 20g of NaOH to ~250 mL DI water in a 500 mL volumetric flask.
- ii. Fill volumetric flask to 500 mL with DI water and transfer to labeled storage container.

Label all stock solution flasks with the solution name, date that was mixed, and person in charge, and set them aside for the next step.

#### **A.4 Buffer Solutions Protocols**

The next step is to mix the stock solutions with calculated amount for each target pH.

The protocols of buffer solutions are the following:

a. 4.5

- i. Add 44.27 mL of 1M sodium acetate to 100 mL volumetric flask
- ii. Slowly add 55.73 mL 1M of acetic acid to fill the 100 mL volumetric flask
- iii. Transfer to labeled storage container.
- iv. Optional: Check pH with pH meter, and adjust with 1 M HCl or 1M NaOH.

b. 5

- i. Add 71.66 mL of 1M sodium acetate to 100 mL volumetric flask

- ii. Slowly add 28.34mL 1M of acetic acid to fill the 100 mL volumetric flask
  - iii. Transfer to labeled storage container.
  - iv. Optional: Check pH with pH meter, and adjust with 1 M HCl or 1M NaOH.
- c. 5.25
- i. Add 81.75 mL of 1M sodium acetate to 100 mL volumetric flask
  - ii. Slowly add 18.25 mL 1M of acetic acid to fill the 100 mL volumetric flask
  - iii. Transfer to labeled storage container.
  - iv. Optional: Check pH with pH meter, and adjust with 1 M HCl or 1M NaOH.
- d. 5.50
- i. Add 88.80 mL of 1M sodium acetate to 100 mL volumetric flask
  - ii. Slowly add 11.20 mL 1M of acetic acid to fill the 100 mL volumetric flask
  - iii. Transfer to labeled storage container.
  - iv. Optional: Check pH with pH meter, and adjust with 1 M HCl or 1M NaOH.
- e. 5.75
- i. Add 88.10 mL of 1M bis-tris to 100 mL volumetric flask
  - ii. Slowly add 11.90 of 1M HCl to fill the 100 mL volumetric flask.
  - iii. Transfer to labeled storage container.

- iv. Optional: Check pH with pH meter, and adjust with 1 M HCl or 1M NaOH.
- f. 6.00
- i. Add 80.70 mL of 1M bis-tris to 100 mL volumetric flask
  - ii. Slowly add 19.30 of 1M HCl to fill the 100 mL volumetric flask.
  - iii. Transfer to labeled storage container.
  - iv. Optional: Check pH with pH meter, and adjust with 1 M HCl or 1M NaOH.
- g. 6.25
- i. Add 70.24 mL of 1M bis-tris to 100 mL volumetric flask
  - ii. Slowly add 29.76 of 1M HCl to fill the 100 mL volumetric flask.
  - iii. Transfer to labeled storage container.
  - iv. Optional: Check pH with pH meter, and adjust with 1 M HCl or 1M NaOH.
- h. 6.5
- i. Add 68.13 mL of 1M potassium dihydrogen phosphate to 100 mL volumetric flask.
  - ii. Add 31.87 mL of 1M disodium hydrogen phosphate to fill the 100 mL volumetric flask.
  - iii. Transfer to labeled storage container.
  - iv. Optional: Check pH with pH meter, and adjust with 1 M HCl or 1M NaOH.
- i. 6.75

- i. Add 57.02 mL of 1M potassium dihydrogen phosphate to 100 mL volumetric flask.
  - ii. Add 42.98 mL of 1M disodium hydrogen phosphate to fill the 100 mL volumetric flask.
  - iii. Transfer to labeled storage container.
  - iv. Optional: Check pH with pH meter, and adjust with 1 M HCl or 1M NaOH.
- j. 7.00
- i. Add 45.43 mL of 1M potassium dihydrogen phosphate to 100 mL volumetric flask.
  - ii. Add 54.57 mL of 1M disodium hydrogen phosphate to fill the 100 mL volumetric flask.
  - iii. Transfer to labeled storage container.
  - iv. Optional: Check pH with pH meter, and adjust with 1 M HCl or 1M NaOH.
- k. 7.25
- i. Add 34.33 mL of 1M potassium dihydrogen phosphate to 100 mL volumetric flask.
  - ii. Add 65.67 mL of 1M disodium hydrogen phosphate to fill the 100 mL volumetric flask.
  - iii. Transfer to labeled storage container.
  - iv. Optional: Check pH with pH meter, and adjust with 1 M HCl or 1M NaOH.

l. 7.50

- i. Add 24.54 mL of 1M potassium dihydrogen phosphate to 100 mL volumetric flask.
- ii. Add 75.46 mL of 1M disodium hydrogen phosphate to fill the 100 mL volumetric flask.
- iii. Transfer to labeled storage container.
- iv. Optional: Check pH with pH meter, and adjust with 1 M HCl or 1M NaOH.

m. 7.75

- i. Add 16.59 mL of 1M potassium dihydrogen phosphate to 100 mL volumetric flask.
- ii. Add 83.41 mL of 1M disodium hydrogen phosphate to fill the 100 mL volumetric flask.
- iii. Transfer to labeled storage container.
- iv. Optional: Check pH with pH meter, and adjust with 1 M HCl or 1M NaOH.

n. 8.00

- i. Add 10.66 mL of 1M potassium dihydrogen phosphate to 100 mL volumetric flask.
- ii. Add 89.34 mL of 1M disodium hydrogen phosphate to fill the 100 mL volumetric flask.
- iii. Transfer to labeled storage container.

- iv. Optional: Check pH with pH meter, and adjust with 1 M HCl or 1M NaOH.
- o. 8.5
  - i. Add 38.51 mL 1M bicine to 100 mL volumetric flask.
  - ii. Slowly add 61.49 mL 1M NaOH to fill the 100 mL volumetric flask.
  - iii. Transfer to labeled storage container.
  - iv. Optional: Check pH with pH meter, and adjust with 1 M HCl or 1M NaOH.
- p. 9.0
  - i. Add 16.61 mL 1M bicine to 100 mL volumetric flask.
  - ii. Slowly add 83.39 mL 1M NaOH to fill the 100 mL volumetric flask.
  - iii. Transfer to labeled storage container.
  - iv. Optional: Check pH with pH meter, and adjust with 1 M HCl or 1M NaOH.

If after the addition of the second ingredient the volume is less than 100 mL, add DI water to adjust the volume to 100 mL. Label all vials with target pH values, date was made, measured pH values (optional), and the person in charge.

# Appendix B

## RADIO FREQUENCY (RF) INTERFERENCE MEASUREMENTS

### B.1 Discovery of the Problem

In 2009, in the improvement process of the lab-developed multi-channel system, System II, a strange phenomenon was observed. During the operation of the system, if the operator was right next to the apparatus, the readings of the signal were only slightly fluctuated for most of the time, but once in a while, large voltage drops randomly appeared on all channels at the same time, as shown in Figure B.1. These sudden voltage drops did not occur with the absence of the operator; yet, reappeared once the operator returned nearby to the apparatus. Also, whenever a phone call or a text message was received on a phone nearby, the same voltage drops appeared. A hypothesis was made that the observed interference was GSM phone signal induced, in other words, the abnormal readings were resulted from RF interference. However, the sampling bandwidth of System II was way under the scope of analyzing power distribution of RF

components in the signal. For the above reasons and out of author's curiosity, a couple of small experiments were carried out to prove the hypothesis.

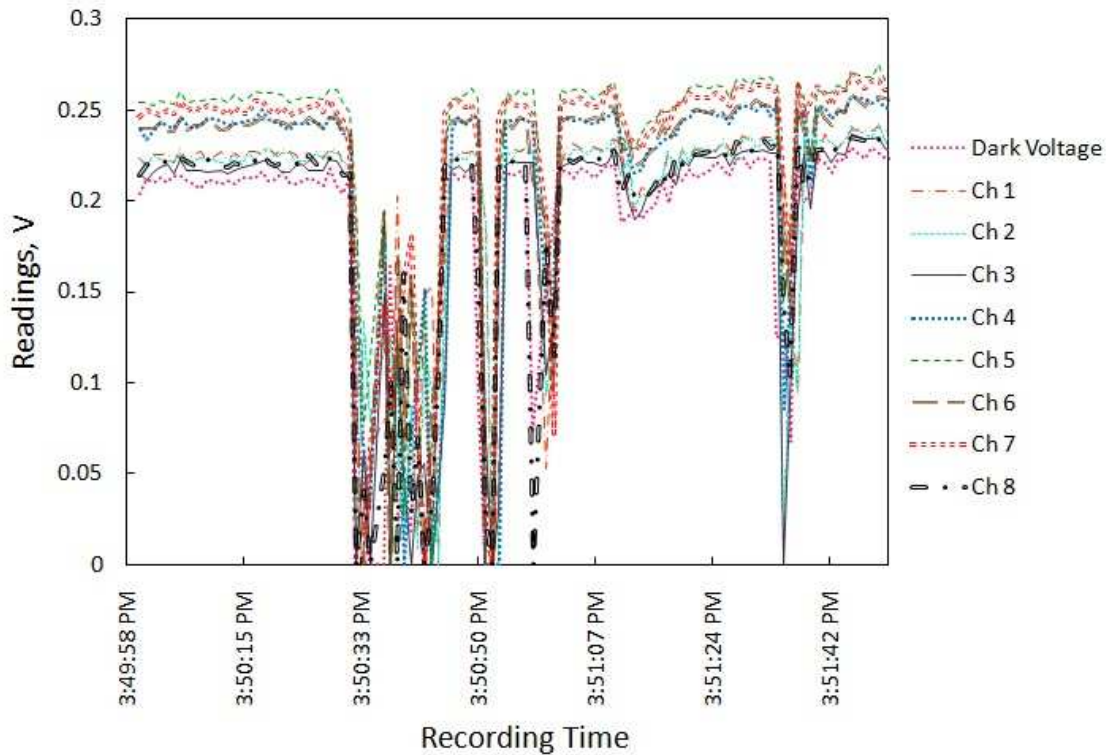


Figure B.1. An example of the readings of random voltage drops for all channels during experiments.

## B.2 RF Interference Measurements

First experiment is to manually turn a GSM phone right next to the apparatus on and off roughly every minute. As seen in Figure B.2, the readings from one of the channels (Channel 7) were dramatically disturbed during the time when the phone was on, and fluctuated much less during the other times when the phone was turned off. Although System II has all electronics contained in two metal housing boxes, as shown in Figure

**B.3**, the connections wires exposed outside the boxes are likely to be the cause of the RF interference. Then a quick fix of an RF-proof box was built as the housing for the entire

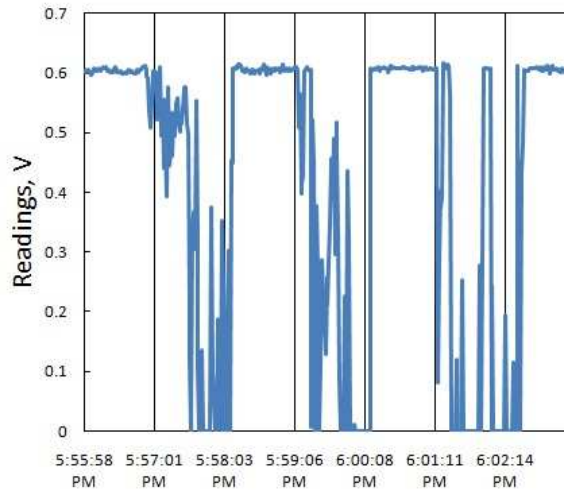


Figure B.2. The readings from Channel 7 of System II with a GSM phone nearby manually turned on and off roughly every minute.

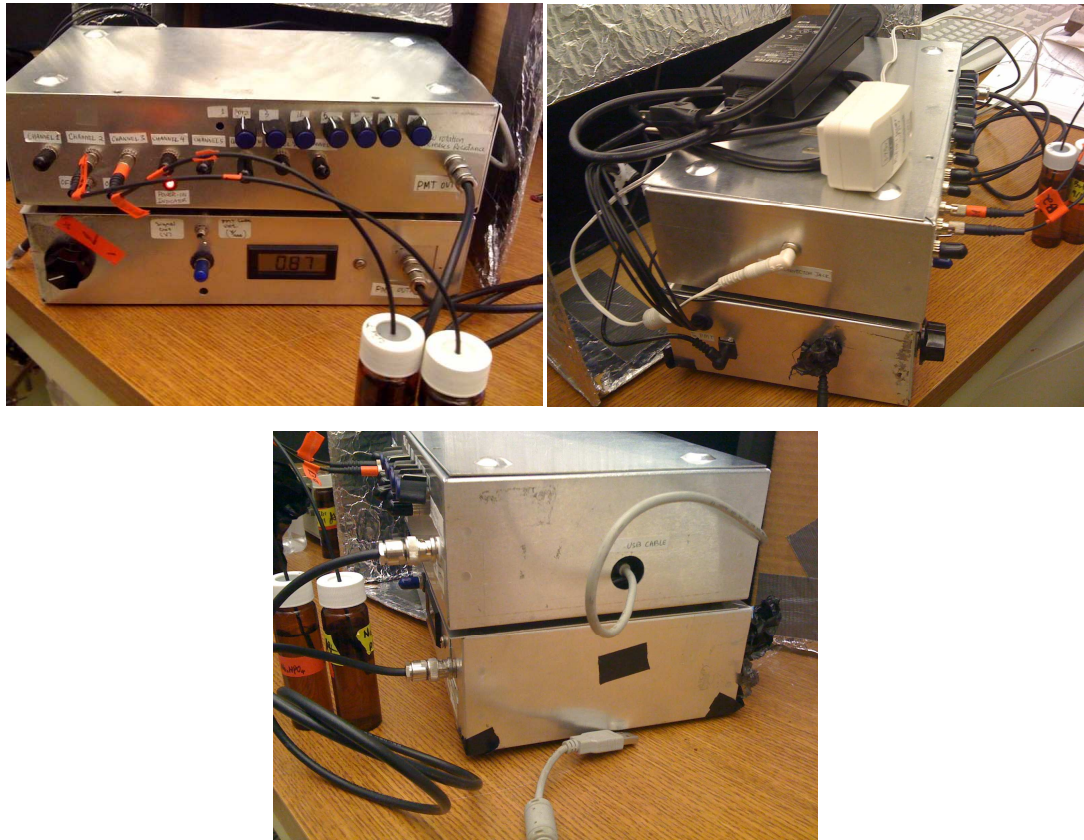


Figure B.3. Front, left side and right side views of System II.

apparatus. The housing is made out of a cardboard box with all sides wrapped in aluminum foil. The results turned out to be surprisingly effective. The same experiment of turning a GSM phone on and off was performed with the apparatus placed inside of the housing. The results of the readings from the same channel are shown in Figure B.4. RF disturbs to the readings were significantly decreased with the new housing installed.

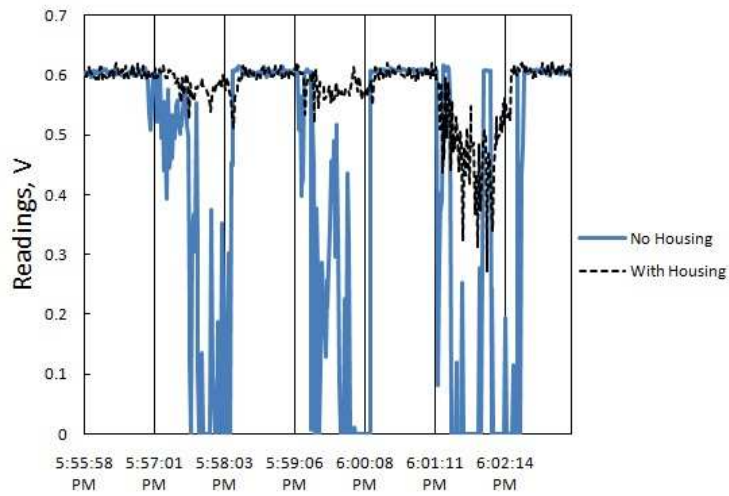


Figure B.4. The readings from Channel 7 of System II with a GSM phone nearby manually turned on and off roughly every minute. Results of the apparatus with no housing is depicted in solid blue line, and the results with the housing is depicted in dashed black line.

Second experiment was to measure the closest distance a GSM phone can be placed near the apparatus. A GSM phone was turned on and off again every minute, and every time it was turned on, the phone was placed at a distance of roughly 0, 1, 2, 5, 10, 15 feet away from the apparatus. The results of the second experiment is shown in Figure B.5. As concluded from the results, as long as a GSM phone is placed farther than 1 foot away from the apparatus with the housing, the RF interference can be avoid. The housing improved the reading standard error from 1.2% to 0.051%.

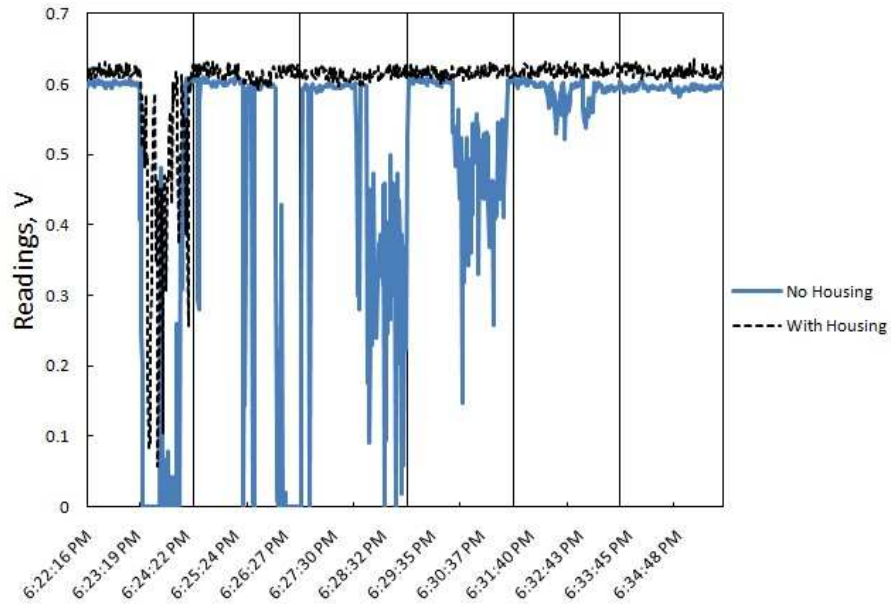


Figure B.5. The readings from Channel 7 of System II with a GSM phone nearby manually turned on and off roughly every minute, and every time when the phone was on, it is placed at a distance of 0, 1, 2, 5, 10, 15 feet away from the apparatus. Results of the apparatus with no housing is depicted in solid blue line, and the results with the housing is depicted in dashed black line.

# Appendix C

## OXYGEN SENSITIVE OPTODES MEASUREMENTS

### C.1 Motivation

Previous work on the characterization of oxygen sensitive optodes have been introduced with complex experimental set up, to simplify the set up and the procedure, a new approach was designed and introduced in this appendix. Originally, a former graduate student at Colorado State University, Sean Pieper, set up the oxygen sensitive tris(4,7-diphenyl-1,10-phenanthroline) ruthenium(II) ( $\text{Ru(dpp)}_3$ ) optode experiments as shown in Figure C.1. It constantly feeds nitrogen gas into the analyte solution to drive out the dissolved oxygen concentration in the analyte. The amount of nitrogen gas is controlled through the nitrogen regulator located on the gas line tube. By blowing different amount of nitrogen into the analyte, different concentration levels of dissolved oxygen can be obtained. The oxygen concentration is measured by a dissolved oxygen meter (EW-01971, Cole-Parmer). The nitrogen gas feed line restricts the experiment to labs.

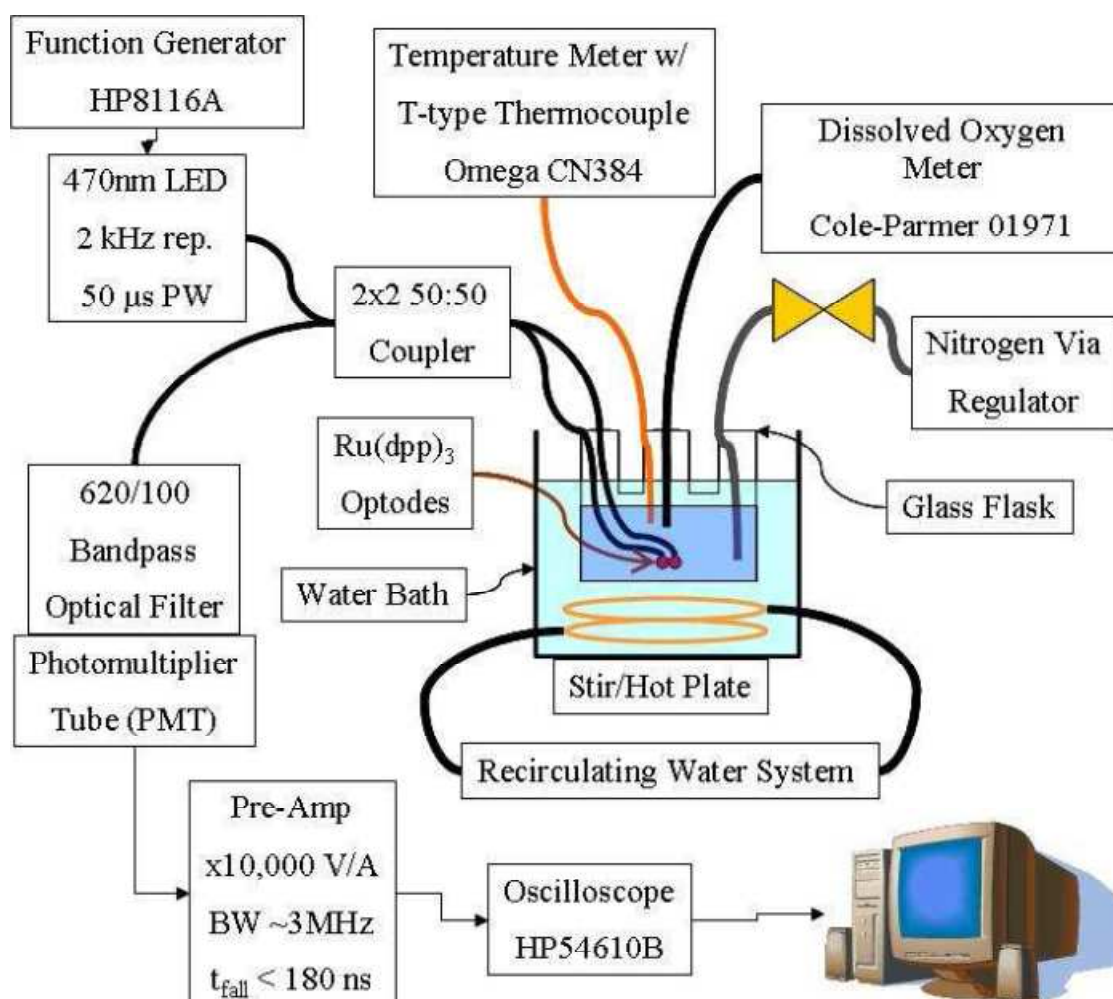


Figure C.1. Experimental set up for a oxygen sensitive Ru(dpp)<sub>3</sub> optode experiments designed by Sean Pieper. This set up uses gas nitrogen to feed into the container where the analyte is to control the dissolved oxygen in the analyte. Reproduced from Reference [1].

## C.2 Principles and Experimental Set-up

The set up uses the reaction between sodium sulfite ( $\text{Na}_2\text{SO}_3$ ) and dissolved oxygen in water to control the dissolved oxygen level. In its reaction, sodium sulfite consumes oxygen produces sodium sulfate with catalyzed by cobalt salt ( $\text{CoCl}_2 \cdot 6\text{H}_2\text{O}$ ), as the following



By adding a known amount of sodium sulfite, the consumption of dissolved oxygen can be calculated, and thus the remaining dissolved oxygen in the solution is known. The experimental set up is implemented with the above principles, as shown in Figure C.2. System that is used in this appendix is System I, but any of the three systems can substitute it. The change to be noticed here is instead of using nitrogen gas, the dissolved oxygen control is through syringing a known amount of sodium sulfite to a fixed volume of water that contains cobalt salt as the catalyst. Analyte is contained in a tinted glass vial with the cap drilled for the optode fiber to go through. The vial is sealed with chemistry wrap to prevent oxygen to escape in or out of the vial. Besides the robust system, the calibration set up is as simple as a vial and a syringe. Although the only disadvantage of the new set up is that the dissolved oxygen concentration can only decrease from the saturated amount to zero and cannot go the other way around.

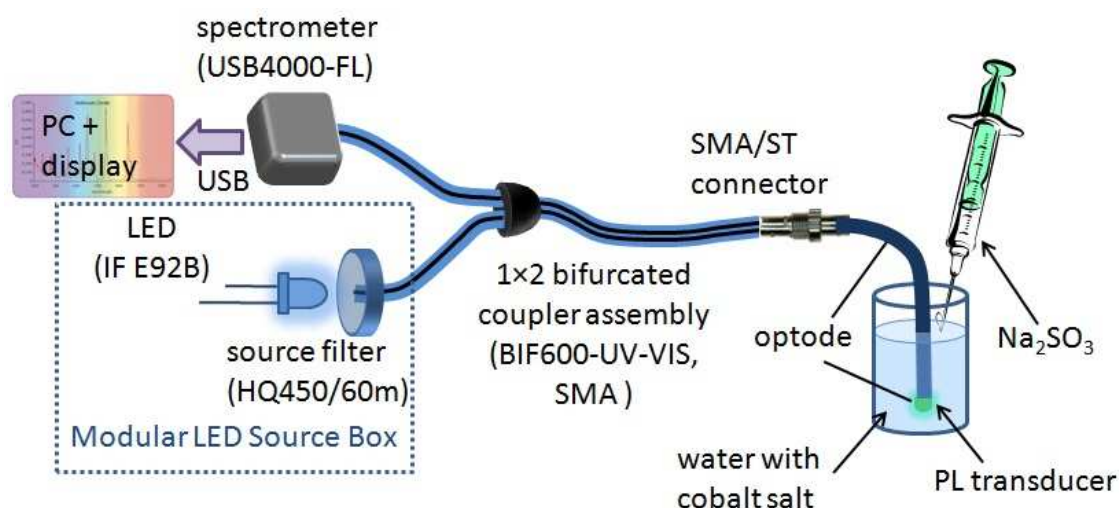


Figure C.2. A new experimental set up for a oxygen sensitive  $\text{Ru}(\text{dpp})_3$  optode experiments. This calibration set up only requires a syringe and a vial for the analyte.

The calculation of dissolved oxygen is shown here using the quantities of chemicals adopted in this appendix as an example. Before adding any sodium sulfite into the cobalt solution, the dissolved oxygen level is assumed to be 8.7 mg/L in room temperature under 1 atm pressure. For 4mL DI water, before any addition of the sodium sulfite, the saturated dissolved oxygen amount in mol is

$$Q_{sat(O_2)} = \frac{V \cdot [O_2]_{sat}}{O_2 \text{ molecular weight}}, \quad \text{C-2}$$

where  $[O_2]_{sat}$  is the saturated dissolved oxygen concentration, which is assumed to be 8.7 mg/L or ppm in room temperature under 1 atm pressure,  $V$  is the analyte volume, which is 4 mL water, and oxygen molecular weight is 32.00 g/mol. The dissolved oxygen  $Q_{sat(O_2)}$  in the analyte at this point is calculated to be 1.088  $\mu\text{mol}$ . Then, 0.4 mL sodium sulfite is stored in a syringe and is divided into small volume of 0.025 mL for each injection. Although the reaction is an easy calculation of 2 mol sodium sulfite consumes 1 mol oxygen, by adding the sodium sulfite solution into the analyte, the 10% volume change is too significant to ignore. Considering the dynamic change in volume, the calculation gets a little bit tricky yet still manageable for an electrical engineering student. The sodium sulfite solution used here has a concentration of 0.6 g/L, and after the first dose of 0.025 mL sodium sulfite added, the saturated dissolved oxygen becomes

$$Q'_{sat(O_2)} = \frac{(V + V_{Na_2SO_3}) \cdot [O_2]_{sat}}{O_2 \text{ molecular weight}}, \quad \text{C-3}$$

where  $V_{Na_2SO_3}$  is 0.025 mL in this case, and the new dissolved oxygen amount  $Q'_{sat(O_2)}$  becomes 1.094  $\mu\text{mol}$ . The amount of added sodium sulfite in 0.025 mL is

$$Q_{Na_2SO_3} = \frac{V_{Na_2SO_3} \cdot [Na_2SO_3]}{Na_2SO_3 \text{ molecular weight}}, \quad C-4$$

where  $Q_{Na_2SO_3}$  has its units in mol and is calculated to be 0.144  $\mu\text{mol}$ ,  $V_{Na_2SO_3}$  is added sodium sulfite volume 0.025 mL,  $[Na_2SO_3]$  is the sodium sulfite concentration, 0.6g/L, and the molecular weight of sodium sulfite is 104.06 g/mol. With 0.144  $\mu\text{mol}$  added, the sodium sulfite consumes half of the amount of oxygen, which is 72.1 nmol. Now subtracting the consumed amount of oxygen from the total saturated dissolved oxygen  $Q'_{sat(O_2)}$  calculated from Eqn. C-3, 1.094  $\mu\text{mol}$ , the remaining oxygen  $Q_{O_2}$  is

$$Q_{O_2} = Q'_{sat(O_2)} - \frac{1}{2} \cdot Q_{Na_2SO_3}, \quad C-1$$

where  $Q_{O_2}$  becomes 1.022  $\mu\text{mol}$ , or 8.13 mg/L, or 254.0  $\mu\text{M}$  for the total volume of 4.025 mL now. The remaining oxygen concentration in the solution is the quencher concentration for the  $\text{Ru}(\text{dpp})_3$  optode.

### C.3 Preliminary Experimental Results

Three  $\text{Ru}(\text{dpp})_3$  optodes were characterized with the above method. Experiments with Optode #1 was performed one week before the experiments with the other two optodes. The phosphorescent readings were integrated over wavelength of 605.01 nm to 625.14 nm. Optode #1 has an integration time of 5 seconds, but Optode #2 and #3 have integration time of 20 ms. The time interval between the two times of the sodium sulfite addition is 1 minute for all experiments. Although the elapsed time for the reaction to reach steady state is the same for all optodes, the number of data points taken by Optode #2 and #3 are much larger than the number of that of the first optode, and thus it results in the standard deviation differences between Optode #1 and the other two optodes. The

phosphorescent intensity readings versus various dissolved oxygen concentrations are shown in Figure C.3 and Figure C.4. A week long storage of Optode #2 and #3 can be the reason for the phosphorescent intensities drop with respect to Optode #1. The sensitivity difference between the three optodes remains when considering either the normalized phosphorescent intensities, shown in Figure C.5, or the Stern-Volmer plots, shown in Figure C.6. Vertical error bars of all figures show the standard deviation of each measurement, and the horizontal error bars show the human error introduced by the manual addition of sodium sulfite solution of 0.01 mL.

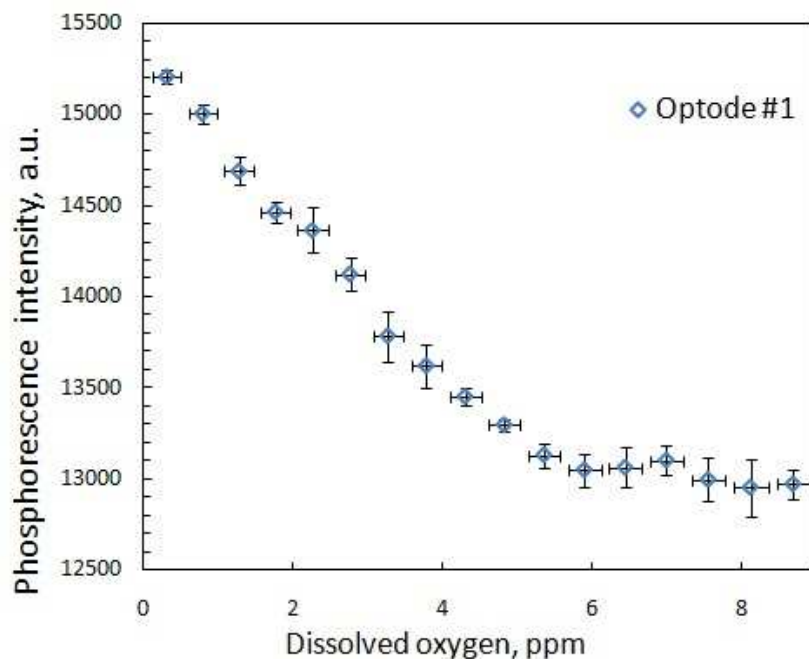


Figure C.3. Phosphorescent intensity of Ru(dpp)<sub>3</sub> Optode #1 with various dissolved oxygen concentrations.

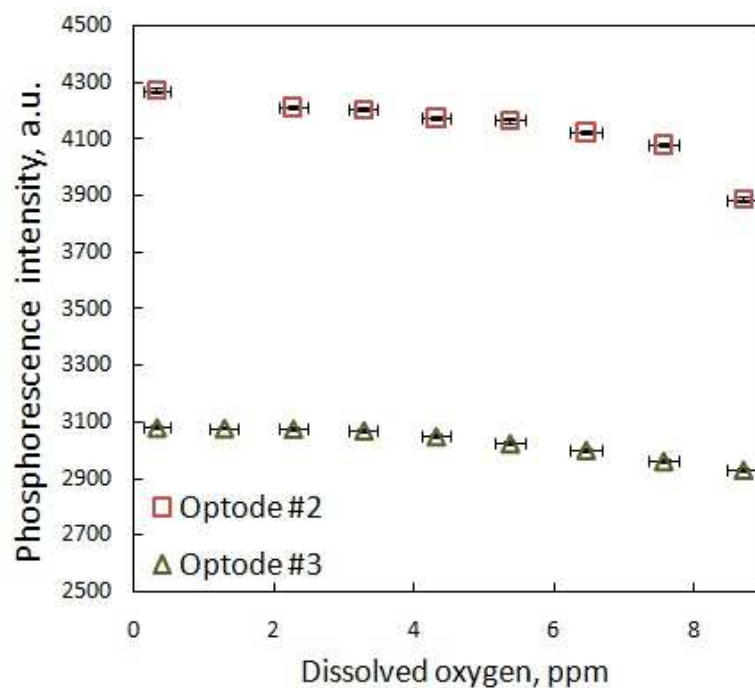


Figure C.4. Phosphorescent intensity of Ru(dpp)<sub>3</sub> Optode #2 and #3 with various dissolved oxygen concentrations.

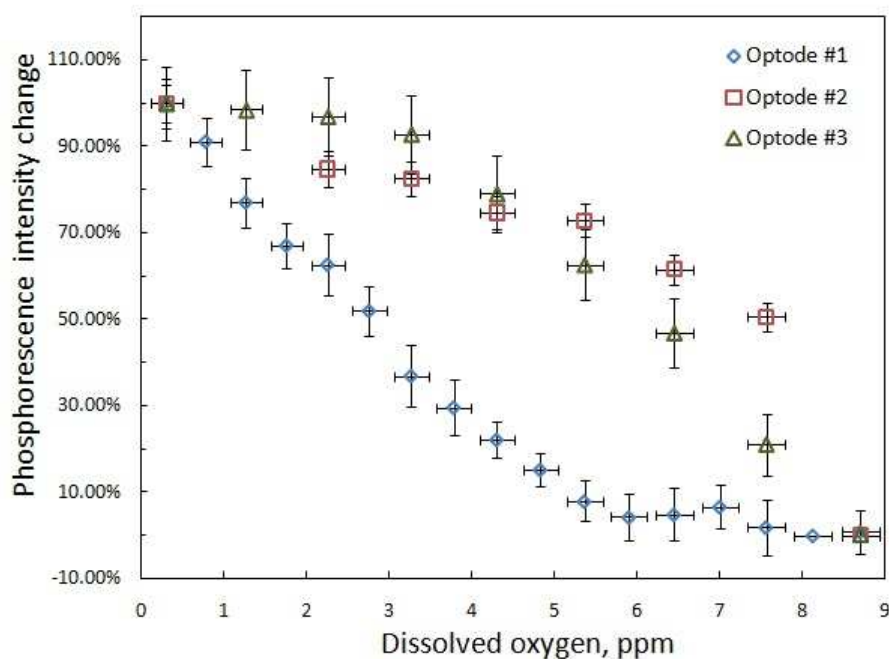


Figure C.5. Stern-Volmer plots of the phosphorescent intensities of Ru(dpp)<sub>3</sub> Optodes.

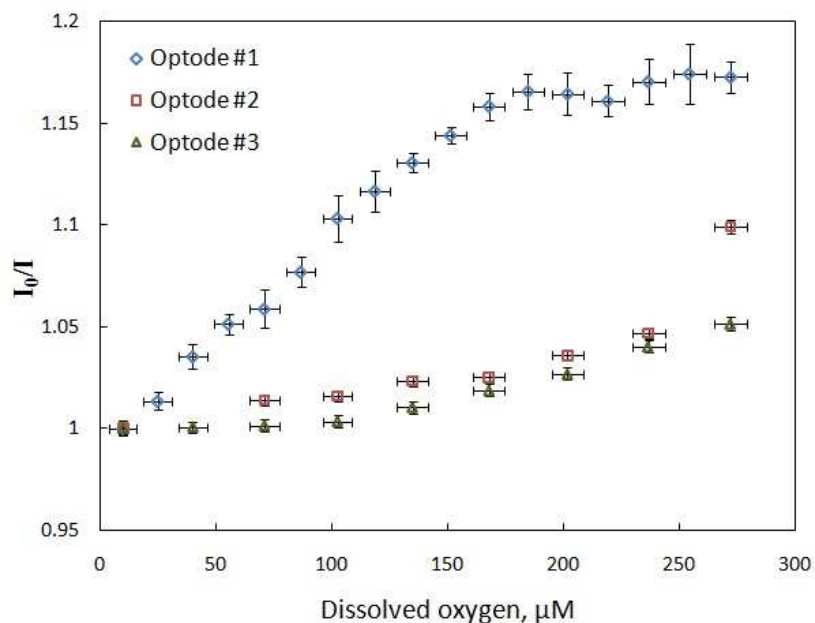


Figure C.6. Stern-Volmer plots of the phosphorescent intensities of Ru(dpp)<sub>3</sub> Optodes.

#### C.4 Notes on Future Works

This appendix is to introduce a simpler experimental set up for the oxygen sensitive optodes characterization with an example experimental results; however, the example experiments have plenty of space for improvements. First, the a dissolved oxygen meter and a thermometer can be incorporated into the set up. Because Ru(dpp)<sub>3</sub> has a strong dependency on temperature [1], monitoring the temperature change during the experiments would be useful. Second, measurements with multiple optodes are preferred to be done within a short period of time. A variety of factors during the storage of the optodes can alter the dye molecules characteristics, one of the known factors is photobleaching. Shortening the experiments time span does not avoid the optodes degradation but eliminate some possible varying parameters that may cause the variation between optodes.

## C.5 References

- [1] Sean B. Pieper, "Temperature Dependence of Oxygen Sensitive Transducer," in *Optical Characterization of Phosphorescent Dyes for Biosensor Transducer Applications*. Fort Collins, United States: Colorado State University, 2008, ch. 6, pp. 100-124.

# Appendix D

## BACK REFLECTION WITH INDEX MATCHING MEASUREMENTS

### D.1 Motivation

Chapter 4 of this thesis has introduced the factor of back reflection that causes the nonlinearity in Stern-Volmer equation, and Chapter 5 has given results of index matching materials' impact on reducing the back reflection intensity for two kinds of fiber coupler assemblies. To tie the two aspects of the problem together, this appendix shows some preliminary results on how reducing back reflection intensity affects the parameters in Stern-Volmer equation. Theoretically, with a reduction in back reflection influence, the absolute fluorescent intensities decreases for all cases; yet with the reduction only in noise intensities, the relative change in fluorescent intensities with various quencher concentrations increases, and thus the sensitivity of the system increases. Also, by controlling the back reflection intensity, the results can gain us more knowledge about the non-linearity effects in the Stern-Volmer equation.

## D.2 Experimental Set-up

Experiments were set up very similarly to the characterization experiments from Chapter 4 except for few variations. A block diagram of the experimental set up with System III is shown in Figure D.1. All measurements were done with the same pH sensitive FLA optode on Channel 1 to eliminate uncontrollable variables, and all the other channels were capped to block ambient light. Index matching material is the controlling variable in this experiment. When the index matching material is air, that means the end of the fiber splitter is exposed in the air inside of a black container to block ambient light; when the index matching material is water, it means the end of the fiber splitter exposed in the water inside of the same container.

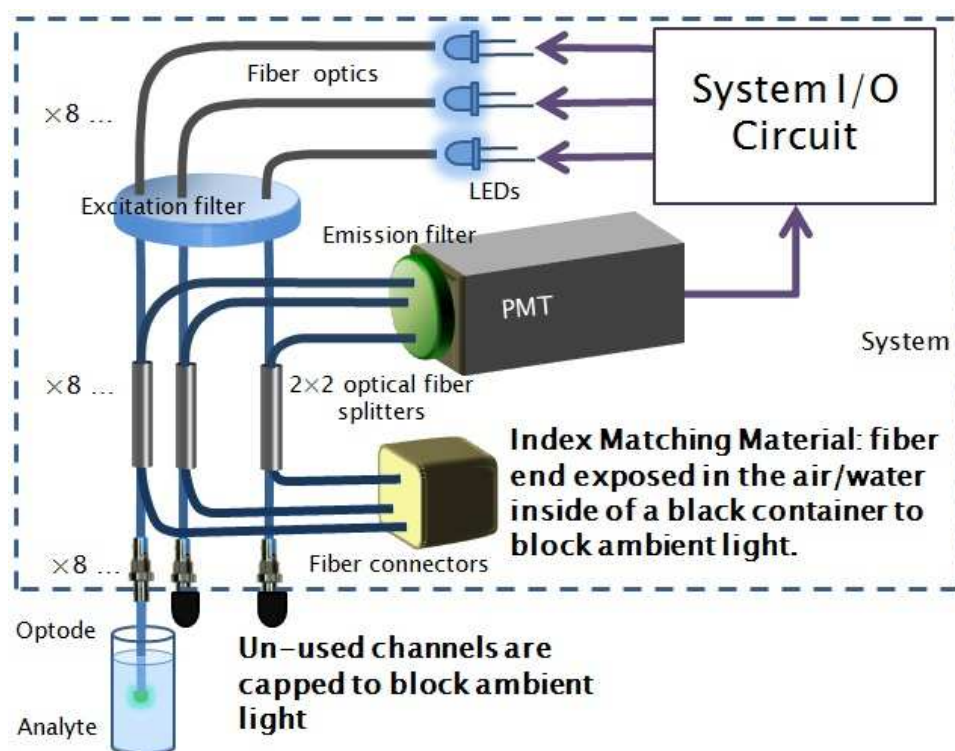


Figure D.1. Experimental set up to verify the back reflection effects on the Stern-Volmer response using System III.

### D.3 Preliminary Experimental Results

Results show that the varying in the index matching material has a significant effect on the response. The fluorescent intensities with the two index matching materials with varying  $H^+$  concentrations are shown in Figure D.2. Assuming the fluorescent intensity when the  $H^+$  concentration is very small, 3.16 nM, is the unquenched intensity,  $I_0$ , the Stern-Volmer plots with different index matching materials are shown in Figure D.3. The dotted lines in Figure D.3 are the models of the modified Stern-Volmer equation described as

$$\frac{I_0'}{I'} = \frac{\frac{1}{f} \cdot (I_{BR}/I_0 + 1)}{1 + K_{SV} \cdot [Q] + \frac{1}{f} \cdot (I_{BR}/I_0 + 1) - 1}, \quad D-1$$

where  $I_0'$  and  $I'$  are the measured fluorescent intensities that are affected by the fractional inaccessibility of the fluorophore with the accessible fraction of  $f$  and the back reflection with intensity of  $I_{BR}$ , and  $I_0$  is the ideal unquenched fluorescent intensity. The modified Stern-Volmer model, as show in Eqn. D-1, provides the best-fit parameter values of  $K_{SV}$  and  $\frac{1}{f} \cdot (I_{BR}/I_0 + 1)$  with for the minimum root mean squared error (RMSE) as shown in Table D.1. For convenience purpose, the parameter  $\frac{1}{f} \cdot (I_{BR}/I_0 + 1)$  is defined as the Stern-Volmer non-linear (SVNL) parameter. As mentioned in the previous section, all measurements were done with the same optode on the same channel. Therefore, theoretically, the fluorophore-only-related parameters  $K_{SV}$  and  $f$  are consistent between the two sets of index-matching-material measurements; in other words, the only difference between the two sets of measurements should be from  $I_{BR}/I_0$ . A second fitting method is adopted with the same calculation method as the minimum RMSE

method except for that the  $K_{SV}$  parameter is fixed at 2.5, and the results are shown in

Table D.1.

Table D.1. Fitting Parameters Of The Modified Stern-Volmer Model

Index Matching Material	Fitting Method	$K_{SV}$	$K_{SV}$ 95% Confidence Interval	SVNL, $\frac{1}{f} \cdot (I_{BR}/I_0 + 1)$	SVNL 95% Confidence Interval	$R^2$
Air	Minimum RMSE	2.059	(0.9365, 3.181)	1.76	(1.695, 1.825)	0.9704
	Fixed $K_{SV}$	2.5 (fixed)	N/A	1.771	(1.692, 1.85)	0.9691
Water	Minimum RMSE	2.977	(1.743, 4.211)	1.461	(1.431, 1.49)	0.983
	Fixed $K_{SV}$	2.5 (fixed)	N/A	1.455	(1.418, 1.491)	0.9817

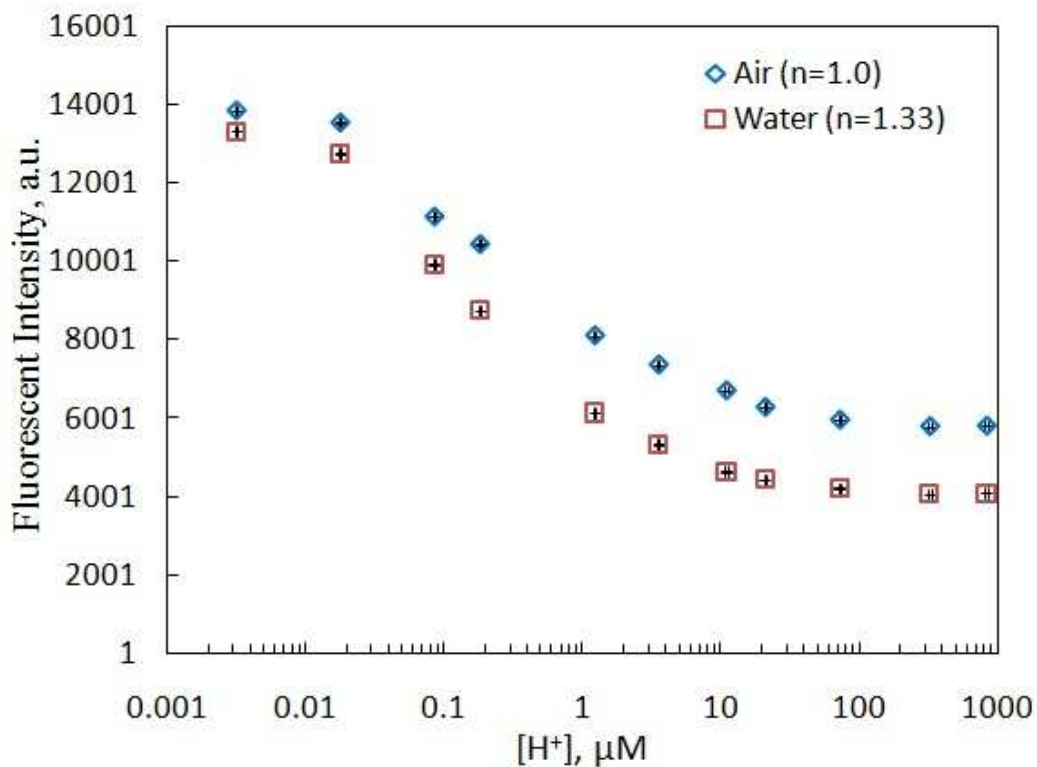


Figure D.2. Results of the fluorescent intensities versus varying  $H^+$  concentrations with the index matching material being air (blue diamond) and water (red square).

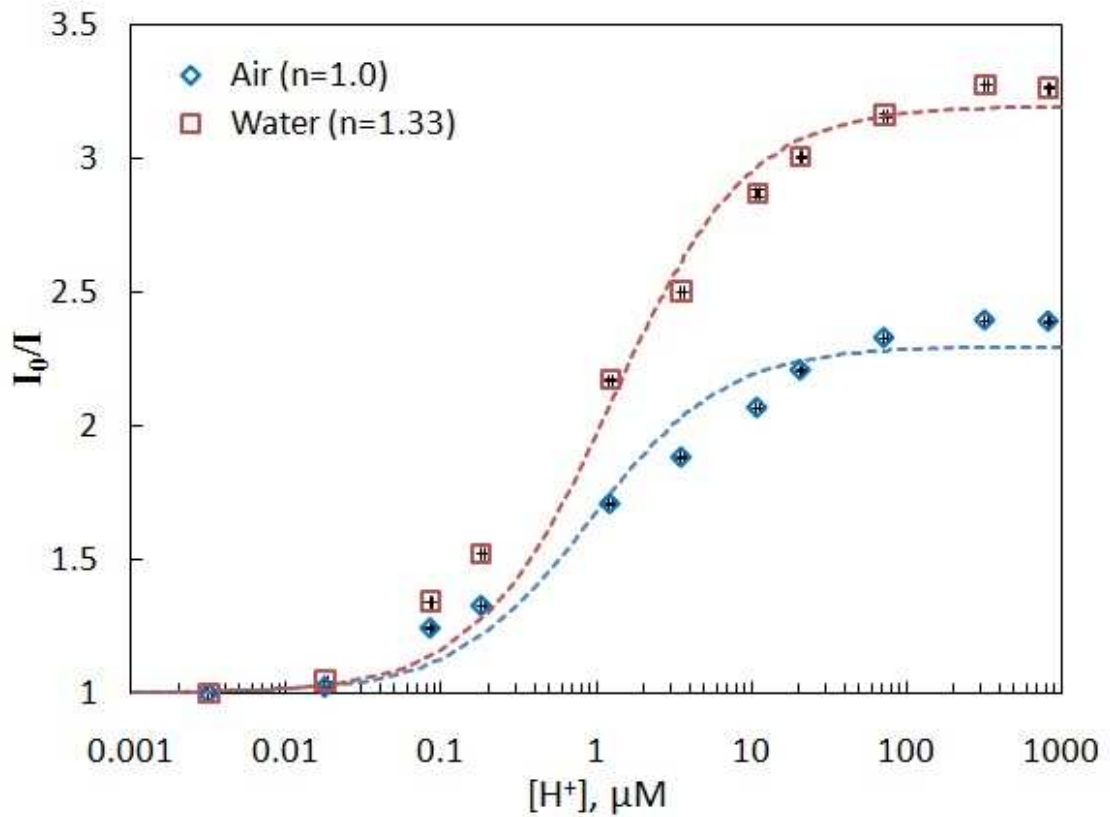


Figure D.3. Results of the Stern-Volmer plots with the index matching material being air (blue diamond) and water (red square). The dotted lines are the non-linear model modified from the Stern-Volmer model.

Although some of the results turned out differently than expected, the results are still valid for discussion and future improvements. Few observations are worth attention. The intensity difference between the absolute fluorescent intensities for the two kinds of index matching materials is not a constant throughout the measurements, in other words, a correlation is observed between the reduced back reflection intensity and the absolute fluorescent readings, as shown in Figure D.4. In theory, the reduction of the back reflection from the index matching is constant with a relationship to the incident optical power defined by the Fresnel equation

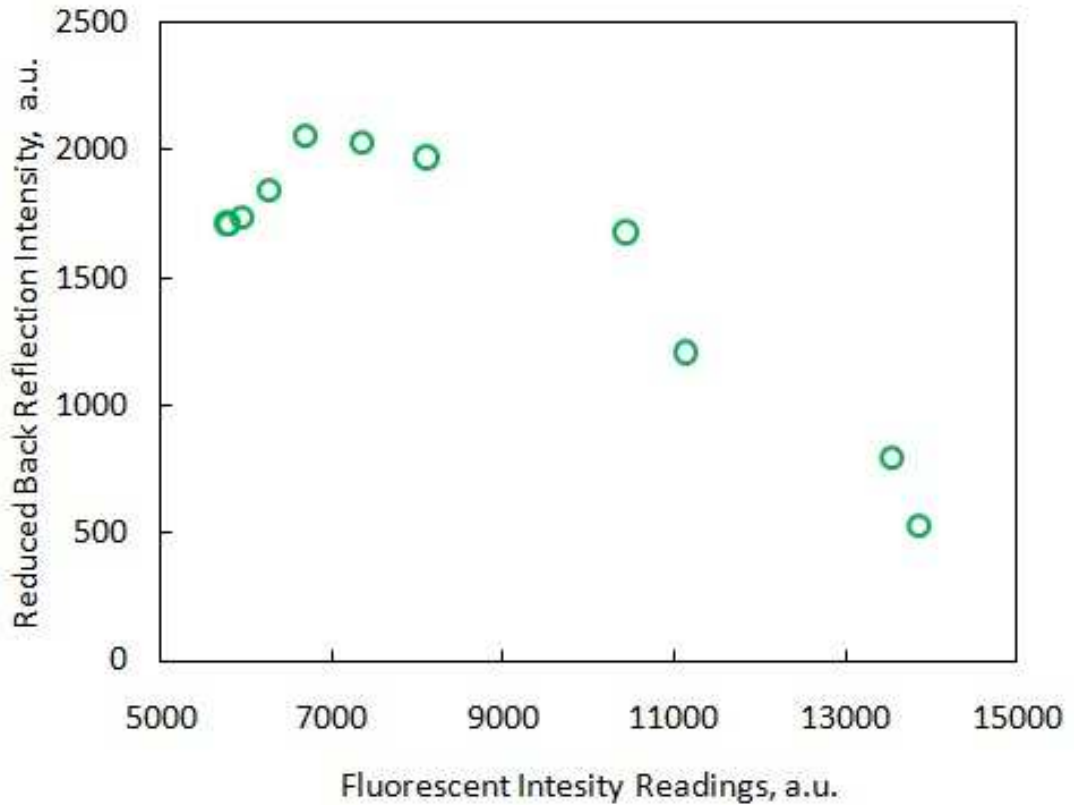


Figure D.4. A plot of the reduced back reflection intensities versus the absolute fluorescent intensity readings (for index matching material is air).

$$\frac{P_{BR.}}{P_{Inc.}} = \left( \frac{n_f - n_i}{n_f + n_i} \right)^2, \quad \text{D-2}$$

where  $P_{Inc.}$  and  $P_{BR.}$  are the incident and the reflected optical powers at the interface of refractive indices mismatch respectively,  $n_f$  and  $n_i$  are the refractive indices of the incident material, fiber core, and the other side of the interface, the index matching material. Therefore, as long as the incident optical power does not change, the same index matching material should results in the same reflected optical power, but this does not agree with the experimental results. One possible explanation is, the illumination source power stayed constant for all measurements, which means the incident optical

power at the indices mismatch interface,  $P_{Inc.}$ , is the same for all measurements. As the reflected optical  $P_{BR.}$  changes as  $n_i$  changes for air ( $n_i = 1.0$ ) and water ( $n_i = 1.33$ ), the transmitted power  $P_{trans.}$  varies accordingly, because

$$P_{trans} = P_{Inc.} - P_{BR.} \quad \text{D-3}$$

In the case of our applications,  $P_{trans.}$  is the excitation light of the fluorophore, and the variations in the excitation light power may change the response of the fluorophore in terms of with different quencher concentrations. In this sense, the experiments in this appendix are not well controlled.

# Appendix E

## SYSTEM II DOCUMENTS

### E.1 Introduction

System II is the lab developed multichannel PL-based fiber optic system designed, assembled, and altered by many former students at Colorado State University. The earliest documentation on this system is the senior design reports of spring 2004 by Jonathon Jaeger and fall 2005 by Evan Gartner. Presumably the photodetector circuit assembled by the senior design students was preserved. After that, former Master students Sean B. Pieper and Manasi Katragadda further evolved the system from single channel into a multichannel system. Although the multichannel system has a commercial prototype version, System III, that functions more advanced, System II is still valuable for research purposes with the great advantage of simplicity in software alteration. This appendix includes all System II related documents for the convenience of future modification and references. All documents are only a snapshot of the current set up as of August 2011. For any of the earlier documentations on this system, please refer to Sean B. Pieper's Master thesis.

## E.2 Electronic Schematics

A schematic drawing of the System II electronics is shown in Figure E.1.

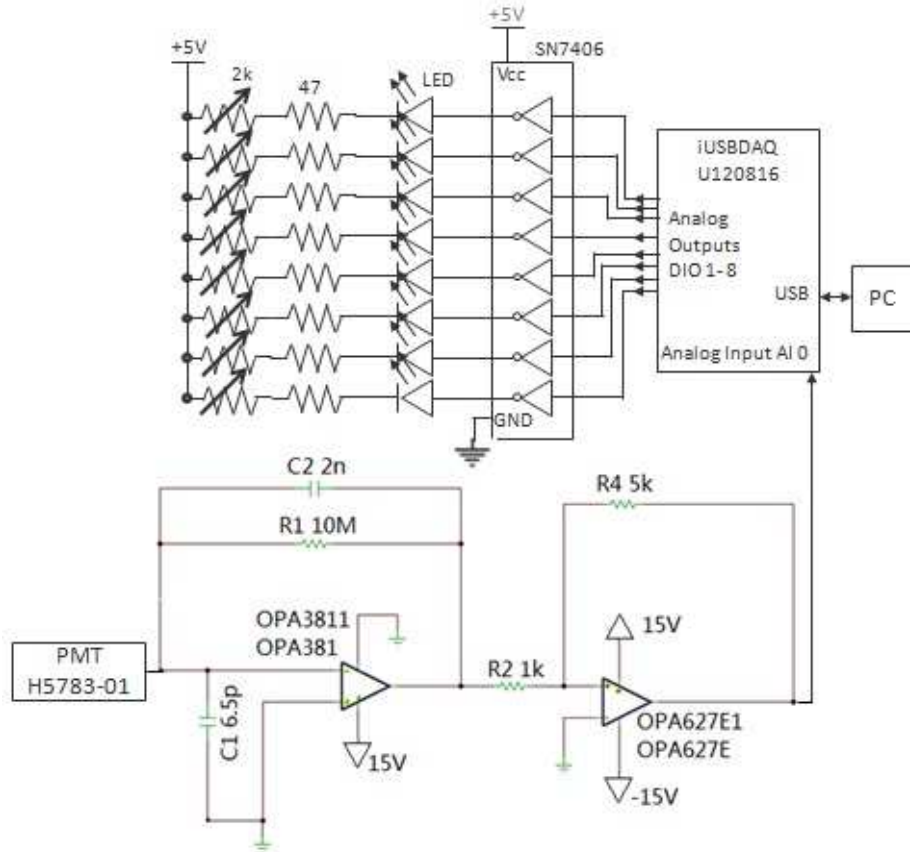


Figure E.1. A electronics block diagram of System II.

## E.3 Bill Of Materials

System II is comprised with two modules, a source module and a photodetector module. The Bill of Materials of both modules are shown in Table E.1 and Table E.2.

Unit price with a \* represents an estimation of the unit cost.

Table E.1. Bill of Materials of the Source Module of System II

Item	Manufacturer	Part Number	Quantity	Unit Price
2 × 2 fiber couplers (3 couplers with bare ends and only one output end with ST-connector)	Industrial fiber optics	IF-540 custom order	8	\$65.00
Plastic fiber optic 470 nm blue LED	Industrial fiber optics	IF E92B	8	\$8.58
Bare Plastic Optical Fiber, 1mm fiber diameter, step-index profile, Core Refractive Index 1.49, Numerical Aperture 0.5	Industrial fiber optics	IF C U1000	1	\$6.00
1m ST-ST fiber patchcords	Industrial fiber optics	IF-640-1-0	4	\$16.70
450/60 bandpass normally incident optical filter	Chroma technologies	HQ 450/60 m OS02295	1	\$50.00*
Filter holder			1	\$200
ST female-ST female adapter	Allied electronics	512-6506	8	\$1.55
Enclosure, Al - .04 in. thick, 12 in.×7in. ×3 in.	Allied electronics	AC-408	1	\$21.70
Plate, bottom, Al, .04 in. thick, 11.812 in. ×6.812 in., natural	Allied electronics	736-1595	1	\$7.07
Self-adhesive rubber feet, .5 in × .5 in× .22 in	Allied electronics	736-3581	4	\$0.43
5 mm Fresnel Lens LED Panel Mount Indicator, Red (635 nm) peak wavelength	Allied electronics	670-1321	1	\$1.21
Toggle switch, mount, round, SPDT, On-none-on, rated 5 A @120 V AC OR 28 V DC	Allied electronics	676-3000	1	\$3.10
2 kohm, 15-turn trimmer Potentiometer0.5 Watts, Rectangular package, 0.748" L x 0.185" W x 0.252" H (19.00mm x 4.7mm x 6.40mm)	Digi-key	SP043-2.0K-ND	8	\$1.42

<b>Item</b>	<b>Manufacturer</b>	<b>Part Number</b>	<b>Quantity</b>	<b>Unit Price</b>
Eurostyle Terminal Strip, connector terminal, 5 position, 8 mm	Digikey	WM15903-ND	1	\$2.64
IC socket, DIP 14, through hole mounting type, pitch .1"(2.54mm), 0.3" (7.62 mm) row spacing, closed frame, contact finish-- tin, undefined	Digikey	A24808-ND	2	\$0.60
Standoffs-	Digikey	2210K-ND	8	\$0.403
Prototype Boards - Perforated, ...	Digikey	V1042-ND	1	\$8.10
Power adapter, AC to DC, Universal, digital camera, selectable 3,5,6,6.5,7 or 7.5 V output, rating upto 2A	Radio shack	273-1696	1	\$32.99
47 kohm resistors	Radio shack	2711342	8	\$0.20
Screws- 6-32 Round-Head Machine Screws (assortment of 1/4", 1/2", 3/4")	Radio shack	64-3012	1	\$1.99
High-tech silver bearing solder, 0.015" diameter, 1 oz	Radio shack	64-03E	1	\$3.49
DC power jack, Size M, Coaxial, solder lug	Radio shack	274-1563	1	\$2.99
Hook-up wire, 18 gauge, 1/64" PVC, 13.7 m	Radio shack	278-1223	1	\$5.49

Table E.2. Bill of Materials of the Source Module of System II

<b>Item</b>	<b>Manufacturer</b>	<b>Part Number</b>	<b>Quantity</b>	<b>Unit Price</b>
Photomultiplier Tube (PMT)	Hamamatsu	H5783-01	1	\$1,000.00*
Shutter Block	Hamamatsu	A10036	1	\$300.00*
Fiber stand			1	\$50.00*
Coaxial cable			1	\$5.00*
500hm Coaxial cable	Belden	8262	15"	\$5.00
520/20 bandpass filter	Chroma Technologies	D520/20m	1	\$150.00

<b>Item</b>	<b>Manufacturer</b>	<b>Part Number</b>	<b>Quantity</b>	<b>Unit Price</b>
Op-Amp	Fairchild Semiconductor	LM741CN	2	\$0.39
LCD Display Screen	C-TON Industries	DK543	1	\$39.80
Connector terminal	Molex connector	WM15903	1	\$2.82
Miniature 2 Pole Power Rocker Switch	C&K Components	DM64J72S205Q3	1	\$6.34
2×2 fiber splitter (1 ST, 3 bare ends)	Industrial Fiber Optics	IF-540 custom order	1	\$65.00
ST-ST mating sleeve	Industrial Fiber Optics	IF-820063	1	\$1.55
Toggle switch	Allied Electronics	676-3000	1	\$3.10
trimmers	Bourns	3266-W-1-502	2	\$2.94
Aluminum enclosure	Bud Industries	AC-408	1	\$21.20
Aluminum bottom plate	Bud Industries	736-1595	1	\$6.90
Rubber foot	Bud Industries	736-3581	4	\$0.40

#### **E.4 User's Manual**

The measurements with System II should set up as shown in Figure E.2 and Figure E.3. Operational details of the program and DAQ are provided here as future guidelines. To install the iUSBDAQ U120816, the drivers and manufacturer software need to be downloaded from hytek automation's website. It is always necessary to make sure the

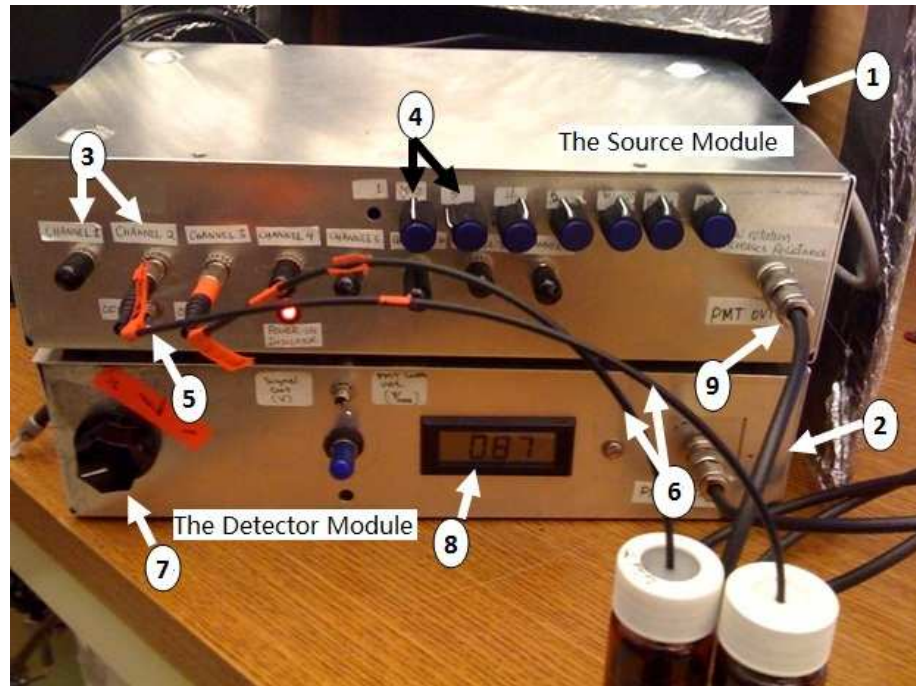


Figure E.2. A front view of System II. In the picture: 1. the Source Module: in which contains the optical excitation circuitry and USB data acquisition module (iUSBDAQ U120816); 2. the Detector Module: in which contains the luminescence detecting circuitry and signal amplifying circuitry; 3.Channels (interface on the front panel); 4. excitation power adjust knobs (corresponding to each channel): counterclockwise rotation increases resistance, which decreases output optical power; 5. On/Off switch of the Source Module; 6. optodes; 7. gain control knob: counterclockwise rotation increases signal amplification goes from 0 to 0.87; 8. gain control display; 9. co-ex cable.

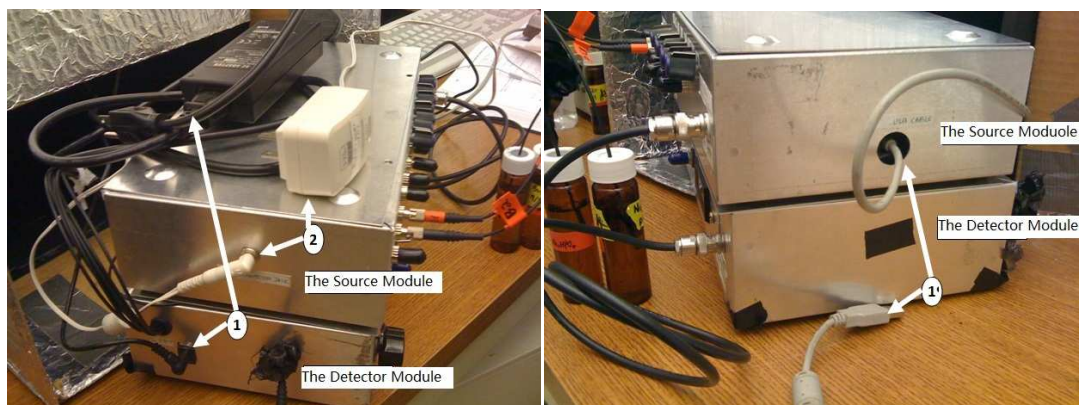


Figure E.3. Side views of System II. In the left picture: 1. power supply for the Source Module: 5VDC; 2. power supply for the Detector Module: 12VDC. In the left picture: 1. USB cable.

Hytek USB cable is always plugged into the same USB port that was selected while installing the software. Otherwise, the unit will not be able to detect the installed software later on. For operating LabVIEW, installing version 8.2 or above is required. Specifically, since the original VIs (virtual instruments) provided by Hytek were specifically written for versions 8.2 or above, any lower version of LabVIEW is not compatible with these VIs. All the digital I/O communication VIs are collected in a library file provided by Hytek automation, and can be downloaded from the website (<http://www.hytekautomation.com/iDAQDownload.html>). After the proper software installation, operate the multi-channel sensor VI, and an interface shown as in Figure E.4 will display. Make sure the USB cable is connected to the Hytek, otherwise an error

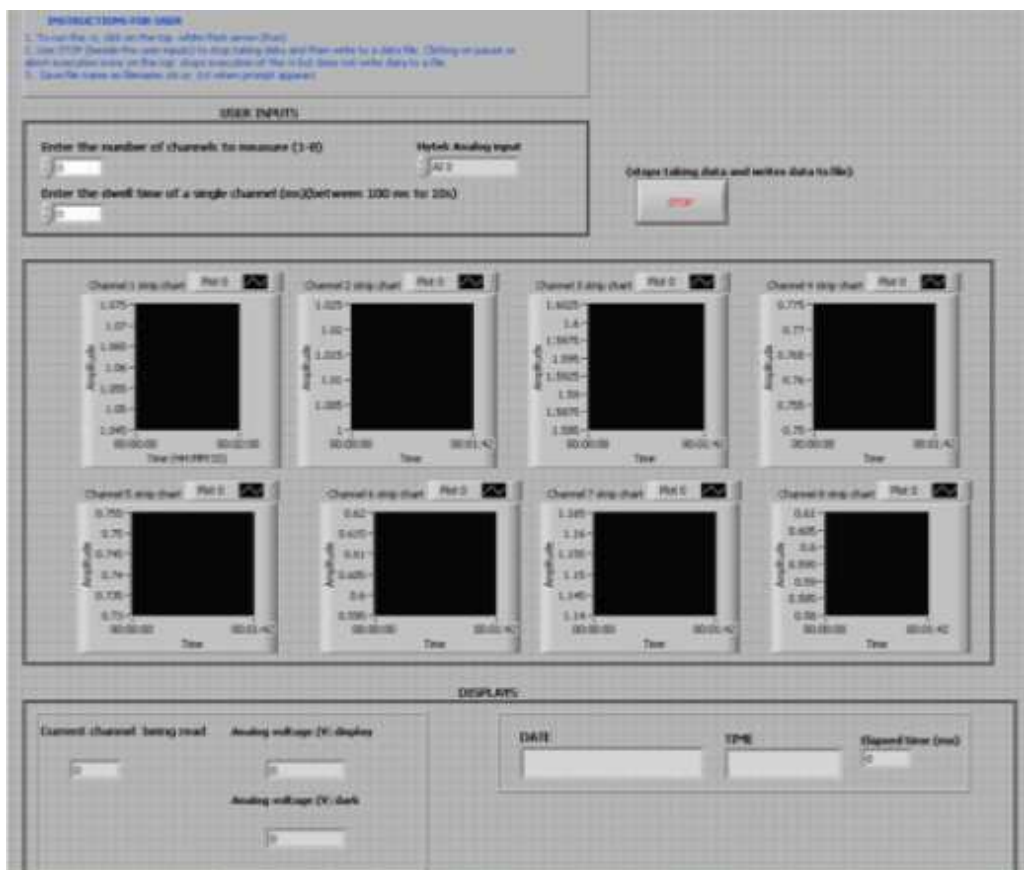


Figure E.4. A screenshot of the user LabVIEW interface for System II measurements.

message of “device index exceeds the max dimension number of that type” appears.

After opening the VI file, it will prompt a warning, as shown in , and click "OK". Once the "run" button of the LabVIEW VI is pressed, the system starts recording data from the PMT. To abort the operation without saving the recordings, press the "abort" button of LabVIEW. Otherwise, once the VI is stopped by pressing the "STOP" button on the user interface, a prompt will appear to ask user to save the data into a XML file.

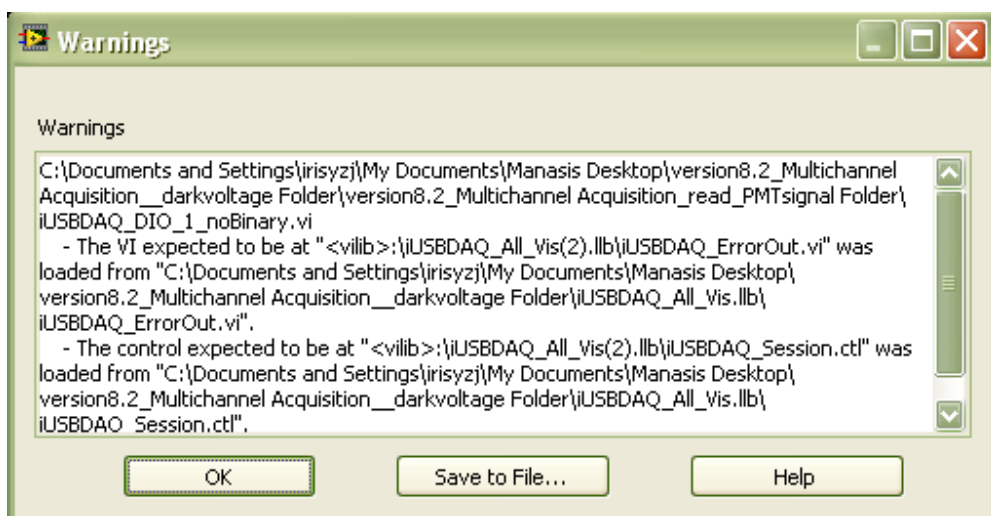


Figure E.5. A screenshot of the warning message appeared when starting the LabVIEW program for System II measurements.

A typical experiments procedures are the following:

1. Plug in both power supplies, and turn on the switches for both boxes.
2. Open VI file as following the steps shown above.
3. Warm up the instrument for 20-30 minutes, or until the “Analog voltage(V) dark” indicates voltage readings higher than zero.
4. Calibrate the instrument.
5. Precede experiments.

6. Save file and exit.

Some advices and tips of operating the experiments are offered here:

1. Turn on and run the system at least 20 minutes prior to performing the experiments for stability.
2. Clean the ST connectors of the optodes with methanol drenched Kimwipe tissues on the optodes before any experiments.
3. Detach the ST connecterized fibers from the inside of the front panel of the Source Module, clean the ST connectors of the fibers as well as the ST connector mating sleeves mounted on the front panel. Insufficient cleaning of the fiber tips can cause significant variations.
4. For a set of experiments with the purpose of comparison, leave the optodes connected to the front panel as much as possible. The connect/disconnect motions of the ST connectors could cause over 10% of the variations in the experiment results. Refer to Appendix G for ST connector related problems analysis and cleaning procedures.
5. Clean optodes' sensor end with distilled water every time when changing analytes.
6. Keep both the instrument and the analyte in dark places while performing the experiments.
  7. Keep any devices that could generate significant radio frequency signals in at least distance of 10 feet. Keeping the instrument in the insulation box during the experiments is recommended.

# Appendix F

## SYSTEM III DOCUMENTS

### F.1 Introduction

System III is the commercial prototype version of the multi-channel PL-based enzymatic biosensor system. It was designed based upon the lab developed multi-channel PL-based enzymatic biosensor system, System II, in 2010 by Chad Busse from OptiEnz Sensors LLC. The system has two models, one is designed for pH sensitive optodes and the other one is for oxygen sensitive optodes. Two models are essentially exactly the same in terms of electronics and software, and the only difference is the emission optical filters in the two have different spectral passband. This appendix provides System III related documents for the purpose of future references. Documents include electronic system diagram, electronic schematic drawings, bill of materials, and user's manual.



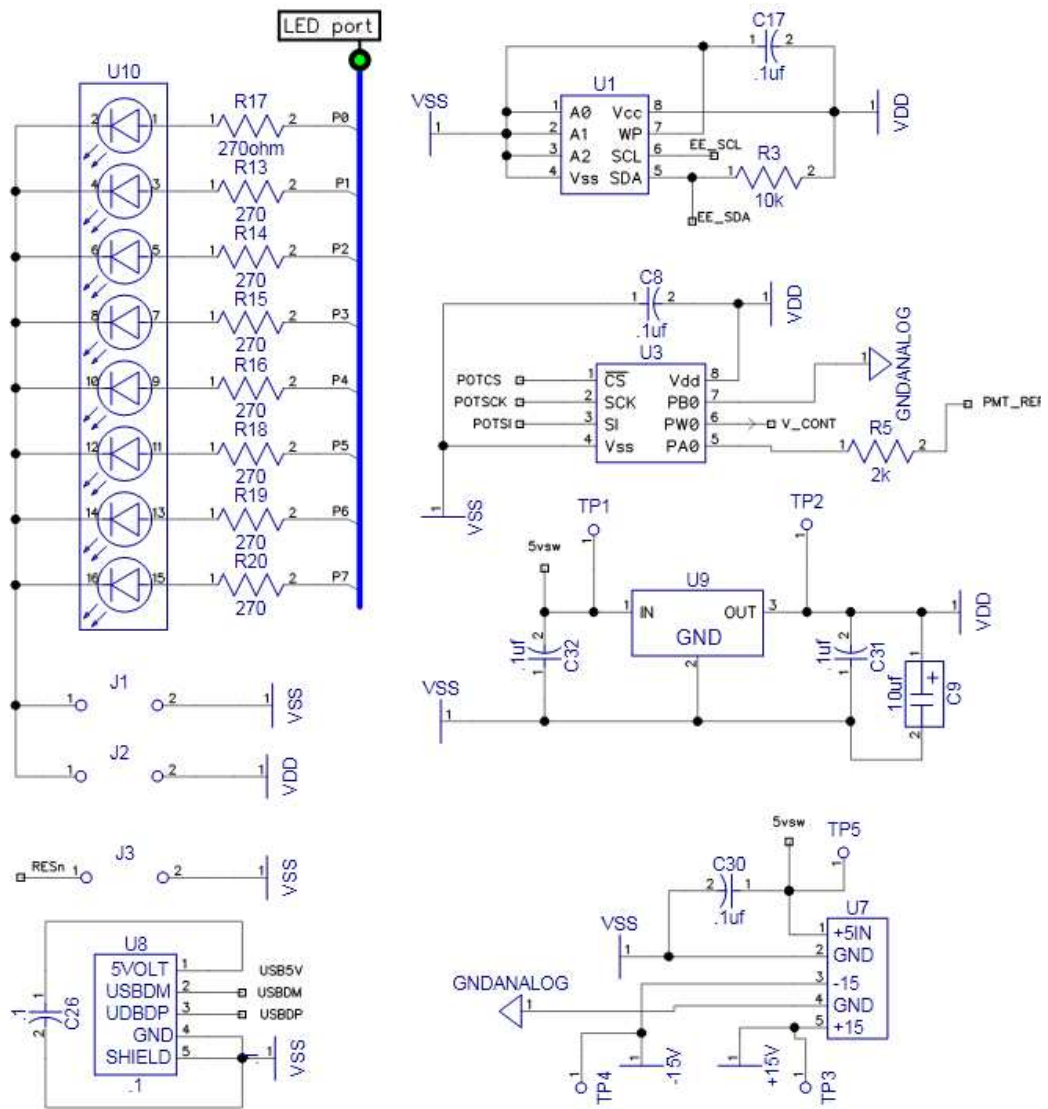


Figure F.3. A schematic drawing (Part 2) of the electronics of System III.

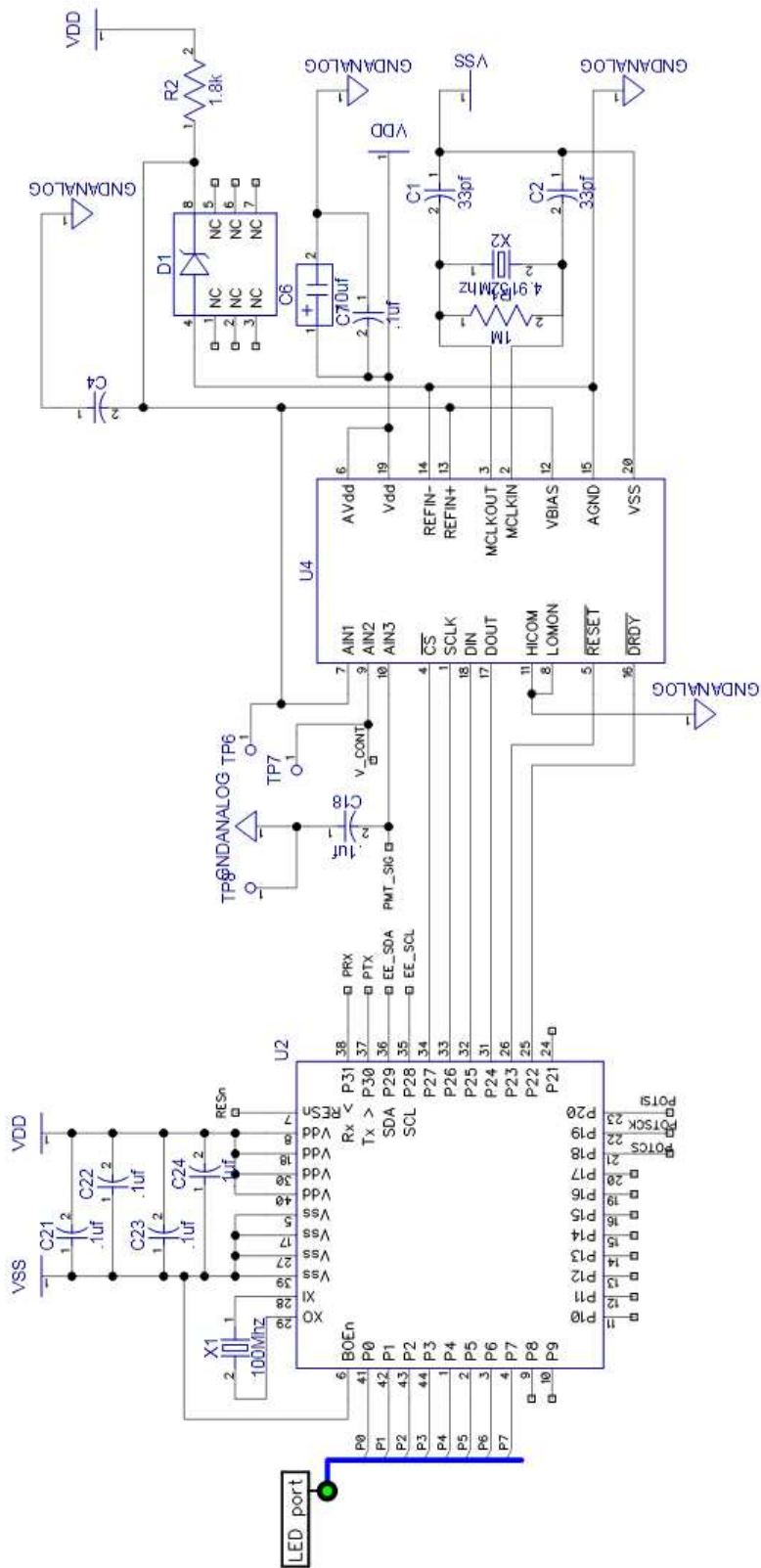


Figure F.4. A schematic drawing (Part 3) of the electronics of System III.

### F.3 Bill Of Materials

This appendix only includes a bill of materials of all integrated circuit (IC) components in the circuit.

Table F.1. Bill of Materials of all IC components in System III

Item	Description	Manufacturer	Part Number
U1	Custom part footprint	N/A	N/A
U2	Microcontroller	Parallax	P8X32A-Q44
U3	Digital Potentiometer	Microchip	MCP41XXX
U4	3-Channel 16-Bit, Sigma-Delta ADC	Analog Device	AD7707
U5	28-pin USB UART IC	FTDI Chip	FT232RL
U6	High Side Power Switch	STMicroelectronics	ST890
U7	DC-DC Converter, PMT power supply	V-infinity	VASD1-SIP
U8	USB Host Shield	Standard	Standard
U9	+3.3 Linear Voltage Regulator	National Semiconductor	LP2950ACZ-3.3/NOPB

### F.4 User's Manual

The measurement procedures of System III are the same as System II except for slight difference in the software operation. The software interface for System III uses a .NET framework. After installing the hardware drivers and the FiberReader.exe program, the system is ready for measurements. Open the FiberReader.exe file, the user interface is very self-explanatory, as shown in Figure F.5. After connecting the USB connector from the system to the computer, select "Comm Port" option under the "Settings", as shown in

Figure F.6. Select the "COM Port" to the port user connected the USB to, then select "Save", as shown in Figure F.7. Once the "Start" button from the main interface is pressed, the software starts to read and display the PL intensities, and store the data into a XML file once the program is manually stopped.



Figure F.5. A screenshot of the user interface for System III measurements.

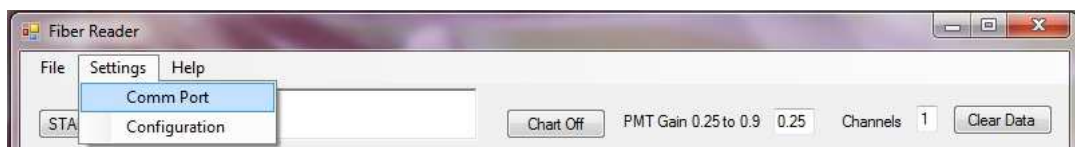


Figure F.6. A screenshot of the user interface for System III measurements.

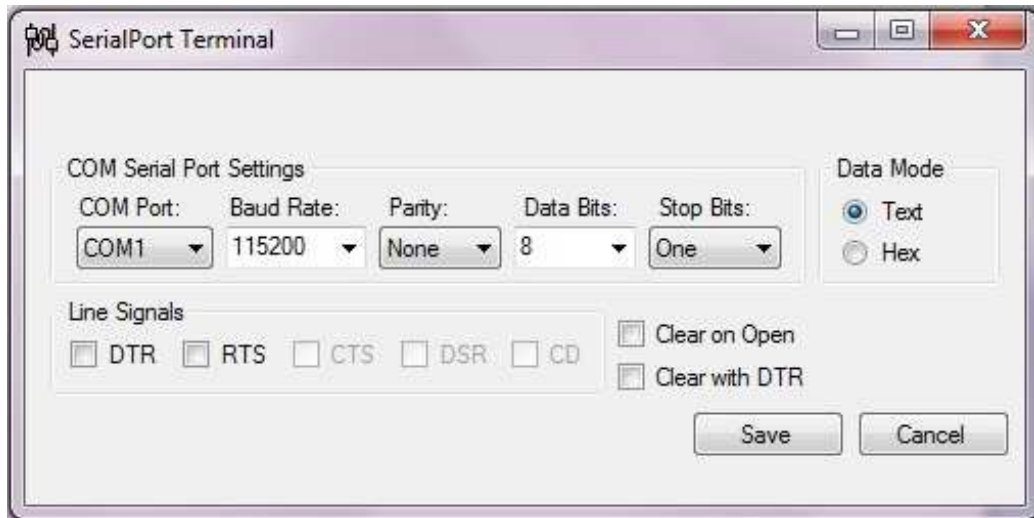


Figure F.7. A screenshot of the user interface for System III measurements.

# Appendix G

## ST CONNECTOR RELATED PROBLEMS

### G.1 Introduction

During the measurements using System II, by accident, an observation was made that by simply disconnecting and immediately re-connecting the ST-connectorized optode's fiber to the system, the fluorescent readings varies quite significantly. Without the motion of disconnecting and re-connecting the optode, the normalized standard deviation of 10 measurements is 1%, while the disconnecting and reconnecting the optode brings up the relative standard deviation to 5%. Because an ST-ST connector is an in-contact connection, meaning the fiber surface becomes in contact with the connecting fiber's surface. Theoretically, if the surface areas of the connecting fibers are the same, the coupling efficiency should be 100% and consistent for every connection. Therefore the optode fiber surface was inspected. An theoretical analysis of the impact of the defects on the optode fiber surface to the insertion loss variations of the measurements.

## G.2 Fiber Inspections

An inspection of the fiber surface was performed on three subject optodes. The results are shown in Figure G.1. Optode 1 (top left) is a rarely used optode, while the other two optodes are frequently used optodes. The frequently used optodes have obvious defects and particles on the fiber surface.

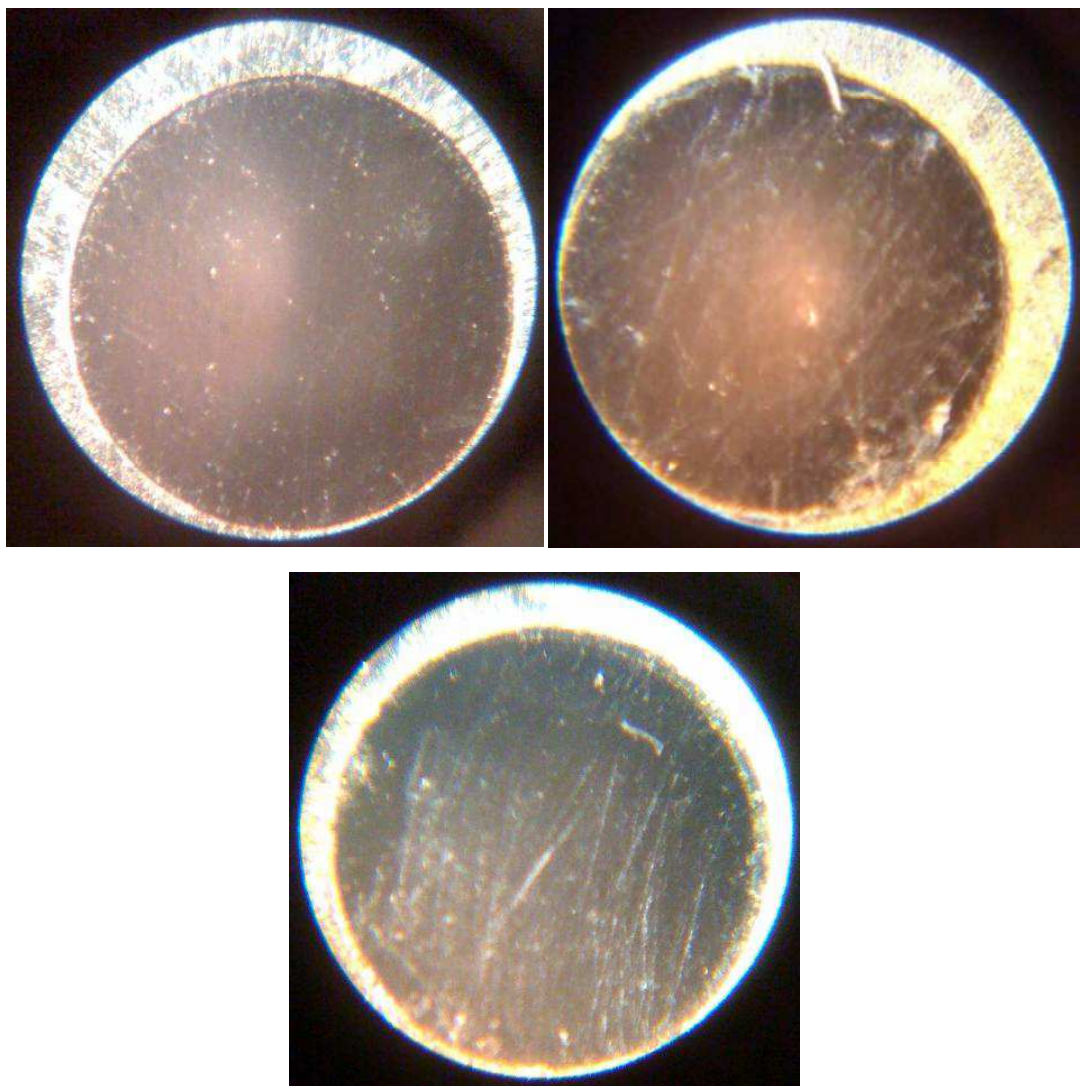


Figure G.1. Fiber surface inspections of three subject optodes: top left picture shows Optode 1; top right picture shows Optode 2; and bottom picture shows Optode 3.

### G.3 An Analysis on the Variation

One may wonder how much difference can a small defect have on the insertion loss of a fiber. To answer the question, a simple analysis of the defect impact on the insertion loss variation is carried out here. Using Optode 2 as an example for the calculation, the entire surface of the fiber has an area of  $A_0$ , and the defects and particles take up areas of  $A_1$  and  $A_2$ , as shown in Figure G.2. The calculation of the insertion loss caused by the surface defects are the following:

$$A_0 = \pi r^2, \quad \text{G-1}$$

where  $r$  is the radius of the fiber core. The areas of the defects shown in Figure G.2 are

$$A' = A_1 + A_2 = \frac{30^\circ}{360^\circ} \pi \left[ r^2 - \left( \frac{2}{3} r \right)^2 \right] + \frac{15^\circ}{360^\circ} \pi \left[ r^2 - \left( \frac{4}{5} r \right)^2 \right], \quad \text{G-2}$$

where the angles are an estimation.

$$\frac{P_{\text{out}}}{P_{\text{in}}} = \frac{A_0 - A'}{A_0} = 87.7\% \quad \text{G-3}$$

Therefore, the insertion loss variations caused by the defects on the fiber surface can be lower than the ideal scenario by 12.3%. Also, as specified by the ST mating sleeve (IF 830063, Industrial Fiber Optics) datasheet, the insertion loss variation after 500 connections is less than 0.10 dB.

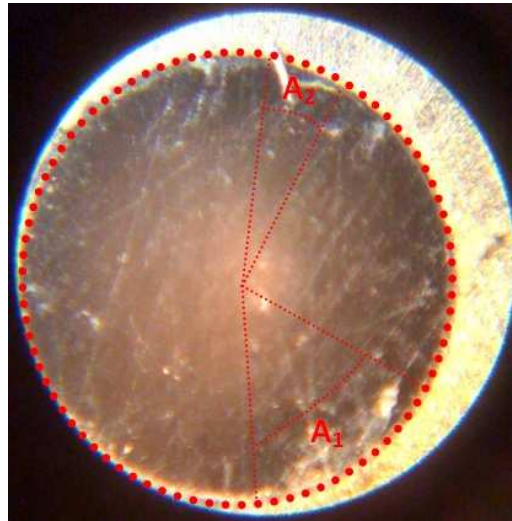


Figure G.2. An illustration of the surface areas referred to in the calculation.

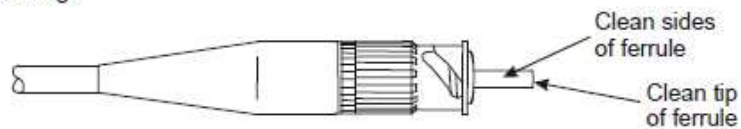
#### **G.4 Cleaning Procedures**

Instructions of cleaning the ST connector and the ST mating sleeve is shown in Figure G.3 [1].

### Clean ST Connector and Adapter

Clean exposed connector ferrule by lightly moistening lint-free wipe with fiber optic cleaning solution (or >91% isopropyl alcohol), and by applying medium pressure, first wipe against wet area and then onto dry area to clean potential residue from end face. Clean connector ferrule inside adapter by inserting lightly moistened cleaning stick with fiber optic cleaning solution (or >91% isopropyl alcohol) inside the adapter until contact is made with connector on opposite end. Rotate cleaning stick with medium pressure in one circular motion as it is pulled away from the adapter. Repeat process using dry cleaning stick.

**Caution:** Signal strength will be affected if end and sides of ferrule are not thoroughly cleaned. Discard cleaning sticks after each use. Do not turn cleaning sticks back and forth pressing against connector end face. This may cause scratches if large contamination is present. Always inspect connector end face for contamination after each cleaning.



Clean adapter by inserting adapter cleaning stick (or fiber adapter sleeve brush) moistened with fiber optic cleaning solution (or >91% isopropyl alcohol) inside the adapter and gently pull out with twisting motion. Repeat process with a dry cleaning stick.

**Caution:** Discard cleaning sticks after each use. Do not try to clean the adapter with cleaning stick if a connector is mounted in one side.

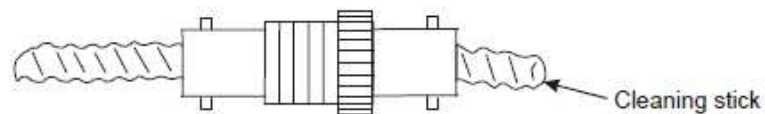


Figure G.3. Instructions on how to clean an ST connector and an ST-ST mating sleeve. Reproduced from Reference [1].

## **G.5 References**

- [1] Comm Scope. (2008, Nov) Comm Scope Instruction Sheet. [Online].  
[docs.commscope.com/Public/700\\_074\\_628.pdf](https://docs.commscope.com/Public/700_074_628.pdf)